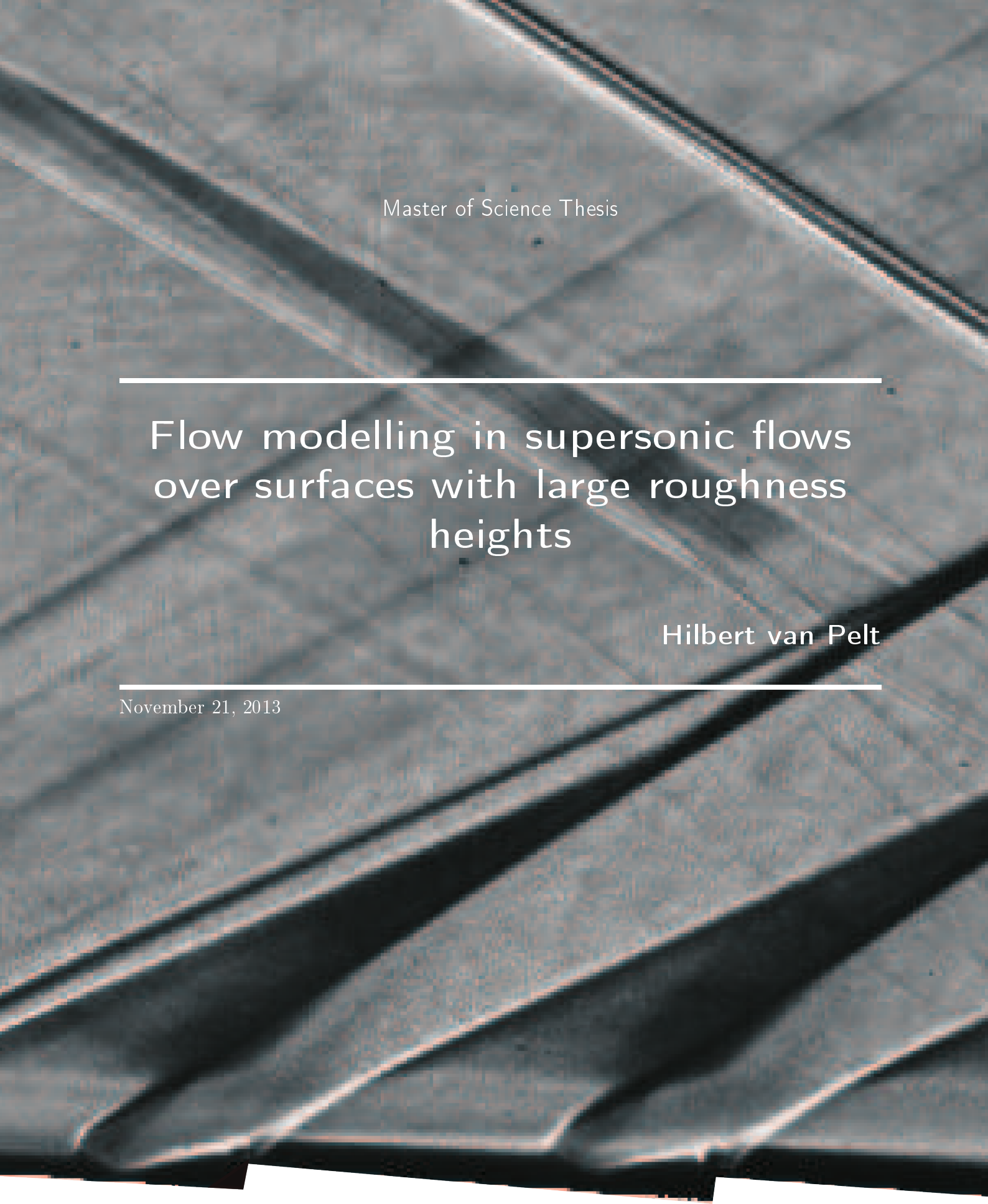

Master of Science Thesis

Flow modelling in supersonic flows over surfaces with large roughness heights

Hilbert van Pelt

November 21, 2013

Aerodynamics

ASTRIUM AN EADS COMPANY

TU Delft

Faculty of Aerospace Engineering

Delft University of Technology

Flow modelling in supersonic flows over surfaces with large roughness heights

Master of Science Thesis

For obtaining the degree of Master of Science in Aerospace Engineering at Delft University of Technology

Hilbert van Pelt

November 21, 2013

Faculty of Aerospace Engineering · Delft University of Technology

Delft University of Technology

DELFT UNIVERSITY OF TECHNOLOGY
DEPARTMENT OF AERODYNAMICS

The undersigned hereby certify that they have read and recommend to the Faculty of Aerospace Engineering for acceptance the thesis entitled **"Flow modelling in supersonic flows over surfaces with large roughness heights"** by **Hilbert van Pelt** in fulfillment of the requirements for the degree of **Master of Science**.

Dated: November 21, 2013

Committee Members:

Dr. ir. B.W. van Oudheusden

Dr. ir. L.J. Souverein (EADS - Astrium)

Dr. ir. F.F.J. Schrijer

ir. B.T.C. Zandbergen

Preface

This thesis represents the final project of my master aerodynamics at Delft University of Technology. After my internship at Gasdynamics Ltd in England this thesis project gave me the opportunity to work at EADS Astrium in Munich, and therefore experience working in a large aerospace company. I want to thank Louis for his guidance during my time in Munich, and his advice during the rest of the project. I also want to thank Katharina for her expert advice on all matters concerning CFD.

In Delft the experimental part of this project has been executed. This experimental part included supersonic testing of a set of geometries with Schlieren and PIV. These could be used as validation for the numerical work done at EADS Astrium. I want to extend thanks to Bas and Ferry for their guidance and insight during the entire project.
A special thanks goes to Peter, and Frits for their help with the design of the test set-up, and the multiple times that the tunnel had to be run. During my multitude of trips back to England, we had a number of discussions about roughness in general. Therefore i want to thank the people at Gasdynamics for the insight i gained during these discussions.

I want to thank Dr. Jaap van Pelt for his help correcting this report.

Abstract

Flow over smooth surfaces has been studied ever since the start of aerodynamic research. Non-smooth irregularities in rough walled surfaces will impact on the flow and induce changes in friction and heat transfer. The term 'rough walled' encompasses a range of shapes, ranging from material roughness to wall profiles with heights up to the boundary layer thickness. The effect of material roughness has been studied extensively, but data on large roughness elements is scarce and case-specific, depending on flow conditions and roughness element shape.

In the present research manufactured shapes of variable heights have been studied under supersonic flow conditions at a free stream Mach number of 2. The shapes used are saw tooths with a certain length and height. The flow over these shapes has been studied computationally by means of Computational Fluid Dynamics (CFD) methods, using the commercially available program CFX. Experimental investigations were performed with Schlieren photography and Particle Image Velocimetry (PIV). The CFD simulations were preformed under adiabatic, heated and cooled wall conditions respectively. The experiments were carried out in the ST-15 supersonic windtunnel at the TU Delft, with the aim to validate the CFD results. The numerical results were found to be in good agreement with the experimental results, apart from two flow cases where significant differences were observed between the numerical and experimental results.

Three flow categories could be distinguished, based on the flow separation mechanism. The first two cases concerned geometries in which the step length was significantly larger than the step height.

In the first case the roughness height was large and the separation in front of the step was found to encompass a separated region, bounded by a shear layer, and a strong shock before the step. In this case the pressure drag dominated the drag force. For the roughness heights tested in this report the drag force increased by a factor of 9 to 13 times the flat plate friction, depending on the roughness height. Heat transfer coefficient variations on the non-adiabatic walls of 7 percent with respect to the flat plate have been found.

In the second case, for smaller roughness height no pronounced shock formation was observed, stagnation pressure was lower then the elements in the first case. Pressure drag is still a dominant force and drag increases by a factor 5 with respect to flat plate friction were found. Variations of 1 to 7 percent in the heat transfer coefficient on the non-adiabatic walls were observed.

The third case concerned roughness elements were the height of the step was in the same order of magnitude as the length of the element, therefore a cavity type flow was observed. Due to this cavity flow, viscous forces where found to be negligible, but pressure forces and heating were significant. Friction increases of 6.1 and 7.5 times the flat plate friction where measured. Heat transfer coefficients varied on the non-adiabatic walls between a 4 percent increase to a 14 percent decrease of the flat plate value for the heated and cooled wall respectively. The drag can be predicted well with a cavity flow assumption. For all three flows categories correlations of the forces and the heating with the geometry and mean flow where found.

Contents

List of Figures

List of Tables

Nomenclature

$\overline{u'v'}$	uv Reynolds stress	$[N/m^2]$
α	Angle Roughess geometry	[deg]
α_e	Equivalent frequency	[1/m]
β	Compressibility corection, Shock angle	$[\sqrt{M^2-1}$, deg]
Δn	Size first mesh point at wall	[m]
δ	Boundary layer thickness	[m]
δ^*	Displacement thickness	[m]
δ_f	Size frictional sublayer	$[\frac{\mu_0^2}{\rho_0 \tau_{N_0} \alpha_e}]$
$\dot{Q}$	Total heat flux	[W]
ϵ_e	Equivalent amplitude	[m]
$\frac{dH_0}{dY}$	Wall normal derivative total wall enthalpy	[J/kg/m]
κ	Von Karman Boundary layer constant	[-]
μ	Viscocity	[Pa*s]
μ_{w_0}	Wall viscosity	[Pa*s]
ω_o	Spatial frequency roughness elements	$[1/m]$
Ω_p	Equivalent amplitude	$[\frac{\alpha_e \delta_f^2 \widetilde{P}(0)}{\epsilon_e \tau_{N_0}}]$

$\overline{u'u'}$	uu Reynolds stress	$[N/m^2]$
$\overline{v'v'}$	vv Reynolds stress	$[N/m^2]$
ρ	Density Gas	$[kg/m^3]$
ρ_p	Desity seeding particle	$[kg/m^3]$
σ	Mixing length	[-]
τ	Shear stress	[N/m]
τ_f	Relaxation time particle	[s]
τ_{N_0}	Baseline wall shear	[N/m]
θ	Wedge angle, Momentum thickness	[deg, m]
$\triangle t$	Time separation PIV image aquisitions	[-]
$\triangle U^+$	Log law Shift parameter	[-]
$\triangle x_{s1}$	Addition to sepration length for constant p_2 model	[m]
$\triangle x_s$	Distance pressure build up to separation point	[m]
$\triangle \tilde{\dot{q}}_w$	Change in wall heat flux	$[W/m^2]$
$\triangle \widetilde{\tau}$	Change in wall shear	[N/m]
υ	Kinematic viscosity	$[s^2/m]$
ξ	Friction coefficient	$[4 * C_f]$
a_k	Fourier coefficients roughness modeling	[-]
b_k	Fourier coefficients roughness modeling	[-]
B_{rough}	Alternative law of the wall parameter	[-]
C_f	Friction factor	[-]
C_p	Specific heat at constant pressure	$[J/kg/K]$
d_p	Diameter seeding particle	[m]
h_{w_0}	Wall enthalpy	[J/kg]
k^+	Non-dimension roughness height	$[\frac{ku_\tau}{\upsilon}]$

k_{eq}	Equivalent sand grain roughness	[m]
k_n	Roughness height nozzle	[m]
k_w	Roughness height wind tunnel	[m]
L	Length roughness geometry	[m]
L_{sep}	Separated flow length	[m]
L_t	length test section	[m]
L_w	Attached flow length	[m]
M_e	Mach number	[-]
P_0	Total pressure	[Pa]
Re_θ	Reynolds number based on momentum thickness	[-]
S_t	Stanton number	[-]
T^*	Reference temperature	[K]
T_{ref}	Reference Temperature Sutherlands law	[K]
T_t	Total temperature	[K]
T_{wad}	adiabatic wall temperature	[K]
u^+	Non-dimensional Velocity	$[\frac{u}{u_\tau}]$
U_0	Free stream velocity	[m/s]
u_τ	Friction velocity	[m/s]
U_f	Velocity flow	[m/s]
U_p	Velocity seeding particle	[m/s]
x_p	Plateau size constant pressure	[m]
x_s	Distance step to separation point	[m]
y^+	Non-dimensional height	$[\frac{yu_\tau}{\upsilon}]$
B	Von Karman Boundary layer constant	[-]
c	Speed of light	[m/s]
d	Wind tunnel diamter	[m]

h	Heat transfer coefficient	$[W/m^2/K]$
K	Gladstone Dale constant	$[m^3/kg]$
k	Roughness height, thermal conductivity, Wave number roughness modeling	[m, W/K, -]
Ln	Nozzle length	[m]
M	Magnification lens	[-]
N	Number of Fourier coefficients considerd	[-]
n	Refractive index	[-]
Pr	Prandtl number	[-]
R	Nozzle geometry radius, Specific gas constant	[m, j/kg/K]
r	Recovery factor	[-]
S	Sutherlands law constant	[K]
s	Coordinate along geometry	[m]
SF	size factor	[-]
u	Velocity x direction	[m/s]
V	Velocity	[m/s]
v	Velocity y direction	[m/s]
y	Distance perpendicular to surface	[m]

Chapter 1

Introduction

The first man made object to go supersonic is a whip, which has been in use for more the 5000 years [24]. With the introduction and development of firearms also bullets obtained the capability to go supersonic. On the 19th of January 1946 American pilot Chuck Yeager was the first human to fly supersonic with his Bell X-1 aircraft.

Figure 1.1: Bell X1, NASA [29]

With the progression of time, and the start of the "Space Race" between the Soviet Union and the United States flight speeds increased further. Inside the rocket engines that were the backbone of the Space Race, also supersonic flow occurs. In a rocket engine, propellants react in the combustion chamber, the produced gases are then expanded through a nozzle to generate thrust.

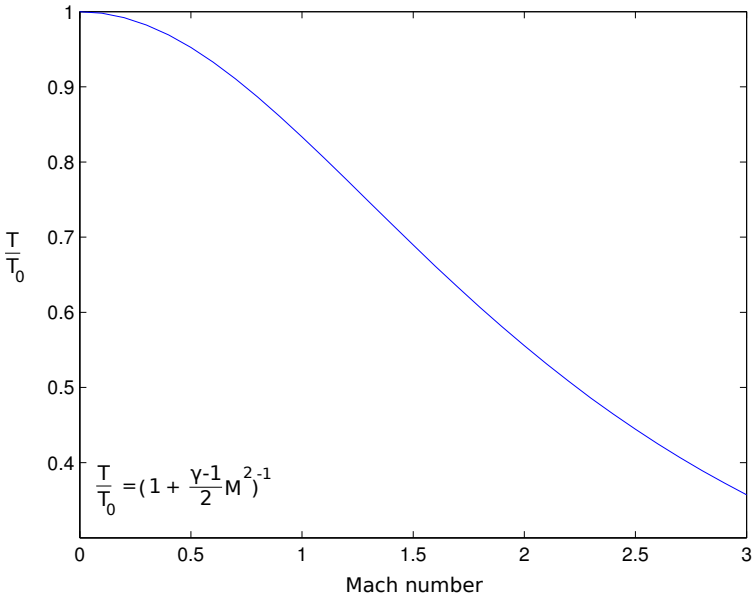

Figure 1.2: Isentropic expansion temperature

When the gases expand in the nozzle there temperature deceases, and there Mach number increases. Assuming the expansion in the nozzle is isentropic figure 1.2 shows how temperature would vary, see Anderson [26] for details on the equation. From figure 1.2 it can be seen that for Mach 3 the mean flow temperature reaches 35 % of the total temperature in the combustion chamber. Combustion chamber temperatures can be in excess of 3000 Kelvin, which means that the gas temperature at the end of the Nozzle can reach as high as 1050 Kelvin. With these temperatures active cooling is required to enable continuous operation of the engine. This cooling can be achieved in multiple ways, for example: film cooling, ablation, cooling channels.

In the case of film cooling a stream of cool fluid is injected into the stream which creates a thermal barrier between the wall and the hot gas. With an ablated wall, the wall burns off. The energy required to burn off the wall, is the cooling achieved. With an ablation system no continuous operation can be achieved, but most engines have to operate for a set amount of time. The maximum operating temperature for ablation systems is higher than for the film cooling and cooling channel systems. An other option is the installation of cooling channels. In this way small channels with cooling fluid are installed into the wall. The cooling fluid takes the produced heat away and thereby keeps the wall at an equilibrium temperature. Whichever cooling method chosen for a proper design, a good predictive capability of the heat transfer on the hot wall side of the nozzle is mandatory. Flow properties of the hot gases are influenced by the surface properties of the inside wall of the combustion chamber and nozzle, and thus also heat transfer and friction will change with a change in surface properties.

For this research the interest lies in rough surfaces. In practice these rough wall geometries can have many forms and shapes. They can range from a roughness on the surface , to machined shapes in the surface itself. Material roughness has been extensively researched. In the past it was shown by Nikuradse [22] that a turbulent boundary layer flow will exist on the rough surface. With additions to the standard law of the wall the influence of the surface roughness of the flow can be described. In this report we will not deal with

material roughness, but with per-determined shapes that are machined into the material in order to represent the surface irregularities of the inside of a rocket nozzle. We will pose the question what are the effects of such shapes on the flow, focusing in particular on the size of machined surface profiles. The flow that was studied by Nikuradse was a flow where drag, and heat transfer were dominated by friction, while pressure effects were of no influence. When the elements become large pressure effects actually become dominant over the viscous effects, as will be shown. To determine how these forces behave, and where there is a switch between the flow studied by Nikuradse, and a flow with large roughness elements research is needed. Most researchers have studied small roughness flow, but data on large structures in the framework of roughness is scarce, and scattered. This report on the other hand contains a discussion on elements ranging from small to large roughness structures. For the variations in size one geometrical shape was used.
This investigation was initiated by a research interest of EADS Astrium. As a world leader in the design of rockets and spacecrafts a proper understanding and determination of nozzle heat transfer is critical. The nozzle with a specific interest is a tube nozzle which have been used in all the upper stages of the Ariane rocket family.

Figure 1.3: Ariane 5, Arianespace [1]

Figure 1.3 shows the Ariane 5, the latest rocket in the series. Ariane 5 has 2 main stages and 2 solid boosters. In figure 1.3 3 cylindrical shapes can be seen, the boosters are the cylinders on the outside, which the main stage is in the middle. The nozzle, which is part of the rocket engine where the flow comes out, can be seen on the rear of the rocket. The second stage, which in on top of the main stage, has a tube nozzle. A tube nozzle from Astrium is non-smooth due to the choice of cooling system. The nozzle is cooled by cooling channels which are made by welding multiple hollow tubes together. All the tubes have the same cross section and the production of this tube nozzle shape yields a non-smooth wall.

The production of these tube nozzles is done by an automated welding machine. This ensures a constant weld quality, and produces a strong weld.

Figure 1.4: Tube nozzle, Arianespace [2]

Figure 1.4 shows a tube nozzle. A nozzle shape can be seen, including all the tubes. These tubes are welded together to allow for an actively cooled nozzle, which is still strong. The internal shape of this nozzle will be taken as a baseline, from where the tested shapes will be derived.

In this report multiple shapes are investigated regarding their influence on the friction and heat transfer of these plates. This research considers heated, adiabatic and cooled walls, such that the results will allow an interpretation of the effects of the thermal wall conditions.

Since Nikuradse started the field of material roughness, countless investigations have been done on rough walled geometries. But the main question to be addressed is, what happens when the size of the roughness increases. Therefore the main research question is

'*Determine the surface drag and heat transfer over a non-smooth wall, where the size of the non-smooth profiles ranges from small with respect to the boundary layer thickness, to in the same order of magnitude of the boundary layer thickness*'

In the research question only heat transfer is mentioned, but heat transfer and friction are closely related. Therefore the friction is also of importance. To investigate the relation between the wall shear, heat transfer, and element geometry, multiple geometries have been defined. These are variations on the nozzle geometry from the baseline nozzle. These variations include variations on the size and length of the roughness elements. Also the importance of the various occurring flow phenomena is investigated.
The investigations have been done following a combined computational and experimental approach. First a CFD study has been performed on all the geometries. These compu-

tational solutions are obtained for a turbulent flow over an adiabatic wall, a heated and cooled wall. This was done to be able to compute the heat transfer. In the experimental approach (in a supersonic wind tunnel) the flow was visualized using Schlieren technology. Thereby individual shock positions can be measured, and the overall flow topology can be obtained. Particle Image Velocimetry (PIV) was subsequently used to measure the velocity in the flow field. Finally, the computational validated against the experimental results. With the PIV set-up the flow cannot be measured inside the roughness elements, and therefore it does not provide data for calculating the friction and heat transfer inside the elements. Therefore in this study the validation is done on the results in the boundary layer, and mean flow. The forces and the heat transfer are calculated on the basis of the numerical results. The research question is then answered on the basis of experimental validation of analytical models and correlations between the wall forces and heat transfer in relation to the wall geometry.

Chapter 2

Rough wall flow

2.1 Rough wall geometrical aspects

For smooth walls and attached flows, the boundary layer can be well described using classical boundary layer theory, see Schlichting [18]. However when the wall is non-smooth significant changes in the boundary layer properties may be observed. These changes will impact the force and heat transfer distribution along the wall. A review will be given on the most relevant literature for rough wall flows. This chapter has its origin in [17], where a more detailed review can be found. The section on wavy wall modeling is work that has been done for this report. This chapter describes the influence of shape and distribution on the flow, and methods for computational modeling of these influences.

2.1.1 General considerations

A rough wall is different from a smooth wall in the sense that it contains roughness elements which affect the flow. As was shown by Jimenez [21], rough wall effects can be broadly divided into two categories. In the first category the effects on the flow are small enough such that a general yet modified boundary layer profile is retained. In the second category, the disruptions are of such a magnitude that the boundary layer flow profile is affected to such a degree that the boundary layer will need to reestablish itself after the roughness element. For this second case the individual roughness elements will have to be modeled since each individual element has an influence on the flow. For the smaller elements, a boundary layer will form on top of these elements, and this boundary layer can be described with additions to standard boundary layer theory. As will be shown these 2 categories apply also to the cases tested in this report.

2.1.2 Height implications

When considering the influence of roughness elements on the turbulent boundary layer, it is important to consider the non-dimensional height of the elements k^+, $k^+ = \frac{ku_\tau}{\nu}$. Roughness effects can be classified on the basis of this non-dimensional roughness height. For $0 \leq k^+ \leq 5$ the element resides in the viscous sublayer, therefore no effect of the roughness will be seen. For $k^+ > 5$ there is a notable influence of the wall roughness on forces and heating. The range $5 < k^+ \leq 70$ is called the transitional rough range since there is an influence of viscosity. For $k^+ > 70$, there is no influence of viscosity because the elements protrudes outside the viscous sublayer. See White [12] for a more detailed description. This regime is called the fully rough regime. As was described earlier, there are two categories of flow, a rough walled boundary layer flow, and a flow where individual elements should be modeled. According to Jimenez [21] the switch from boundary layer behavior, to separate element behavior occurs at a $\frac{k}{\delta} > 0.2$, where k is the roughness height and δ the boundary layer thickness. As will be shown in this report element modeling was needed for roughness elements smaller then $\frac{k}{\delta} = 0.2$. A more detailed discussion on this boundary can be found in section 7.5.

2.1.3 Distribution

The spatial distribution of roughness elements can be divided into two categories: randomly distributed or a periodic distribution. Unstructured rough materials will generally develop a boundary layer flow, since the roughness heights are generally small. In the case of structured roughnesses, such as in riveted plates, there will be a repeating process of disturbing the flow over the element, and recovery of the boundary layer in the space between the subsequent roughness elements. When the roughness elements are sufficiently small with respect to the boundary layer thickness, the flow can still be modeled as a boundary layer flow, such that on average the rivet flow can still be modeled by a boundary layer distribution [12].

When the roughness elements are sufficiently large, and the peaks are closely packed together a cavity flow can occur [23]. In this case a region of separated flow will occur between the roughness elements and the main flow will settle on top of the cavity. This type of flow can occur in both 2D and 3D flows. In this report only 2D flows where tested.

2.2 Modeling possibilities

2.2.1 Sand grain roughness

A proven method to describe small-scale distributed roughness is by means of sand grain roughness. Sand grain roughness is a method developed by Nikuradse [22], where the flow is modeled by closely packed spheres. The model can be seen in figure 2.1.

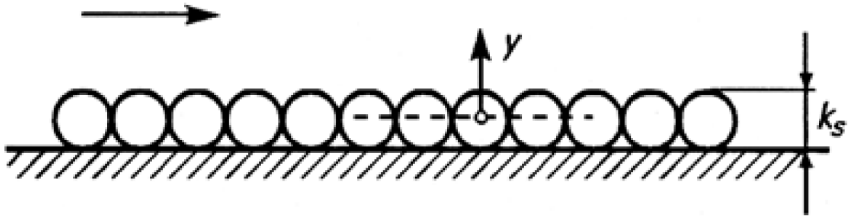

Figure 2.1: Sand Grain roughness model (Schlichting [18])

As can be seen in figure 2.1 the roughness is modeled by closely packed spheres with a diameter k_s, which is the sand grain roughness height. Consequently the origin of the y axis is not placed at the wall, but at half the roughness height k_s, see figure 2.1. Following White [12] one can now state that the boundary layer on top of these elements can be described by adding an extra term to the log law, resulting in

$$u^+ = \frac{1}{\kappa} ln\left(y^+\right) + B - \triangle U^+ \tag{2.1}$$

According to equation 2.1 a rough wall boundary layer follows the same profile as a normal boundary layer, but shifted by the term $\triangle U^+$. For sand grain roughness the roughness term $\triangle U^+$ can be written as $\frac{1}{\kappa} ln(1 + 0.3k^+)$ where k^+ is the non-dimensional roughness height defined by $k^+ = \frac{ku_\tau}{\nu}$. This makes that the boundary layer on a rough walled surface can be described by

$$u^+ = \frac{1}{\kappa} ln\left(y^+\right) + B - \frac{1}{\kappa} ln(1 + 0.3k^+) \tag{2.2}$$

According to equation 2.2 the flow over this specific surface can be described by a combination of the standard boundary layer parameters κ and B and the value of the k^+ for a specific surface.

2.2.1.1 Equivalent sand grain roughness Equation 2.2 is valid for a roughness of closely packed spheres. For a different geometry, or different distribution of the elements the equation still hold but a different "equivalent" sand grain roughness height has to be used. The equivalent sand grain roughness for a specific case is the sand grain roughness for which the resulting flow profile is the same as for this specific case. Following Schlichting [18] the boundary layer over a rough wall can be described by the following law of the wall,

$$u^+ = \frac{1}{\kappa} ln\left(\frac{y}{k}\right) + B_{rough} \tag{2.3}$$

Comparing equation (2.2) with (2.3) we can write

$$u^+ = \frac{1}{\kappa} ln\left(y^+\right) + B - \frac{1}{\kappa} ln(1 + 0.3k^+) = \frac{1}{\kappa} ln\left(\frac{y^+}{1 + 0.3k^+}\right) + B$$

Which for large k^+can be written as

$$u^+ = \frac{1}{\kappa} ln\left(\frac{y}{k}\right) + B - \frac{1}{\kappa} ln\left(0.3\right) \tag{2.4}$$

From which it can be concluded that for large k^+ B_{rough} can be written as $B - \frac{1}{\kappa} ln\left(0.3\right)$. For standard values of 5.5 for B and 0.41 for κ this amounts to a B_{rough} value of 8.4. This slightly overestimates the experimental results by Tani [19] which show that the value of B_{rough} should go to 8. According to Tani the value of 8 can be used for k^+ values larger then 70.
From equation (2.3) an equivalent sand grain roughness for a given velocity field can be defined by

$$k_{eq} = e^{\left\{\kappa \lim\limits_{y \to 0}\left[8 + \frac{1}{\kappa} ln(y) - u^+(y)\right]\right\}} \tag{2.5}$$

With equation 7.16 one can calculate the equivalent sand grain roughness k_{eq} for a given u^+ and y. In equation (7.16) the B_{rough} value of 8 can be seen. Equation (7.16) is only valid for the fully rough regime, so one must check that the k^+ value based on k_{eq} is bigger then 70. Both the original and equivalent sand grain roughness models imply that the flow, and the surface drag are dominated by friction.

2.2.2 Element flow

When an element becomes large with respect to the boundary layer thickness, the flow over the element itself has to be modeled. In this case the modeling focus changes from using a universal and uniform boundary layer law to finding the blockage and form drag of the individual elements, which will be shape specific. Hodge and Taylor [7] did a preliminary examination of a discrete roughness model; they derived equations for the flow around rough elements including blockage factors and drag coefficients. The model by Hodge and Taylor is not used in this report, but there initial ideas of modeling the elements them selfs are used.

2.2.3 Cavity flow

When there is a cut-out in a wall a cavity flow will occur. Cavity flow occurs in 2 types, an open or closed flow. In the open case the cut out is short, and therefore the flow does not reattach to the bottom of the cavity. In a closed cavity flow, the cut out is of such length, that the flow attaches to the bottom of the cavity, and separates at the downstream side of the cavity. The closed cavity has a large drag then the open cavity flow. As will be shown later, for an open cavity the drag is due to pressure drag, viscous drag is negligible. Cavity flows are generally not studied as part of rough wall flows, and therefore have not been discussed in the foregoing sections. But as this report will show cavity flows do have an important place in rough walled flows, and are therefore discussed here.

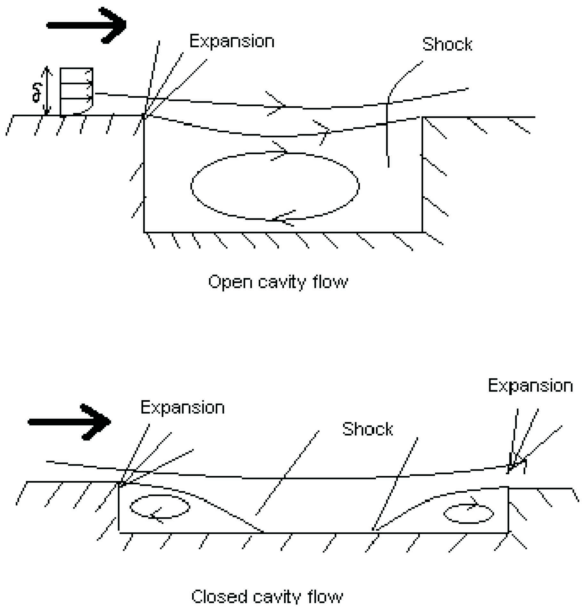

Figure 2.2: Open and closed cavity flow, (van Pelt [17])

Figure 2.2 illustrates that a cavity flow can be a open or closed cavity flow, in the presence of a supersonic external flow. On the top of the figure an open cavity flow can be seen. The flow does not reattach to the bottom of the cavity cavity, and therefore a region of recirculating flow is formed. On the bottom of the figure an closed cavity flow is shown. There the flow reattaches to the bottom of the cavity, and separates at the end of the cavity.

The drag of a cavity is main dominated by pressure forces. Figure 2.3 shows the pressure ratio along the floor of an open and closed cavity.

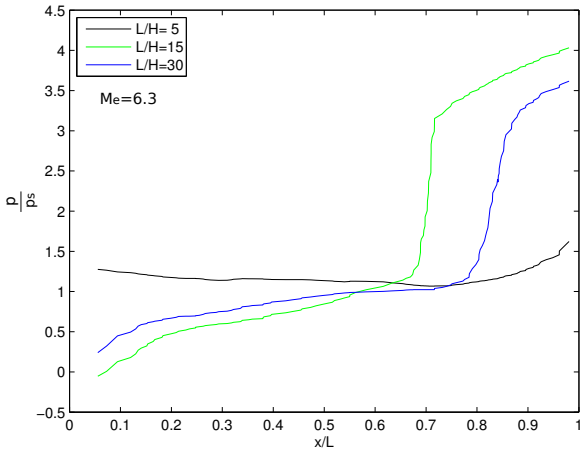

Figure 2.3: Pressure ratio along cavity floor, (Nestler et al[10].)

Figure 2.3 is a reproduction from a figure by Nestler et al[10].

The L/H (length over height of the cavity) ratios of 15 and 30 represent closed cavity flows, while the L/H ratio of 5 represents an open cavity flow. In the case of the closed cavity flow it can be seen that there is a large pressure build up on the downstream edge. For the open cavity flow a smaller pressure build up can be seen. The pressure differences with respect to to the flat plate is small and therefore the influences of the cavity on the drag are small as well. For the distribution of the heat transfer coefficients the same distribution can be observed.

2.2.4 Wavy wall

Equivalent sand grain modeling gives the possibility of describing the influence of the roughness on the flow field. The main issue with this kind of modeling is that a test needs to be done before a surface can be described. A theoretical approach to model a rough wall is given by Inger [14]. In his paper Inger assumes the wall height to vary sinusoidally, and

from this variation the change in heat transfer and wall shear are calculated. The author of this report has extended Ingers analysis by taking a wall that is modeled by a Fourier series.

For this extended modeling a flat plate flow should be assumed as baseline, the changes in this flat plate flow can then be calculated with this method. The changes in friction and heat transfer are given by

$$\triangle\widetilde{\tau} \simeq 1.37\tau_{N_0}\frac{\epsilon_e\Omega_p}{\delta_f}e^{\frac{4}{3}\pi i}\left[1+1.62e^{\pi i/3}\left(\frac{\delta_f}{h_{w_0}}\right)x\frac{dH_0}{dY}(0)\right] \tag{2.6}$$

$$\triangle\tilde{\tilde{q}}_w \simeq 0.443\mu_{w_0}\frac{dH_0}{dY}(0)\frac{\epsilon_e}{\delta_f}\Omega_p e^{\frac{4}{3}\pi i}\left[1+5.4\left(\frac{\delta_f}{h_{w_0}}\right)\frac{dH_0}{dY}e^{13\pi//30}\right] \tag{2.7}$$

Where ϵ_e is the equivalent amplitude given by

$$\epsilon_e = -\frac{1}{i}\sum_{k=1}^{N-1}e^{i\omega_o x}\left(a_k cosh\left(k\omega_o x\right)+ib_k sinh\left(k\omega_o x\right)\right) \tag{2.8}$$

Equation 2.8 shows a summation over the Fourier coefficients a_k and b_k. N is the number of Fourier coefficients considered. $\frac{\epsilon_e\Omega_p}{\delta_f}$ and includes the geometrical information, h_{w_0} is the wall enthalpy, τ_{N_0} and μ_{w_0} are the wall shear and the wall viscosity of the reference case and $\frac{dH_0}{dY}$ is the derivative of the total enthalpy at the wall. For the derivation of equation 2.8, and further considerations see Appendix C.

2.2.5 Reynolds Analogy

Under certain conditions a boundary layer flow displays similarity between the velocity and temperature profile [12]. Because wall shear and heat transfer both depend on a derivative to the wall normal, heat transfer and wall shear are then coupled. This coupling is called the Reynolds analogy. The heat transfer coefficient, expressed as a Stanton number can then be related to the friction coefficient.

$$S_t = \frac{h}{\rho V C_p} = \frac{C_f}{2}Pr^{-2/3} \tag{2.9}$$

In equation 2.9 the Reynolds analogy relates the heat transfer coefficient h, normalized by the density, velocity, and specific heat at constant pressure, with the friction and the Prandtl number. The assumptions used for the derivation of equation 2.9 are steady flow,

zero pressure gradient, constant specific heats and constant wall temperature. Therefore care has to be taken with the applicability of equation 2.9 in more general conditions. In attached flows with small pressure gradients the results are good, but when separation dominates, the results can deviate highly. In the light of the current research the Reynolds analogy will be used to calculate the in heat transfer as function of the friction.

Chapter 3

Test case

3.1 Baseline geometry and flow case.

The background for this investigation, is that of cooling a rocket nozzle. Due to non-smooth walls in this nozzle heat transfer and wall friction will change with respect to the flat plate case. The non-smoothness of the nozzle is due to installed cooling system. To test the influence of the wall geometry on the flow, multiple simplified models will be derived. With these simplified models the influence of variations in the geometry on the flow field can be investigated. In this section the geometries that will be tested will be derived from the nozzle geometry.
The nozzle that serves as the baseline for this project has a smooth surface in the throat, where the cooling is integrated in the wall. Downstream the nozzle is build-up out of cooling tubes welded together in a nozzle shape. A cut out of this nozzle is shown in figure 3.1.

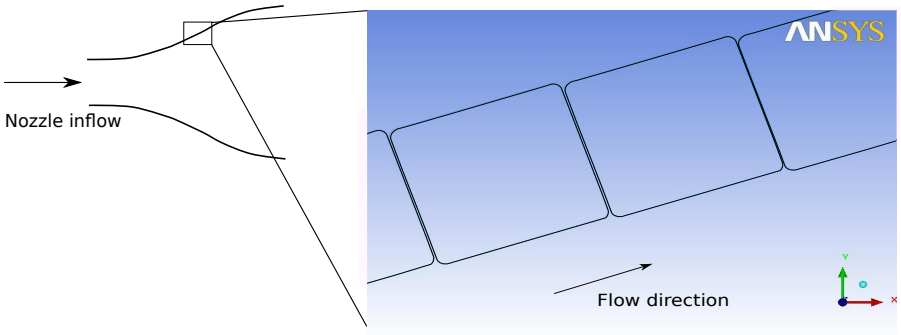

Figure 3.1: Nozzle cut out

In figure 3.1 the flow runs from left to right on the bottom side of the elements, and the cooling fluid would run, in and out of the screen. Taking a local tangent to this shape yields the shape the flow would see, in the case this geometry would be fabricated on a flat plate, see figure 3.2.

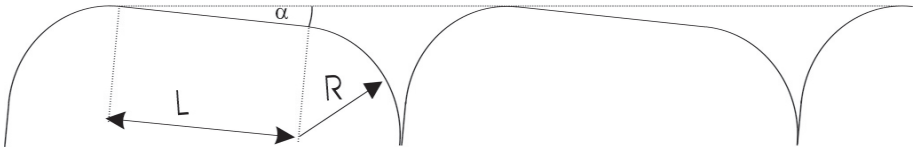

Figure 3.2: Local tangent to Nozzle geometry

Figure 3.2 displays a cross-sectional nozzle reference geometry from which all geometries for the report are derived. It shows that the nozzle geometry consists of a number of tube cross-sections that have been rotated over an angle α. The tubular cross-section consist of a flat section with length L and 2 rounded sections on each side with a radius R.

3.2 Basic test case

In order to perform a systematic investigation on the effect of geometrical variations on the boundary layer flow field, the geometry is simplified. However care is taken to include geometrical aspects that are essential for a correct simulation of the "true" flow field, as would follow from the original geometry. The methodology for defining the simplified geometry can be explained using figure 3.3.

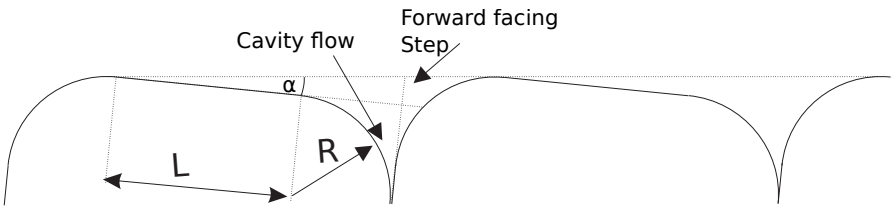

Figure 3.3: Geometry flow decomposition

Figure 3.3 is a reproduction of figure 3.2 with one imaginary line added. For a flow running from left to right, it is expected that it will at first be attached to the flat part, section described with L, at the section where the concave part starts it is expected that the flow will separate. Therefore it can be expected that the geometry includes two important flow

aspects, a forward facing step, and a cavity like flow. Based on these considerations a number of the geometries can be defined.

Figure 3.4 shows the shape definitions. The first geometry (figure 3.4, A) is the full geometry. The second shape (figure 3.4, B) is a saw tooth. This shape aims are reproducing only the effects of the forward facing step in the full geometry. In the third shape (figure 3.4, C) a cavity without the presence of a step is shown. Finally the effects of the combination of cavity and a step were investigated (figure 3.4, D). The main goal of this last test geometry is to investigate the flow for a combination of a cavity and a forward facing step, and determine which of the two geometrical elements dominates the flow field.

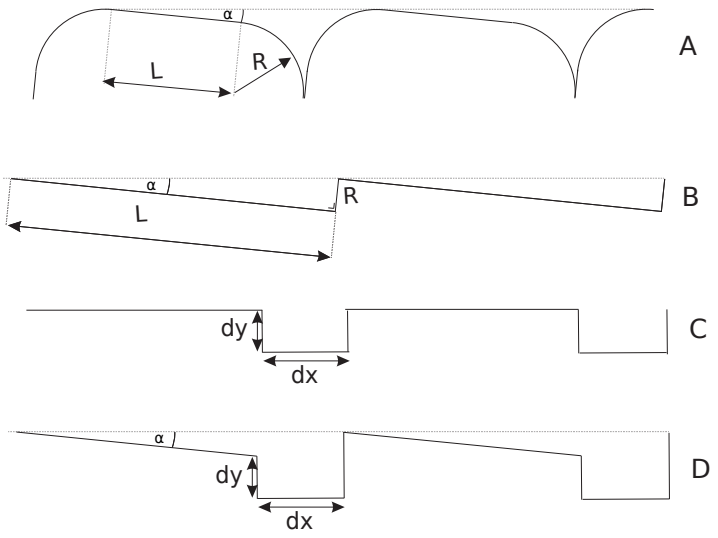

Figure 3.4: Roughness shape definitions

3.3 Geometrical dimensions

To define the dimensions of the geometries a start point is needed from which all other geometries will be derived. In order to determine the size of the roughness elements a local similarity between th actual nozzle flow and the flow in the wind tunnel test section will be defined.

Multiple options have been taken into account for similarity parameters. These are k^+, the non-dimensional roughness height, δ the boundary layer thickness and θ the momentum thickness. k^+ is defined by $\frac{ku_\tau}{\nu}$ where u_τ is the friction velocity and ν is the kinematic viscosity. Therefore k^+ can also be seen as a roughness Reynolds number. The displacement thickness δ^* was not taken into account, due to cooling of the nozzle wall the displacement thickness becomes negative which cannot be reproduced in the wind tunnel. To set a basic

design a size factor SF will be defined by :

$$SF = \frac{k_w}{k_n}$$

where k_w is the required roughness height in the wind tunnel and k_n is the roughness height in the nozzle. For k^+ similarity $\left(k^+_{nozzle} = k^+_{windtunnel}\right)$, θ similarity $\left(\frac{k}{\theta}|_{nozzle} = \frac{k}{\theta}|_{windtunnel}\right)$ or δ similarity $\left(\frac{\delta}{\theta}|_{nozzle} = \frac{\delta}{\theta}|_{windtunnel}\right)$, the size factor is a function of boundary layer variables in the nozzle and in the wind tunnel. The size factor needed to obtain all mentioned similarities has been calculated.

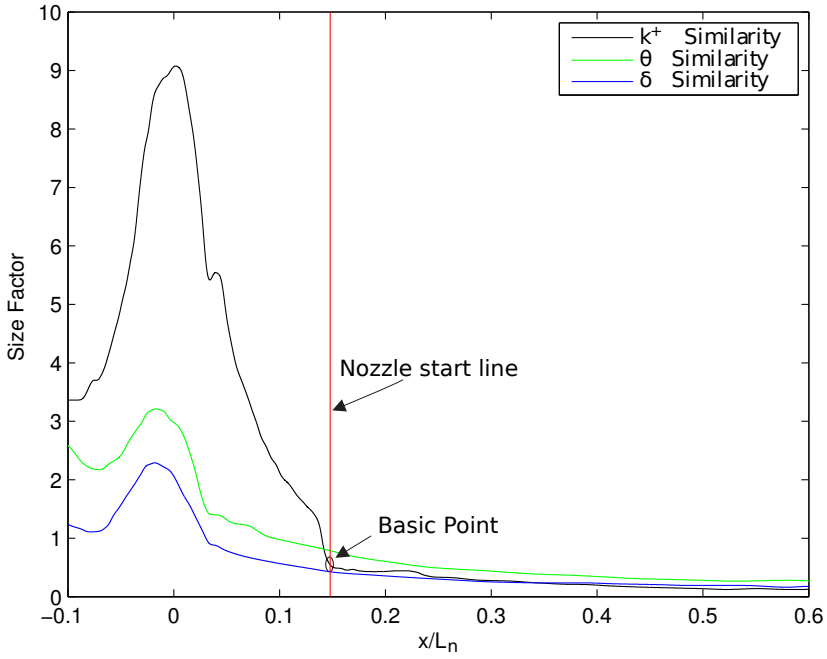

Figure 3.5: Size factor

Figure 3.5 shows the size factor to obtain k^+, δ, θ similarity. The nozzle boundary layer data was determined using the program TDK [35], while the boundary layer data from the wind tunnel were taken from Sun et al. [37], which applies to a Mach number of 2. The Mach number of 2 is also the Mach number a which the experiments will be run. This is due to the large body of knowledge available at Mach 2. The origin for the longitudinal coordinate x in figure 3.5 is located in the throat of the nozzle. A piece of the divergent section is still a structural part of the combustion chamber. The nozzle starts at 0.147 x/L_n, where L_n is the length of the nozzle. What can be observed is that upstream of the nozzle all size factors have a value which exceeds one, further downstream they decrease to a value below one. Recalling the discussion in section 2.2.1, k^+ is the primary similarity variable for rough flows, therefore the choice has been made to proceed with k^+ similarity.

The roughness size needed lies closely to the roughness size that would uphold θ or δ similarity. For wind tunnel measurements and manufacturing purposes large elements are preferable. Therefore the first element at the start of the nozzle has been selected for similarity to wind tunnel geometry. The size factor at this point in the nozzle is 0.59. The resulting geometrical values, and the flow variables are described in table 3.1 and 3.2.

Table 3.1: Comparison of nozzle and wind tunnel parameters: Geometrical values

Variable	Wind Tunnel	nozzle
R/δ	0.0637	0.14
L/δ	1.26	2.77
α(deg)	0.56	0.56
k/δ	0.0637	0.14

Table 3.1 list the geometrical parameters of the nozzle and wind tunnel shapes. All length scales have been normalized with the local boundary layer thickness. As can be seen the wind tunnel roughness elements extend less into the boundary layer compared to the real nozzle case. But it is expected that the effect on the flow will be the same due to the k^+ similarity.

Table 3.2: Comparison of nozzle and wind tunnel parameters: Flow variables

Variable	Wind tunnel	Nozzle
θ/δ	0.08	0.05
k^+	190	190
Re_θ	12242	632
C_f	1.937e-3	3.87e-3
u_τ (m/s)	3.420.84	124.5

The available wind tunnel test facility can only be run at discrete Mach numbers of 1.5, 2 and 2.5. The tests will be run at a single setting since the goal of this investigation is to investigate geometrical variations. Table 3.3 lists all the test conditions.

Table 3.3: Wind tunnel boundary layer characteristics

Variable	Tunnel
δ (mm)	5.18
θ (mm)	0.42
δ^*(mm)	1.18
P_t(bar)	3.2
M_e(-)	2.04
T_t(k)	290

All boundary layer characteristics displayed in table 3.3 are the compressible properties and have been used for the design of this test. They were measured with PIV in an empty tunnel by Sun et al. [37]. The current boundary layer characteristics including the roughness elements and geometrical inserts are given in section 5.1.

3.4 Test matrix

In the experiments a number of geometries will be tested. An overview is shown below.

Table 3.4: Test Matrix

Test point	Model	Model used	L/R	R (mm)	k^+	k (mm)	N CFD	N PIV
1	Flat plate	Flat plate	-	0	0	0	0	0
2	L48R25	Saw Tooth	19.8	2.45	1414	2.45	3	4
3	L33R17	Saw Tooth	19.8	1.66	960	1.65	5	6
4	L16R08	Saw Tooth	19.8	0.83	480	0.83	10	12
5	L06R03	Saw Tooth	19.8	0.33	190	0.33	26	30
6	L03R02	Saw Tooth	19.8	0.17	95	0.17	51	-
7	Cavity	Cavity	19.8	1.66	960	1.65	5	6
8	L33R17C	Saw Tooth &Cavity	19.8	1.66	960	3.21	5	6
9	Original geometry	Full	19.8	1.66	960	1.65	5	6
10	L10R17	Saw Tooth	6.09	1.66	960	1.65	16	19
11	L06R17	Saw Tooth	3.3	1.66	960	1.64	31	33

Table 3.4 shows the test matrix. The naming convention in derived from the geometry, figure 3.4, B. The forward facing step, which is the most used geometry in the test matrix, contains a length L and a height R. the naming is such that the number after L is the length of the forward facing step in mm. The number after R shows the height in tens of millimeters. For example the name L48R25 shows that the element has a length of 48 mm and a height of 2.5 mm.

The first test case is a flat plate which acts as reference. Test points 2 to 6 are a variation in roughness height. The basis case is test point 5 which corresponds to the similarity scaling of the nozzle roughness. The specific height of the L48R25 case has been chosen such that it is half the boundary layer. The L33R17 case has been chosen such that is as large as the log-law. The height of L16R08 geometry is half of the height of the L33R17 geometry. The height of the L03R02 geometry is half of the height of L06R03 geometry.

For the variation in shape the full shape, a cavity, and a saw tooth +cavity are chosen. The depth of the cavity has been taken the same as that of the L33R17 geometry. Figure 3.3 shows that the length of the cavity part is slightly larger than the radius. Therefore the length of the cavity has been set on 1.71 mm. For the L33R17C case the cavity geometry has been added to the L33R17 geometry.

Test points 10 and 11 are a variation in spatial frequency (the amount of roughness elements per unit spatial direction). The specific sizes are determined by varying the length of the L33R17 case, while keeping the height constant. The full shape (test point 9) has not been tested in the wind tunnel due to problems in the manufacturing of the curvatures in the geometry.

The number of elements used N for the CFD and PIV is also shown. As will be discussed in chapter 4 for the CFD the roughness elements have been incorporated into the nozzle, while for the PIV the elements have been fabricated onto special designed plates which fit onto the nozzle geometry. Since these plates had to be secured it was not possible to fill the entire test section with roughness elements. For the CFD there was no such restriction and therefore the choice was made to fill the entire test section with roughness elements. See figure 3.6 for a comparison on the sizes of the test cases. The figure is to size, and the boundary layer thickness is also shown. The cavity and L33R17C geometry are not shown, since they have the same roughness height as the L33R17 geometry. For a number of geometries extra elements are shown to give a better indication of the shape of the elements.

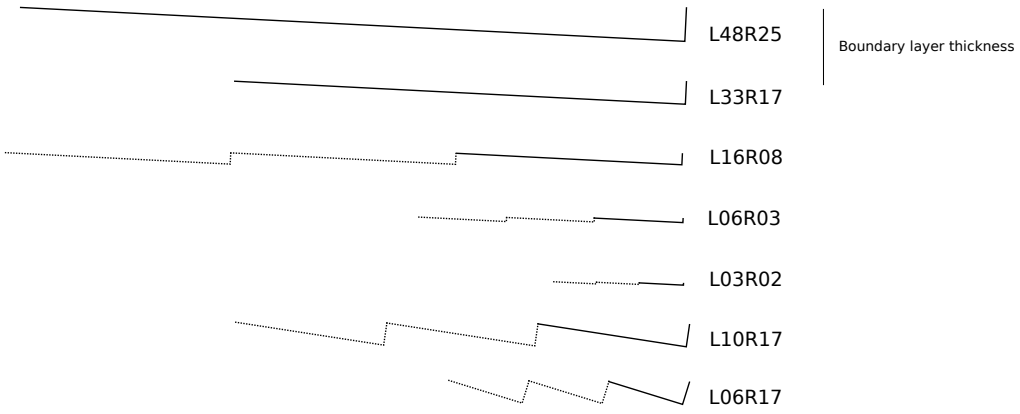

Figure 3.6: Wind tunnel insert geometries

See figure 3.6 for a comparison on the sizes of the test cases. The figure is to scale, and the boundary layer thickness is also shown. The cavity and L33R17C geometry are not shown, since they have the same roughness height as the L33R17 geometry. For a number of geometries extra elements are shown to give a better indication of the shape of the elements.

Chapter 4

Experimental and Numerical set-up

In this chapter the experimental and numerical set-up is discussed. This chapter starts of with a discussion of the test facilities and test set-up. In the experimental part of the research measurements with Schlieren and PIV where done. The general working principle of both techniques will be discussed. The numerical set-up and data reduction techniques are also discussed in this chapter.

4.1 Test facility

For the experimental test campaign, a supersonic wind tunnel at the TU Delft was used. The tunnel (ST-15) is a blow down facility.

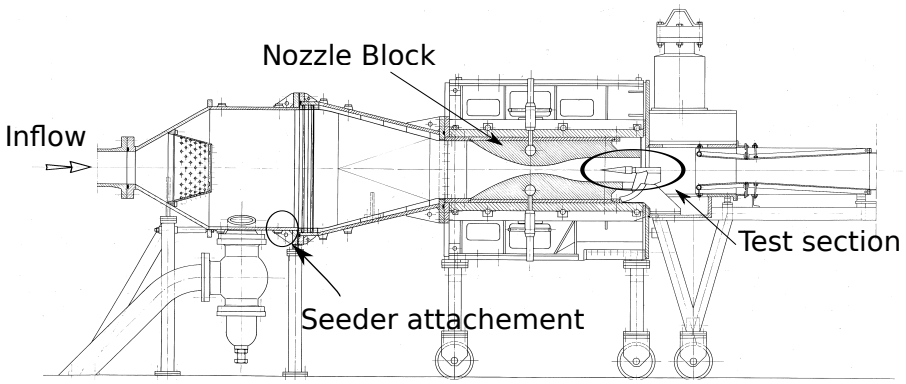

Figure 4.1: Overview of the supersonic wind tunnel ST-15

Figure 4.1 shows an overview of the tunnel. The Mach number can be changed by means of a number of different nozzle blocks. Mach numbers that can currently be achieved are: 1.5, 2, 2.5 and 3 respectively. The total temperature is determined by the temperature of the pressure vessel, which is outside and is typically between 280 and 290 Kelvin.

4.2 Test geometry

The rough wall geometries cannot be integrated into the wind tunnel wall itself. Therefore, plate inserts where fabricated that could be attached to the wind tunnel wall. These plates are 15 cm wide, and 18 cm long. The test section itself is 20 cm long. These plates have to be attached into the nozzle geometry and therefore a front and back insert where made to hold these plates in the tunnel.

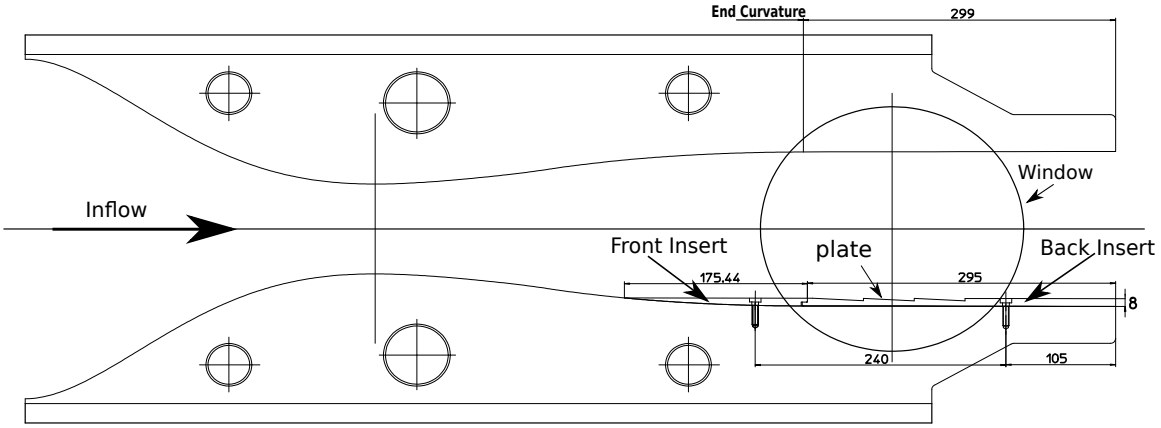

Figure 4.2: Wind tunnel geometry with test geometry

In figure 4.2 one can see the geometry of the wind tunnel with one of the test geometries inserted, dimensions shown are in mm. The front and back insert and the plate can be seen. Roughness elements are on the top side of the plate. The thickness of the insert is 8 mm. The placement of the test plate in the tunnel has as a consequence that the flow will be turned away from the ideal nozzle contour. A shock will appear at the front of the insert. Because of this the front insert has been made 17 cm long to make sure that the boundary layer can recover to a standard boundary layer.

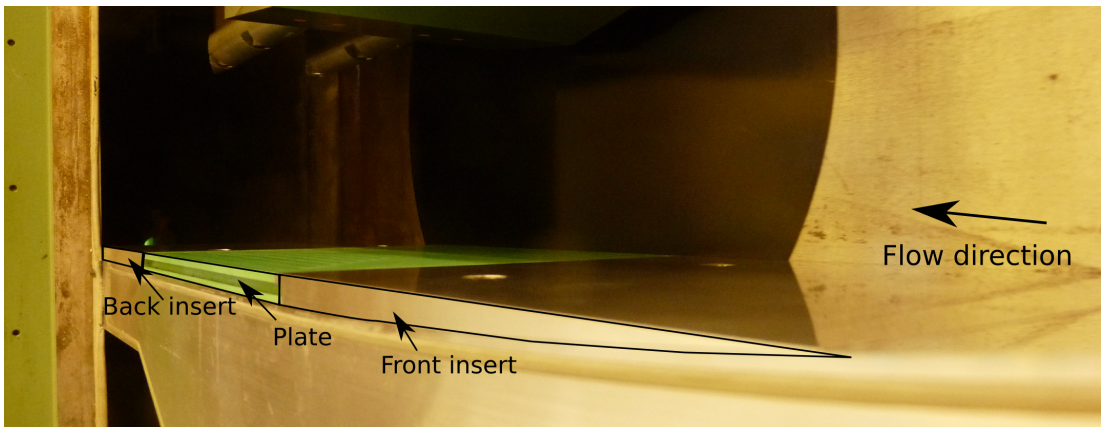

Figure 4.3: Photo Wind tunnel with test geometry

Figure 4.3 shows the wind tunnel with the inserts and plate. The flow runs from right to left in the figure. It can be seen that the flow first runs over the front insert, then transitions onto the plate, and then to the back insert. Due to manufacturing imperfections the transition from front insert to the plate was not smooth, therefore in a number of results, expansion waves will be seen at this point. The step is largest in the flat reference case. On the sides of the tunnel the step is minimal while in the middle it is largest. On the point where it is largest it is roughly 0.5 mm. The geometries of the plates fabricated can be found in appendix A.

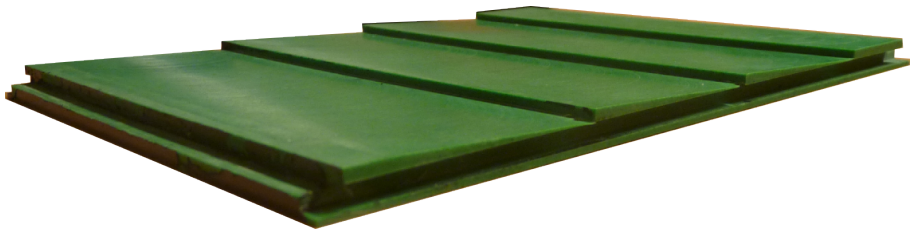

Figure 4.4: Fabricated geometries

Figure 4.4 shows the plate for the L48R25 geometry. Three steps can be seen and an edge at the front and back to hold the plate in place.

4.3 Reference coordinate frame

In this research two slightly different coordinate reference frames have been used, a PIV reference frame, and a CFD reference frame.

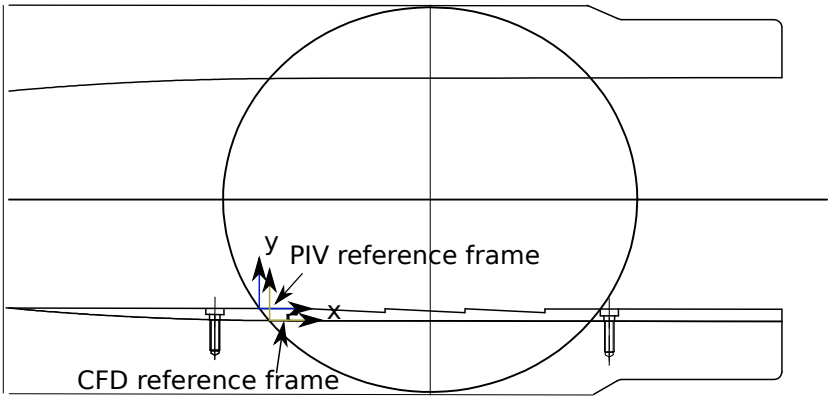

Figure 4.5: Reference frames

Figure 4.5 shows both the reference frames. The origin of the PIV reference frame is situated at the intersection of the insert with the window. The CFD reference frame is situated at the intersection of the nozzle with the window. The difference in y direction is 8 mm, and 4.8 mm in x direction. In the CFD reference frame the elements start at the point 0,0. For the PIV reference frame the plate starts at an x position of 25 mm. In any comparison between CFD and PIV there has been corrected for this 25 mm. This makes that in any comparison between PIV and CFD the same number of elements have been passed and comparisons are done on the same position within an element.

In this report figures where only CFD data is shown, are printed in the CFD reference frame. Figures with only PIV data are shown in the PIV reference frame. For PIV/CFD comparisons the CFD data is transformed to the PIV reference frame, and the PIV frame is used.

4.4 Schlieren

First inspection of the flow field was done by Schlieren visualization. In Schlieren measurements density gradients are visualized due to the change in refractive index. Observing this change in refraction dark and light areas indicate places of compression and expansion. In the light of this study Schlieren measurements where preformed to have a global overview of the flow field and therefore to check if the overall flow field behaved as expected. In the current section an overview of the Schlieren set-up will be given.

4.4.1 Set-up

The concept of a Schlieren measurement is based on the dependence of the refractive index on the density of the flow. For an optical medium the Gladstone-Dale relation states that the refractive index is a function of the density according to equation (4.1) .

$$n = \frac{c_0}{c} = 1 + K\rho \tag{4.1}$$

In equation (4.1) n is the refractive index, c_0 is the speed of light in vacuum c is the speed of light in the optical medium considered, K is the Gladstone-Dale constant and ρ is the density of the optical medium. The Gladstone-Dale constant is a constant for a specific gas. A Schlieren system measures changes in refractive index, and by equation (4.1) these are a measure for changes in density. Details can be found in [15].

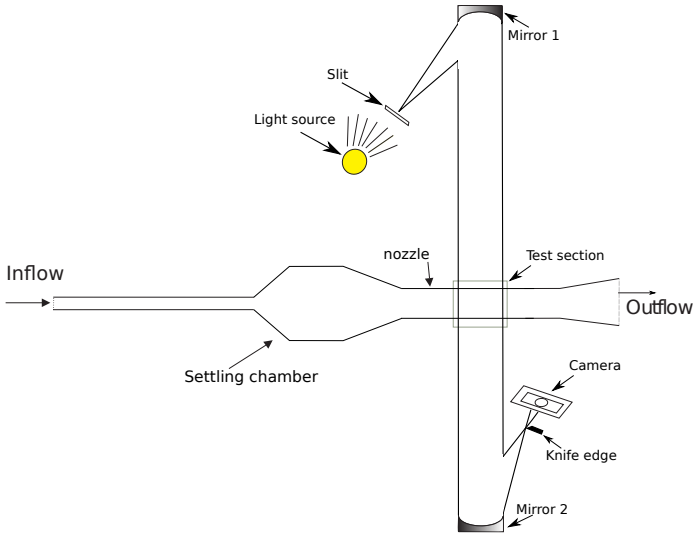

Figure 4.6: General Schlieren set-up

Figure 4.6 shows a top view of the wind tunnel with the Schlieren set-up. The light source produces light which passed through the slit to create a point light source. The slit has to be in the focal distance of mirror 1. Because the slit is in the focal point, mirror 1 creates a collimated light beam. The parallel light from mirror 1 will now pass through the test section where it will be distorted by the existing flow features. The distorted light beam is then reflected by a second parabolic mirror (Mirror 2) focusing the light on a recording device. Mirror 2 has the same focal distance as Mirror 1. The distance between Mirror 1 and Mirror 2 determines the dynamic range of the system. The knife edge is positioned in the focal point of Mirror 2. The knife edge controls the sensitivity of the system.

4.5 Particle Image Velocimetry

In the current investigation Particle image Velocimetry (PIV) measurements have been made to acquire velocity data to be used for CFD validation. PIV is a non-intrusive measurement technique and therefore this technique is a good option to acquire flow data. In the current section the set-up of the PIV measurements will be given. In the first section a description will be given of the geometrical set-up of the experiment. The next section will describe the laser seeding and the cameras used. The last section describes the data processing.

4.5.1 PIV theory

In a PIV measurement seeding particles are inserted into the flow. These particles, are illuminated by a laser at 2 time instances. The time separation is such that the particle displacement can be determined from the images. For a good velocity determination the particles should have the same velocity as the flow. The difference between the flow velocity and the particle velocity can according to [36] be written as:

$$\frac{d\overline{U}_p}{dt} = \frac{\overline{U}_f - \overline{U}_p}{\tau_f}$$

Where U_p is the velocity of the particle, U_f is the velocity of the flow and τ_f is the relaxation time of the particle. As a first approximation the assumption is made the velocity difference is small enough that stokes drag is the main cause of drag. Then it can be derived that the relation time is

$$\tau_f = d_p^2 \frac{\rho_p}{18\mu} \tag{4.2}$$

Where d_p is the diameter of the particle, ρ_p is the density of the particle and μ is the viscosity of the fluid.

When the velocity undergoes a step change the difference in velocity between the particle and the flow will follow a exponential decay:

$$\bar{U}_p = \bar{U}_2 + \triangle\bar{U}e^{-t/\tau_p}$$

Where $\bar{U}_2$ is the reached velocity and $\triangle\bar{U}$ is the step change in the velocity. When the flow

passes through a shock wave there is a large velocity gradient. Therefore in most cases the particle will lag the speed of the flow through a large gradient. Thus measuring the velocity in a shock wave can results in erroneous measurements.

When illuminating these particles with a laser images can be taken. The images are divided into sub domains, called windows. A cross correlation between the image pairs is done on each window to determine the particle displacement. This particle displacement is the average particle displacement in that window.

With the particle displacement, the time separation between the image pairs and the calibration of the image the velocity can be calculated. Reynolds stresses can be calculated by a statistical analysis on multiple velocity fields. As will be shown in chapter 5, for the calculation of reliable Reynolds stresses, a large set of image pairs is needed. To obtain a velocity field with a small vector pitch all the available image pairs can be combined with a sum of correlation. Hereby a single velocity field with small vector pitch is calculated from a large number of image pairs.

4.5.2 Set-up

For the positioning of the PIV system, the positioning of the cameras and the positioning of the laser should be considered. The positioning of the cameras directly determines the magnification of the images. The laser generates the laser sheet which is used for illuminating the particles.

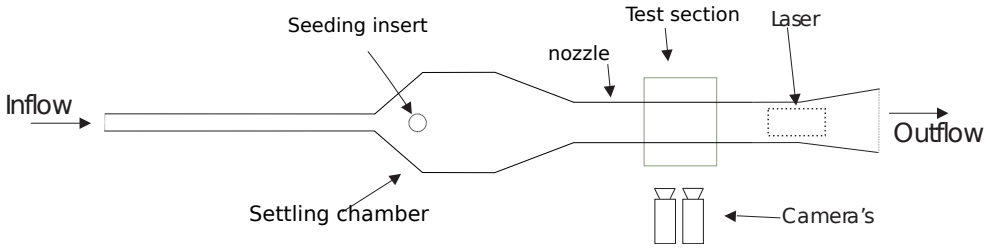

Figure 4.7: Top view of PIV set-up

Figure 4.7 shows a top view of the used wind-tunnel, the cameras and the laser. The inflow is on the left hand side of the figure. The seeding inset is directed upstream to improve mixing of the seeding particles with the flow. To increase the size of the field of view two cameras were used, as can be seen in the figure. The laser is situated down-steam, under the tunnel. The laser light is directed into the test-section via a number of mirrors.

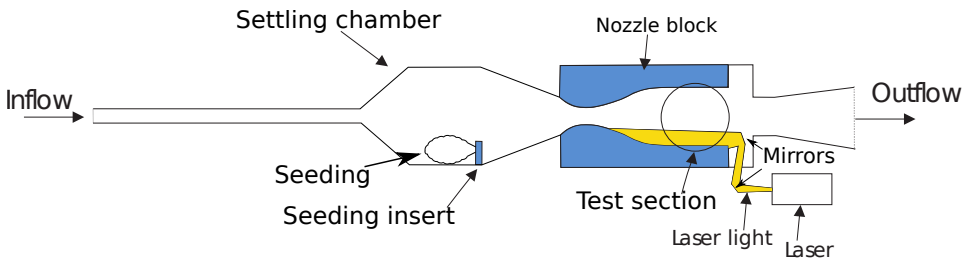

Figure 4.8: Side view of PIV set-up

In figure 4.8 one can see a side view of of the set-up. As can be seen the laser sheet is reflected via two mirrors into the test section. From figure 4.8 one can see the seeding inset in the settling chamber, after which a a nozzle contour can be seen in the test section. In the window section the insets for this investigation have been placed.

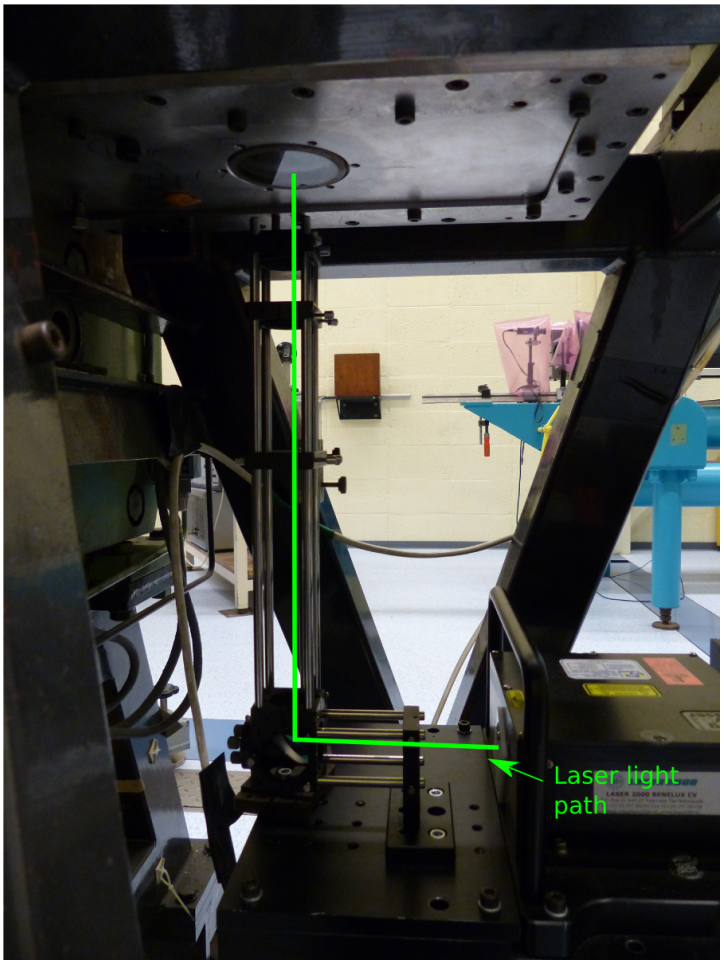

Figure 4.9: Laser and mirrors.

Figure 4.9 shows the laser and the mirrors and reflect the laser light into the tunnel. On the right bottom is the laser. On set of reflective mirrors can be seen which reflect the laser light upwards into the tunnel.

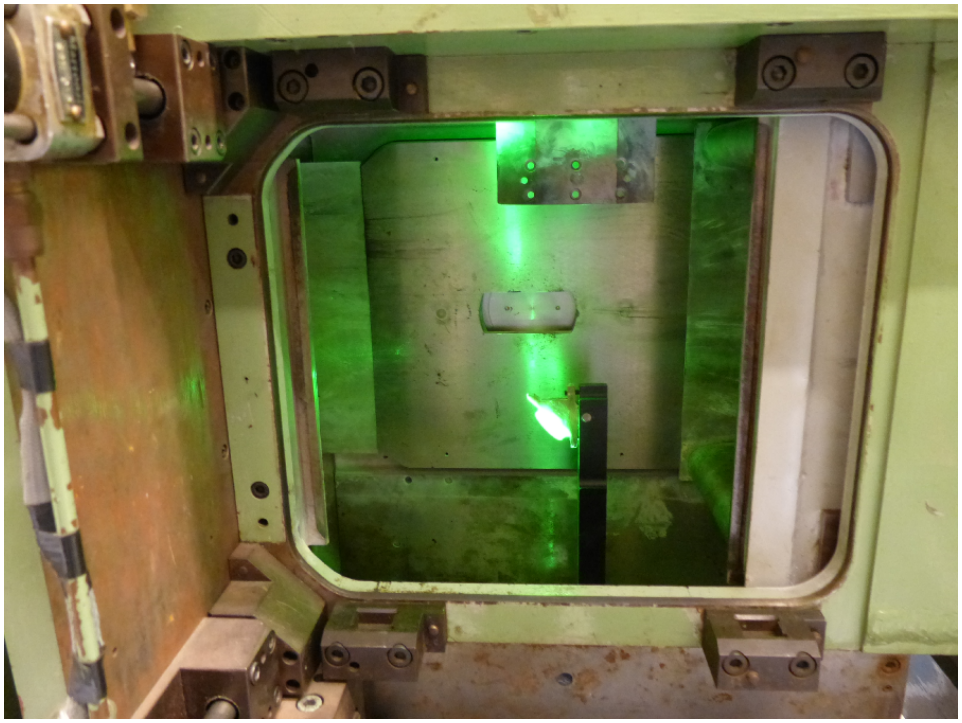

Figure 4.10: Reflective mirror in the tunnel

Figure 4.10 shows the reflective mirror in the test section which reflects the light upstream, see figure 4.8. The flow is from left to right in figure 4.10. The mirror that reflects the light beam upstream is at the same height as the wall. Therefore the laser sheet is parallel to the top of the roughness elements. This means that no velocity information can be obtained inside the elements.

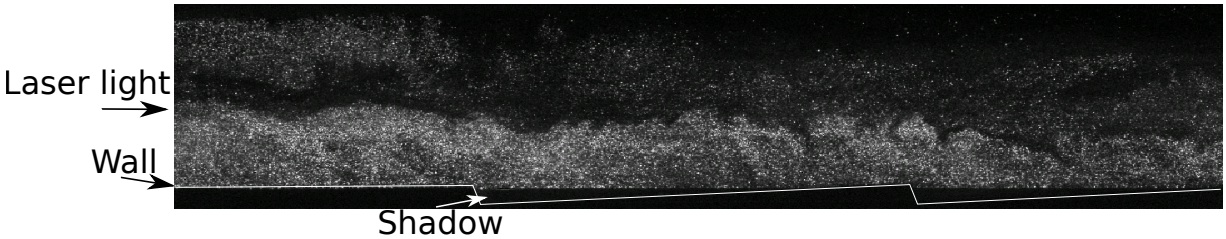

Figure 4.11: Laser lighting

In figure 4.11 the L48R25 geometry is shown with the wall. It can be seen that the laser

light goes over the elements, but does not enter into the elements.

4.5.3 Field of view

To measure the velocity fields four field of views have been been studied.

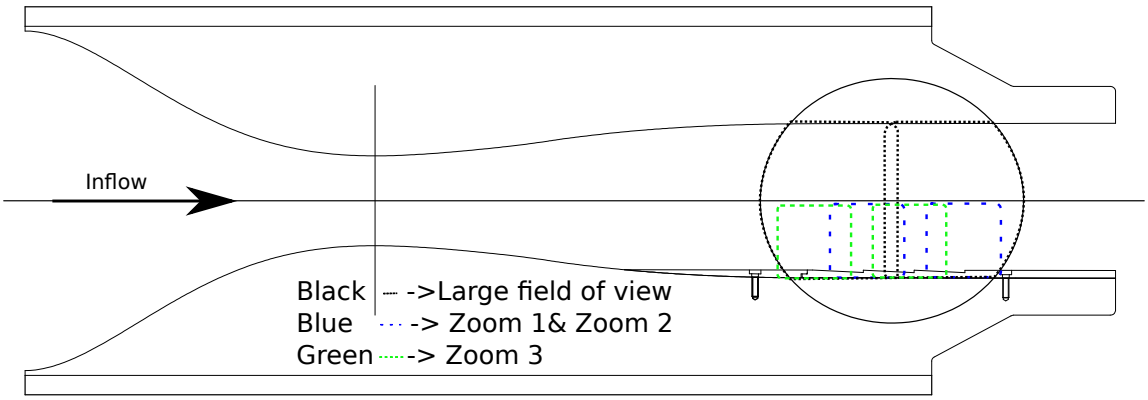

Figure 4.12: Field of view

Figure 4.12 shows the distribution of the field of views. Every rectangle represents a field of view. There are two of each rectangle since two camera's where used for each zoom level. Large field of view measurements have been used to have a complete overviews of the 15 by 20 cm test section. In this case there was an overlap between the two images, so they could be merged. The 1st and 2nd zoom images have been made with one camera on the trailing edge of the roughness elements, and the other in the middle of the test section. For the 3rd zoom field of view the first camera was on the inflow part of the test section, and the second camera in the middle of the test section. With this field of view only measurements where made of the flat reference geometry.

Table 4.1: Sizes field of views

Zoom	Size field of view	Tested geometries
Large field of view	111x59.9 mm	L48R25, Flat, L06R17
Zoom 1	41.55x22.44 mm	L48R25, L33R17, L16R08, L06R03, L03R02, L33R17
zoom 2	34.5x18.8 mm	Flat, Cavity, L10R17, L06R17
zoom 3	30.36x10.11 mm	Flat

Table 4.1 shows the fields of views used. They show a decrease in size, for an increase in magnification.

4.5.4 Seeding Laser and Cameras

To make PIV images the seeding and laser work closely together to generate a system of particles and there illumination.

For the seeding the oily substance DEHS was used. DEHS was vaporised using a laskin nozzle seeding generator [32]. Diameter of the particles varies between 1 and 3 micron. The relaxation time of the particles is 2.92 10^{-5} sec according to equation 4.2.

The laser used is a double pulse laser from Quantel, operating at 532 nm. The system is a double-pulse Nd:YAG system. The laser sheet was operated at a thickness of 3.2 mm. The thickness was selected since it was in the depth of focus of the camera, and a thicker laser light yields more imaged particles. The flow is assumed to be 2D and therefore the errors made due to cross flow will be small. For further details on the laser see, [33].

To record the seeding particles two Imager intense cameras from Lavision [27] have been used. This camera is a one Megapixel camera specially designed for PIV experiments. The CCD of the camera is able to make two images in quick succession. This ability makes that from this image pair the velocity fields can be calculated. In table 4.2 one can see all the settings used.

Table 4.2: Camera set-up

Test	camera lens	f#	Distance camera to tunnel (cm)	M	$\triangle t\ \mu s$
Large field of view	60 mm	5.3	112.5	0.06	3
Zoom 1	60 mm	11	37.5	0.16	1
zoom 2	60 mm	11	20.5	0.24	1
zoom 3	100 mm	11	13.7	0.31	0.9

Test	mm/pix	FOV (pix^2)
Large field of view	1.1e-1	1009x545
Zoom 1	3.9e-2	1065*575
zoom 2	2.7e-2	1280*696
zoom 3	2.0e-2	1518*506

As can be seen in Table 4.2 the set-up has been slightly altered during the multiple tests. The distance from the camera to the tunnel is the distance from the camera lens to the tunnel window. $\triangle t$ is the time separation between the image pairs, and mm/pix is the zoom.

4.5.5 Image pre-processing

The PIV images obtained with the apparatus described above yields a picture that can already be used to determine the velocity fields. To obtain better velocity information image processing has been applied to obtain a clearer image for correlation. The processing applied consisted of subtracting the minimum of the image, multiplying the pixel values by the value of 100, and dividing by the average pixel value. All these operations are used to obtain an image with a high contrast. An example of an image obtained with this procedure can be seen in figure 4.13.

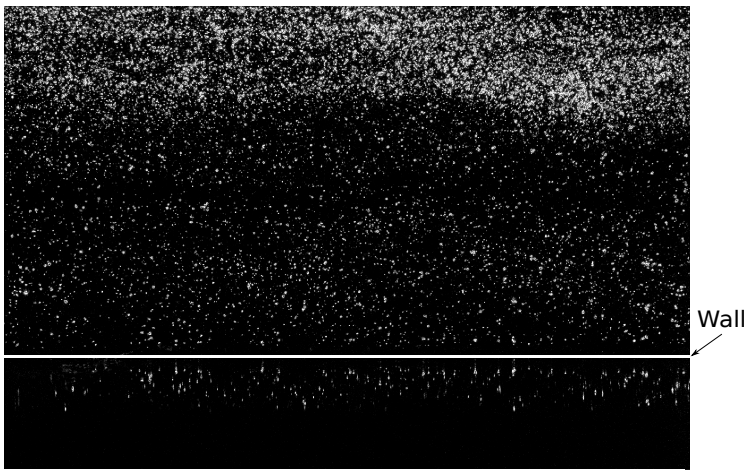

Figure 4.13: PIV Image after processing

In figure 4.13 the wall has been shown, and the PIV particles can be clearly distinguished. The particles shown below the wall are reflections on the surface of the particles above.

4.5.6 Image processing

The processing of the PIV images has been done with the commercial software DaVis from Lavision. This program includes a set of computational routines to extract information from the PIV images. the main routine is an iterative window deformation method with Gaussian weighing. Two variations of the method were applied, standard PIV correlation, and Sum of correlations. In standard PIV the correlation is done on one image pair, while for sum of correlation all available image pairs are used. For the processing of the images the following data was used

Correlation method	Window size	overlap	Resulting Vector pitch (mm/vector)
Standard	32x32	75%	0.1
Sum of correlations	8x8	75%	0.07

Table 4.3: Processing data

For the sum of correlations and the standard processing the same setting where used, apart from the size of the windows. As can be seen the application of the sum of correlations yields a decrease in the vector pitch.

For the zoom 3 measurements 400 images were acquired for statistical correlation, for the other zoom levels 200 images were acquired for each geometry. For data processing mean fluctuating values are calculated for comparison. For the calculation of the mean velocity values data is only included if inside a range of 3 standard deviations from the mean. All data shown in this report are mean values. Reynolds stresses are calculated with all image pairs and with the setting as show in table 4.3.

4.6 Computational Fluid Dynamics simulations

In this section the set up of the computational fluid dynamics part, hereafter abbreviated with CFD will be discussed. This research project was divided into a computational and an experimental part. This was done to be able to validate the CFD results with the experimental data. In CFD the Navier Stokes equations are solved on a given grid. In the current research the choice was made to solve the flow over the roughness elements using the RANS (Reynolds averaged Navier Stokes) equations. In the RANS equations the time average of the quantities are solved and the turbulent fluctuations are modeled. In this section the domain, grid, turbulence model and the boundary conditions are described.

4.6.1 Computational domain

The domain simulated is half of the wind tunnel nozzle and test section. It was decided to include the nozzle geometry, including the throat in order to have the same inflow conditions, as those that would occur in the wind tunnel. In the computations the flow starts subsonic, becomes supersonic in the throat, and is Mach 2 when it reaches the test section.

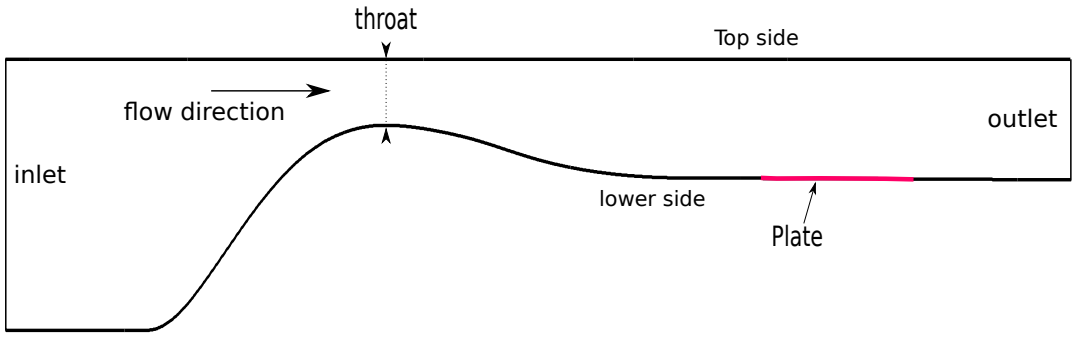

Figure 4.14: Inner half-profile of the wind tunnel

The profile of the computational domain is shown in figure 4.14. The inlet is 17 cm, the throat is 4.13 cm, and the outlet is 7.45 cm. All the test geometries are placed in the test section. As can be seen only half of the test section is modeled. This is to reduce the size of the computational domain. In the simulations a symmetry condition will be set on the top side of the half channel for proper reproduction of the size of the windtunnel. In the wind tunnel there is no reflection symmetry since there is no roughness on the top side of the channel. However any disturbance that the roughness on the top side of the computational domain generates will not impact the test section.

The contour of the nozzle was described by a number of points. On first inspection these points make up a continuous contour, but further inspection revealed discontinuities in the first and second derivative of the nozzle contour. These discontinuities make that non physical-shocks are formed in the test section. These shocks are non-physical since no shocks can be observed in the experiments.

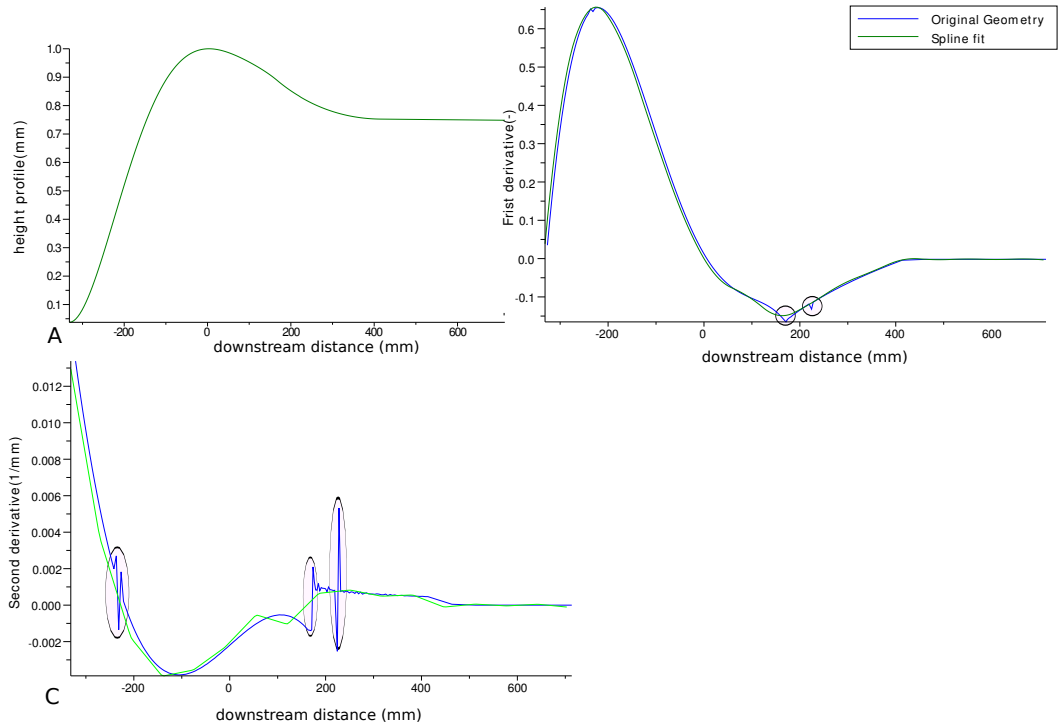

Figure 4.15: Tunnel contour (A), First derivate contour (B), Second derivative contour (C)

Figure 4.15 shows the tunnel contour and it's first and second derivatives, and a spline fit to this contour. The start of the test section is at an x position of 331.55 mm in the top left(A) the tunnel contour is displayed, which at initial inspection has no discontinuities. The top plot (B) right shows the first derivate. Discontinuities appear a 3 locations. The bottom left plot (C) shows the second derivative also with discontinuities at the same locations. These discontinuities are problematic since they cause shocks to form in the computational domain. These shocks are not seen in the wind tunnel and and therefore the profile should be such that these shocks are not produced. To achieve this profile a spline with given break points is used on the original points. The algorithm used to spline fit the contour is the Scilab implementation of the least squares spline algorithm by C. De Boor and A.H. Morris, Scilab function lsq_splin. There original code is included in the NSWC fortran library. Break point given to this algorithm are: [0 95 190 285 380 475 530 665 760 855 950 1045]. It can be seen that the used spline fit is able to make a continuous transition on the points were the original data shows discontinuities.

4.6.2 Mesh

A mesh is needed to transform the continuous geometry into a discrete domain on which the flow governing equations can be solved.

Three element distribution strategies have been applied to mesh the geometry. The L48R25, L33R17, L10R17 and L06R17 cases have been meshed with refinement in front of the steps in the geometry. Since these geometries are big with respect to the rest of the geometry set, this was deemed enough. See figure 4.16 for the mesh distribution in the L06R17 case.

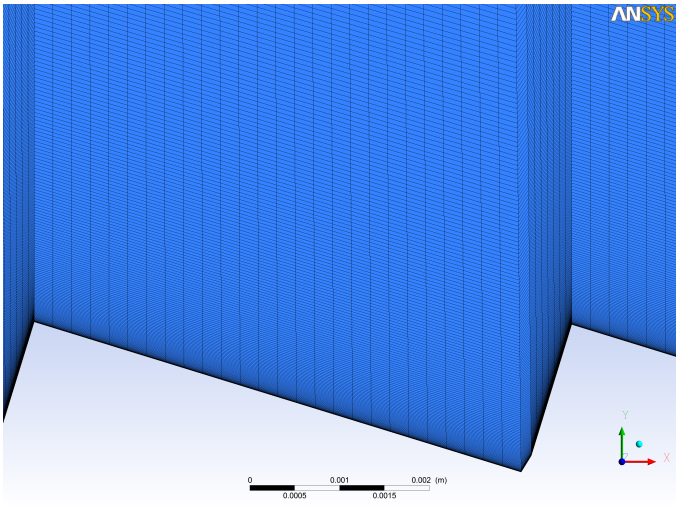

Figure 4.16: Elements distribution L06R17 case

In figure 4.16 one can see that the element distribution was chosen such that the number of elements was more dense at the forward facing step. Due to the chosen element distribution strategy obtaining a 90 degree angle at the lower bottom required a large number of elements. Therefore the small deviation from this 90 degree angle in one cell was found to be acceptable. Since the difference between the mesh and a 90 degree angle are small and the difference between the geometry and the mesh applies to one cell it was deemed that the influence of the deviation is small. Also flow velocities in section are small and therefore the difference will have negligible impact. For the L16R08, full and L06R03 geometries a multi-stage refinement of the mesh was chosen.

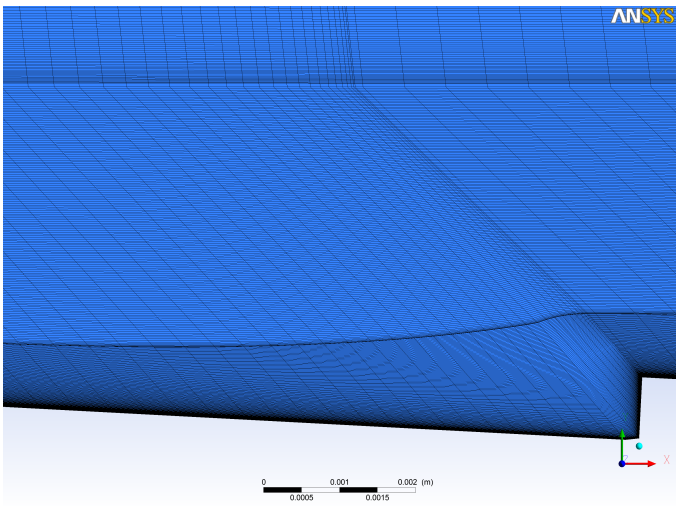

Figure 4.17: L16R08 Geometry mesh

Figure 4.17 shows the L16R08 geometry mesh. Three refinements can be seen. On the top of the figures the mesh in the free stream flow field can be seen. The middle of the figures shows a refined piece of mesh. Near the wall the densest mesh has been applied. For the geometries with a cavity the shear layer that is formed at the top of the cavity is the most important part that should be meshed.

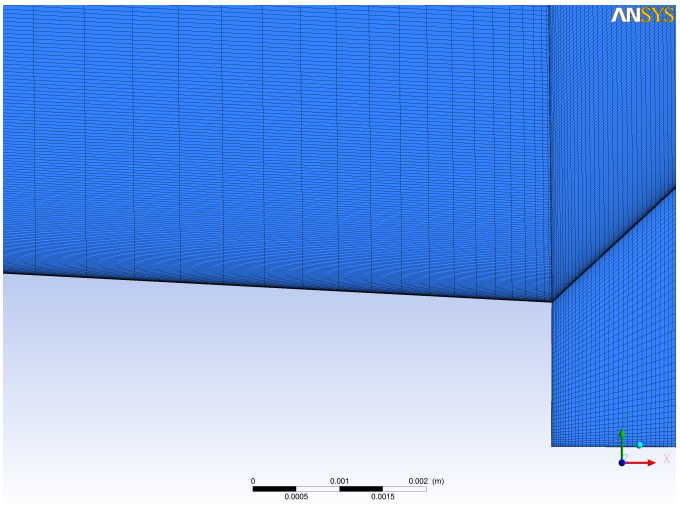

Figure 4.18: L33R17C geometry mesh

In figure 4.18 the mesh of the L33R17C geometry is shown. It illustrates that the biggest refinement was produced on top of the cavity, and on the shear layer. The amount of cells used per simulation is dependent on the simulated roughness profile.

Table 4.4: Mesh Statistics

Stimulation	Nodes	Elements
Flat plate	1883000	939456
L48R25	1694400	845189
L33R17	4531304	2262325
L16R08	2671300	1332584
L06R03	2998372	1494888
L03R02	-	-
Cavity	1352680	939456
L33R17C	2192400	1092264
Full	2348080	1171482
L10R17	1891200	943425
L06R17	3222800	1222776

Table 4.4 shows the mesh statistics. For the L03R02 geometry no converged solution could be obtained, and therefore the mesh statistics are not displayed. The mesh statistics in table 4.4 have been obtained by comparing all cases to the flat plate reference case. Grid convergence of the flat plate reference case was investigated by means of a grid convergence study.

Simulation	Nodes	Elements
Coarse	478000	237606
Nominal	1883000	939456
Fine resolution	3690000	1841156

The full shape (test point 9) has not been tested in the wind tunnel due to problems in the manufacturing of the curvatures in the geometry.

Table 4.5: Grid data flat plate

Table 4.5 shows the three meshes used for determining grid convergence. The main direction for the increase in the number of cells is the y direction. A coarse mesh, the nominal mesh, and a fine resolution mesh. The data is compared on the wall of the test section for the three cases. To determine if convergence is achieved the difference is calculated between the the coarse mesh, and the fine resolution mesh, and between the nominal mesh and the fine resolution mesh. The difference for both cases is defined here as:

$$Difference = \frac{Case_{mean} - Grid\,Convergance_{mean}}{Grid\,Convergance_{mean}}$$

Where the data is obtained at the wall of the test section.

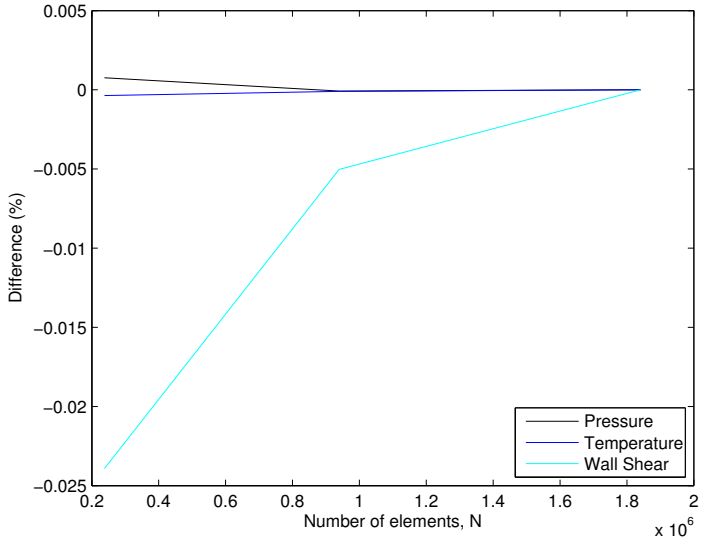

Figure 4.19: Grid convergence study

Figure 4.19 shows the difference for the 3 cases considered. Since the differences are calculated with respect to the Grid convergence case the difference for this case is zero. A difference that decreases with in increase in the number of elements can be seen. For the test case mesh the largest error is -0.5 % for the wall shear. It is therefore concluded that this case has converged. From table 4.4 one can see that the Cavity and L48R25 cases are the 2 cases that have fewer elements then the flat plate geometry.

A grid convergence simulation was done for the L48R25 geometry to show convergence within the elements. The fine grid has 2099200 nodes and 1047489 elements.

Variable	Difference (%)
Temperature	-0.006
Pressure	0.0017
Wall shear	-0.7

Table 4.6: Grid convergence L48R25 geometry

Table 4.19 shows the difference between the nominal, and fine grid simulation for the L48R25 run. As can be seen the largest difference is at the wall shear were the difference is -0.7 %. Therefore it is concluded that convergence is achieved.

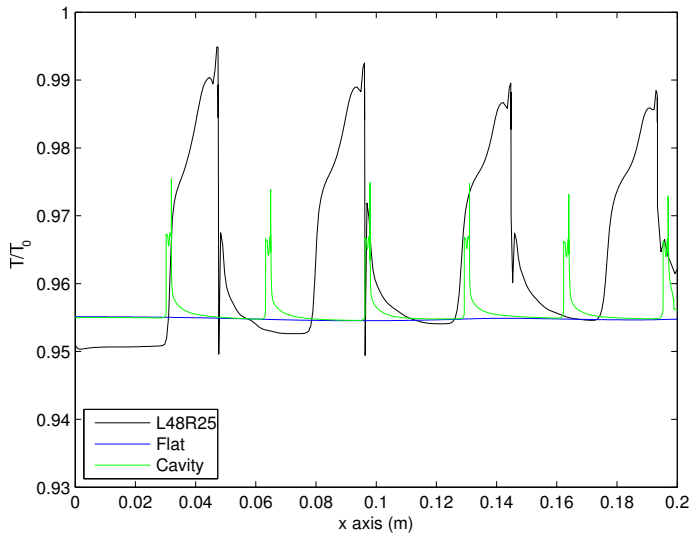

Figure 4.20: Temperature lower wall

Figure 4.20 shows the temperature on the lower wall of the flat plate, cavity and L48R25 case. For the cavity it is expected that flow plate flow occurs on the flat regions. It can be seen that this is achieved since the temperature is close to the flat plate value.

For the L48R25 geometry the temperature can be validated in the first element since it involves a expansion fan. Standard analytical results can be used to calculate the temperature jump over the expansion fan, see for example Anderson [26] for analytical relations. It was calculated that the temperature after the expansion fan should be $0.95T_0$, which is the temperature shown in figure 4.20.

The inflow conditions show grid convergence and the roughness elements of the L48R25 geometry show grid convergence. The results for the cavity geometry show similarity with the converged flat plate simulation and all other cases have a denser mesh then the last mentioned geometries. Therefore the conclusion is drawn that t he simulations have converged.

Since this is the case it has been concluded that all geometries have converged. Convergence during a run was achieved by making sure that the change in RMS value of the residuals went to zero.

Because no wall functions are used, the wall resolution should be high to resolve all flow characteristics. For a good wall resolution y^+ should be smaller than 1 [3]. See table 4.7 for the average y^+ values in the test section. y^+ is defined as $y^+ = \frac{u_\tau \triangle n}{\nu}$ where u_τ is the friction velocity, Δn is the distance from the wall to the first node and ν is the kinematic viscosity.

The average y^+ in the current simulation is 0.35. The y^+ varies between plus or minus 0.1 of the average value. In table 4.7 the average y^+ values can be seen. Apart from the cavity geometry all the geometries have an average y^+ value smaller then one. For the cavity geometry is was noted that also in the cavity the value of y^+ is smaller then one. Outside the cavity however the flat plate sections follow the same trend as the reference geometry, and so it was deemed not necessary to refine the mesh further. Table 4.7 also shows the RMS value of the residual in the x direction. This is a measure for the error in the simulation. As can be seen the errors are small.

Table 4.7: Average y^+ in test section, RMS x residue

Stimulation	Average y^+	RMS x residual
Flat plate	0.2347	4.2e-7
L48R25	0.2347	3.7e-7
L33R17	0.4915	1.0e-6
L16R08	0.0763	5.7e-5
L06R03	0.0777	3.6e-6
L03R02	-	-
Cavity	1.6593	1.2e-8
L33R17C	0.1522	5.1e-7
Original geometry	0.1206	4.7e-7
L10R17	0.0961	1.5e-6
L06R17	0.0912	4.0e-7

4.6.2.1 Entire tunnel mesh

As was described in the previous section the CFD will be done in a geometry, which is described by half of the wind tunnel geometry used for experiments. As was described the rough wall geometries cannot be put into the wall of the wind tunnel during the experiments. Therefore an insert was made to hold the test shapes. A simulation has been made of the geometry as that will be present in the wind tunnel, see figure 4.2. See figure 4.21 for the geometry.

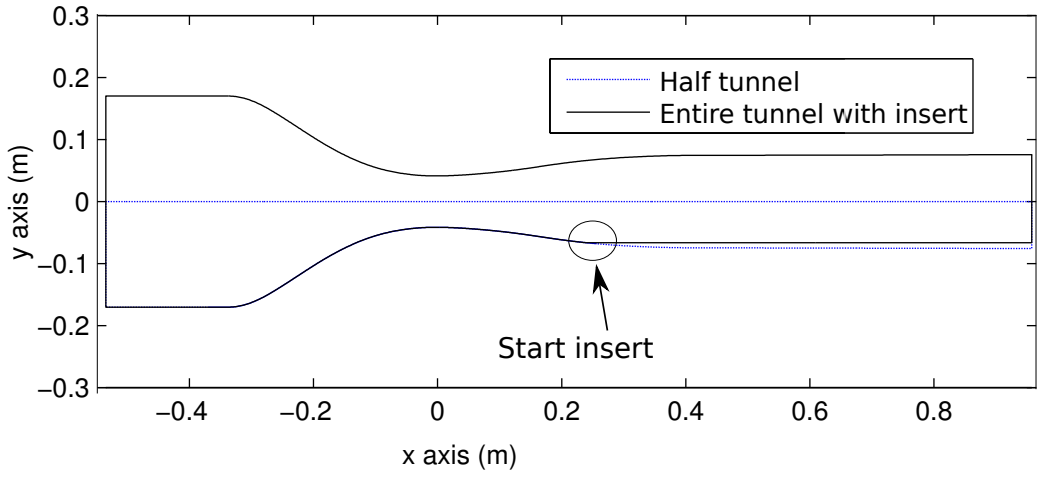

Figure 4.21: Whole tunnel geometry

In figure 4.21 the entire tunnel and half tunnel geometry is displayed. The start point of the insert is shown The transition point where the geometry changes from a nozzle contour to a flat plate is displayed. The mesh used in the y direction is a full cosine mesh, meaning that the size of the elements gets smaller when approaching the wall. This simulation has been made as a reference to check if the flow in the half tunnel geometry behalves the same as the flow that will be tested in the wind tunnel. Average y^+ in the test section is 0.12. The number of nodes for this model is 1250000, and the number of Elements is 1222776.

4.6.3 Boundary conditions

The boundary conditions on the inlet concerned a total pressure of 3.2 bar, and a total temperature of 290 Kelvin. At the outlet two boundary conditions where used. At the start of a simulation a subsonic boundary condition has to be set on the outlet, with a pressure of 0.05 bar. When supersonic flow was established in the test section, the boundary condition was switched to supersonic. This procedure was followed since a supersonic boundary condition with subsonic flow in the entire domain would mean a crash of the solver. On the upper-boundary a symmetry condition was imposed. On the lower boundary a no-slip condition was set.

4.6.4 Models

4.6.4.1 Reynolds Averaged Navier-Stokes equations The equations that where solved on the grid described above where the Reynolds Averaged Navier-Stokes equations (RANS). The choice for this set of equations was made since solutions can be obtained within a reasonable time frame. The full equations can be shown in [12].
When one compares the full Navier-Stokes equations to the RANS equations one will see that the equations are almost the same, when the variables are replaced by their time-averaged counterparts. Because of the averaging the equations become dependent upon the turbulent inertia tensor: $\overline{u_i' u_j'}$. This term has the unit of stress, and is therefore called the Reynolds stress term. This term has to be modeled with a turbulence model.

4.6.4.2 Turbulence In RANS simulations the turbulent fluctuations in the flow are modeled by means of turbulence models. Two models have been selected, the shear stress transport (SST) model [34] and the BSL Reynolds stress model [6] These models serve two goals. The SST model will be used for all calculation, due to its popularity, and it is known to give good results under a wide range of circumstances.

The SST model is a 2 equation model eddy viscosity model. At the wall this model uses a $\kappa - \omega$ approach, which in the free stream a $\kappa - \epsilon$ approach is used. A $\kappa - \omega$ approach yields

the ability to integrate the equation to the wall, and the ability to use a low Reynolds number approach. The $\kappa - \omega$ approach has shortcomings in simulating free stream flow, and therefore a $\kappa - \epsilon$ approach is used in the free stream. Both approaches are combined with the usage of blending functions.

The shear stress transport model yields good results, but no Reynolds stress information. To validate the inflow conditions in the test section knowledge of the Reynolds stress is preferable, since these can be compared with experimental results. For this goal the BSL Reynolds stress model (RSM) was chosen. In this model also the Reynolds stress equations are solved and therefore also the Reynolds stress will be know. The main part of BSL and SST model are the same up to a limiter on the eddy viscosity which is present in the SST model, but not in the BSL model. Since the BSL Reynolds stress model was the only available RSM that combines a $\kappa - \omega$ with a $\kappa - \epsilon$ approach this model was taken. The equations for the BSL model can be found in [6].

For the turbulence numerics and the advection scheme the high resolution scheme is used, see [4] for details.

4.6.4.3 Viscosity and thermal conductivity

The viscosity and thermal conductivity where modeled by means of a Sutherland law [12], see equation (4.3).

$$\frac{\mu}{\mu_{ref}} \approx \left(\frac{T}{T_{ref}}\right)^{3/2} \frac{T_{ref} + S}{T + S} \tag{4.3}$$

Equation (4.3) is written down for the viscosity, but is also valid for thermal conductivity, when using the appropriate constants. The constants used for the viscosity are: $T_{ref} =$ 273 Kelvin, μ_{ref} is 1.716e-5 $N \cdot s/m^2$, Sutherland constant 111 Kelvin. For the thermal conductivity the constants are: $T_{ref} =$ 273 Kelvin, k_{ref} 0.0241 $N \cdot s/m^2$, Sutherland constant 111 Kelvin.

4.6.4.4 Materials, and heat transfer

For heat transfer the total energy model is selected [5]. This model describes the transport of enthalpy, and takes kinetic effects into account. The model is based upon a turbulent Prandtl number approach. For the total energy model viscous work was also included. Air is modeled as an ideal gas.

4.7 Data Reduction

In this report a number of quantities are used for comparison. These include the boundary layer thickness, momentum thickness, log law constants, and density for the PIV. In this section there methods of calculation is be discussed.

In the case of the CFD density, velocity and pressure information is available anywhere in the flow field. For a number of boundary layer parameters density information is needed. For PIV this is not available, and therefore it has to be computed. To to this a 2 way strategy is employed were first the temperature is computed by means of a Crocco-bussemann relation. A Crocco-bussemann relation for an adiabatic wall is given by:

$$T = T_{wad} - r\frac{u^2}{2C_p} \tag{4.4}$$

Where T_{wad} is the adiabatic wall temperature, see White [12] for details. In equation (4.4) T is the temperature. $T_{w_{ad}}$ is the adiabatic wall temperature, r is the recovery factor, u is the velocity, and C_p is the specific heat at constant pressure. This equation is only valid for an adiabatic wall. The recovery factor of 0.89 will be used when the used number is not specified. 0.89 is the Prandtl number for air at room temperature. The specific heat C_p of air is 1004 $j/kg/K$. With the known velocity distribution from PIV the temperature distribution can be calculated. To compute the density the perfect gas law is employed:

$$\rho = \frac{P}{RT}$$

For density computations the assumption is made that the pressure is constant though the boundary layer. This assumption is valid in the case that there are no strong shocks running through the domain. In figure 4.22 a profile is taken from the CFD information of the L48R25 geometry. Three lines are shown, the density taken from the CFD, the density calculated with the above mentioned approach (Crocco-Constant pressure) and the density calculated with the above mentioned approach, with the difference that the pressure is not taken constant, but varies according with the information from the CFD (Crocco-CFD pressure).

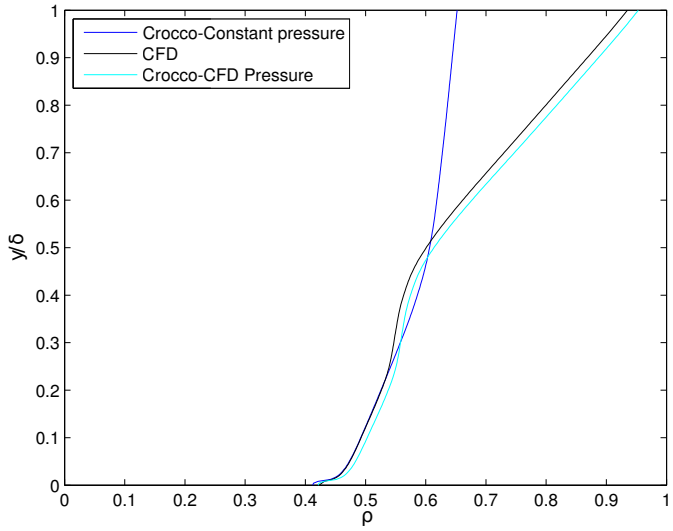

Figure 4.22: Density L48R25, at $\frac{x}{L_t} = 0.75$

Figure 4.22 shows a profile which is disturbed by shocks. It can be seen that the density taken from the CFD and the density computed with pressure taken from the CFD compare well. The density computed with a constant pressure does show significant deviations. This figure shows the importance of validating the influence of shocks on a profile before density calculations are done with a constant pressure assumption.

For the determination of the boundary layer thickness and velocity, the definition of δ_{99} is taken. This means that the boundary layer thickness is defined as the distance perpendicular to the surface were the velocity reaches 99% of the mean flow velocity. As will be shown later, shock waves make that a number of velocity profiles show large oscillation. When a velocity profile shows oscillation, the first maxima is is taken as the mean flow velocity, taking care that this maximum is representative, and lies close to the free stream velocity. In this report the compressible displacement thickness and momentum thickness are used:

$$\theta = \int_0^\infty \frac{\rho u}{\rho_0 u_0} \left(1 - \frac{u}{u_0}\right) dy$$

$$\delta^\star = \int_0^\infty \left(1 - \frac{\rho u}{\rho_0 u_0}\right) dy$$

In the case these quantities are calculated with PIV data, care has been taken to ensure that the assumption of constant pressure can be used. For the calculation of the friction velocity a fit is done to the log-law part of the boundary layer. After a van Driest transformation

[12], a linear fit was done to the log-law region of the boundary layer. In this fitting procedure the friction velocity could be determined since the value of the van Karman constant κ was set constant at 0.41.

Chapter 5

Validation

The acquired solution with CFD may differ from reality for a number reasons. CFD is a model of reality, describing it in a set of partial differential equations. Errors can occur in the physical modeling of the phenomenon, and the the discretization of the equations. In the previous section it was shown that the discretization error is small by means of a grid convergence study. In the current chapter the computational results will be validated by means of the experimental results.
The validation will be done in multiple parts. First it will be shown that inflow conditions show expected behavior. PIV and CFD will be compared against each other, and against analytical results. The next section will show that all the results from CFD, Schlieren and PIV are similar. The results from all 3 techniques will be compared to show that they produce the same flow features. Velocity distribution at a number of places will be shown for 3 geometries, obtained using PIV and CFD. It will be shown that the CFD velocity distributions compare reasonably well with the PIV results. For the high frequency plates a mismatch between the CFD and PIV results will also be shown. In the last section the change in momentum thickness and displacement thickness over the plate will be compared between CFD and experiments.

5.1 Inflow

The current section will describe the inflow conditions in the test section. Four datasets will be used for the comparison. The experimental data for the entire tunnel geometry will be compared with the CFD solution with an SST turbulence model. The experimental data from Zoom 3 will be used. The CFD solution of half the tunnel with a BSL turbulence model, and with an SST model will also be compared. This allows for comparisons of the velocity profiles, Reynolds stresses, shear stresses and it allows for a quantification of the effects of the inserts on the flow. The velocity profiles have been taken at a location of $\frac{x}{L_t} = 0.03$. Figure 5.1 shows all the velocity profiles for the start of measurement section.

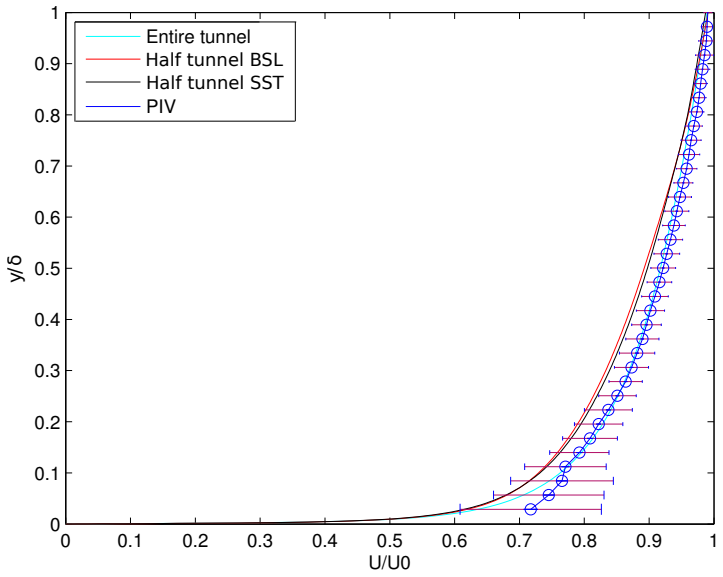

Figure 5.1: Velocity profiles start test section at $\frac{x}{L_t} = 0.03$

The four lines show the experimental results (dark blue), the entire tunnel simulation (light blue), and 2 simulations of the half domain (red for BSL model, and black for SST model). The error bars are based on the RMS of the velocity data. The height has been normalized by the boundary layer thickness, and the velocity has been normalized by the mean flow velocity. Both simulations of the half domain show great resemblance. The entire tunnel simulation shows great resemblance with the experimental results. As can be seen experimental data deviates from the CFD results near the wall (for y/δ <about 0.1). But for larger distances from the wall(for $y/\delta >\sim 0.1$) (3th data point) the resemblance with the entire domain simulation is good. It will be shown later that the mismatch between the experimental results and the entire domain simulation on the one hand, and the two half tunnel simulations on the other hand, is due to the fact that the entire tunnel simulation and the experimental results have not fully recovered from the shock at the start of the front insert. Situated downstream in the test section figure 5.15 shows a good

comparison between the computational and experimental results .

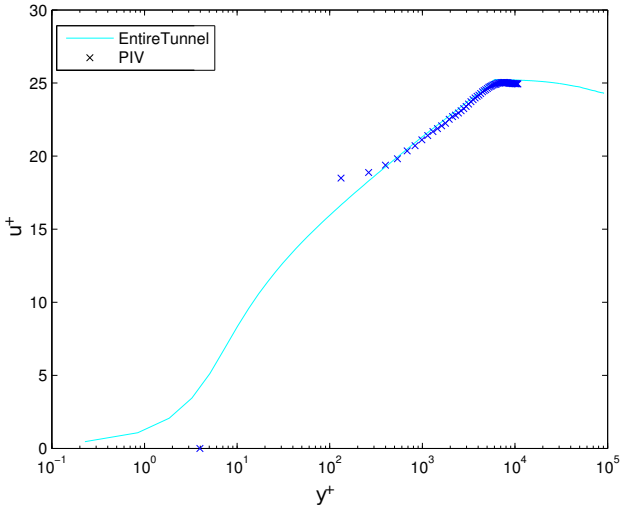

Figure 5.2: Velocity profiles start test section, log region

Figure 5.2 is a log plot of the velocity data of the PIV and Entire tunnel CFD from figure 5.1. The first PIV data point is at y^+ 132.6. Linear behavior of both data sets can be observed till y^+ in the order of 5000. This linear region can be studied in figure 5.3.

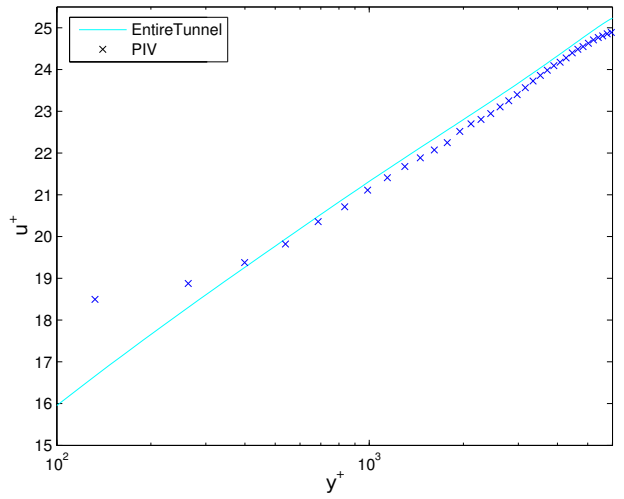

Figure 5.3: Velocity profiles start test section, zoom log region

Figure 5.3 shows the a zoom of the linear region of figure 5.2. Clear linear behavior can be seen.

The first three data points of the PIV close to wall show a deviation with respect to the

CFD. A explanation for this deviation could be the fact that the interrogation windows which are used to compute these data points overlap the wall. Hereby the average velocity in the windows is larger then the local velocity.

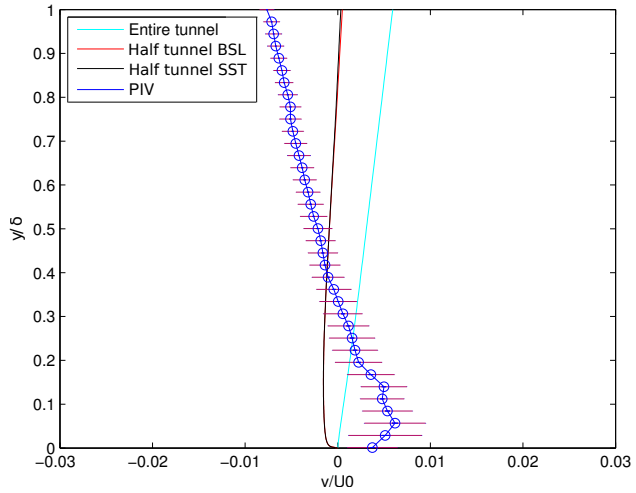

Figure 5.4: Velocity v start test section at $\frac{x}{L_t} = 0.03$

In figure 5.4 one can see the v velocity normalized by the mean flow velocity. Error bars are based on the RMS on the velocity. As can be seen the experimental results do not follow the same trend as the simulations. In the experimental results, and the entire tunnel simulation the air flow was flowing over a flat plate, the section where the flow could recover from the transition to the front insert. The half tunnel geometry is following the original nozzle contour of the wind tunnel, and is therefore still expanding. It can therefore be expected that the results differ. The entire tunnel simulation and the experimental results show different behavior. However the differences are small in comparison with the general behavior of the flow. Therefore we will conclude that inflow conditions are properly reproduced by the numerical approach.

In table 5.1 the free flow velocity and boundary layer thickness can be seen.

Table 5.1: Boundary layer thickness, and mean flow velocity

Case	Turbulence model	$\delta \quad (mm)$	$U_0 \quad (m/s)$
Entire tunnel Geometry	SST	5.37	517.9
Half tunnel geometry	SST	6.14	516.0
Half tunnel geometry	BSL	6.34	515.9
PIV results	-	5.46	511.9

In table 5.1 the boundary layer thickness δ, and mean flow velocities U_0 are displayed. What can be observed is that both half geometry simulations are closely related in their boundary layer thickness and mean flow velocity. The boundary layer thickness of the full geometry and PIV measurements are within 0.1 mm of each other. The difference in the mean flow velocities between the Entire tunnel simulation and the PIV simulation are due to difference in total temperature of the flow. The total temperature for the CFD was set at 290 Kelvin, while the total temperature while the total temperature of the flow is 283 Kelvin is for the zoom 3 measurements. According to calculations the difference in mean flow should be 4 m/s. With this correction in place the difference between the experimental results and the Entire tunnel simulation amounts to 2 m/s.

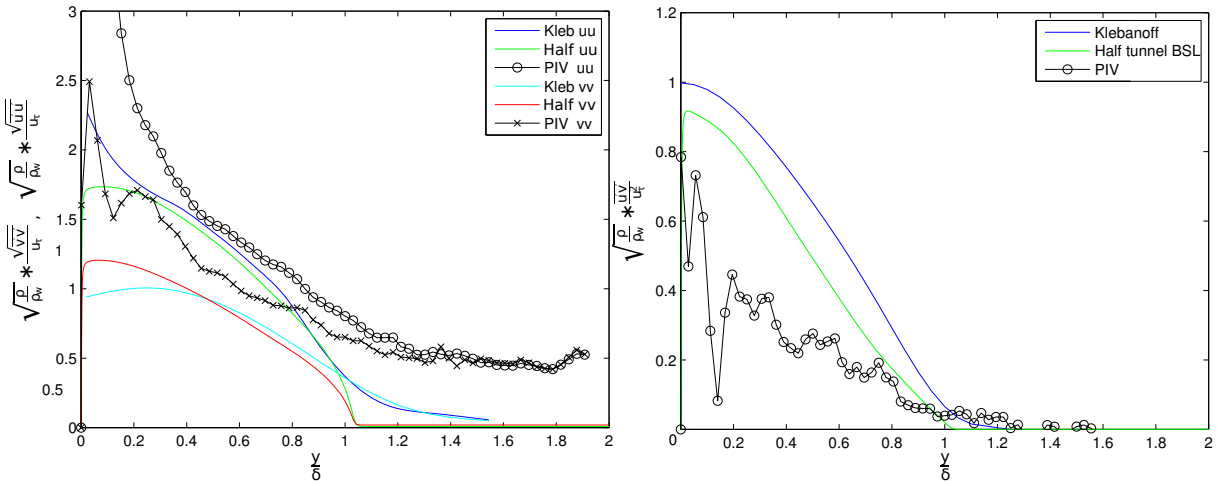

Figure 5.5: $\overline{u'u'}$,$\overline{v'v'}$ (left), $\overline{u'v'}$ (right) Reynolds stresses at $\frac{x}{L_t} = 0.03$

In figure 5.5 the Reynolds stresses $\overline{u'u'}$, $\overline{v'v'}$ and $\overline{u'v'}$ are shown. The data has been averaged over a range of 20.85 mm in the x direction, $\frac{x}{L_t} = 0.03$ to $\frac{x}{L_t} = 10.4$. The CFD data concerns the half tunnel geometry with the BSL Reynolds stress model. Klebanoff stresses[31] have also been incorporated for a comparison to a standard boundary layer. As can be seen from the $\overline{u'u'}$ and the $\overline{v'v'}$ Reynolds stresses the free stream stresses are higher than a standard boundary layer. These stresses are also high at the wall. A number of PIV images show a low level of seeding at the wall, and therefore a decrease in measurement quality at the wall, which could be the cause for these high stresses. The $\overline{u'v'}$ stresses show a lower value over the entire boundary layer. The PIV measurements in figure **??** still show large fluctuations after averaging, indicating that there are large fluctuations in the measured values. Therefore the Reynolds stresses do not have enough quality to be used in later processing.

To make a temperature comparison between the experimental and numerical results, temperature data needs to be derived from the PIV results. For this a Crocco-Bussemann

relations for $T_w = T_{w_{ad}}$ can be used, see section 4.7. See figure 5.6 for the temperature distribution, normalized with the total flow temperature.

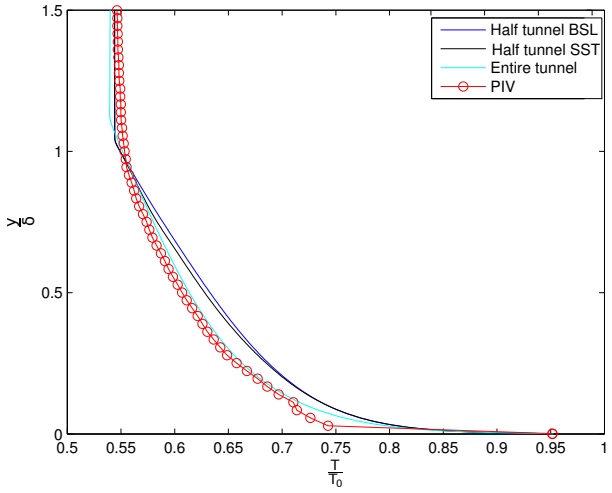

Figure 5.6: Temperature profiles at $\frac{x}{L_t} = 0.03$

What can be seen is that there is a small discrepancy between the static flow temperatures of all the cases. These differences are due to small differences between the cases. The CFD has a different total temperature then PIV. Also there is a small difference in Mach number between the half and whole cases due to the insert which has been places in the nozzle. In figure 5.7 the pressure profile can be seen, where the pressure has been normalized by the total pressure.

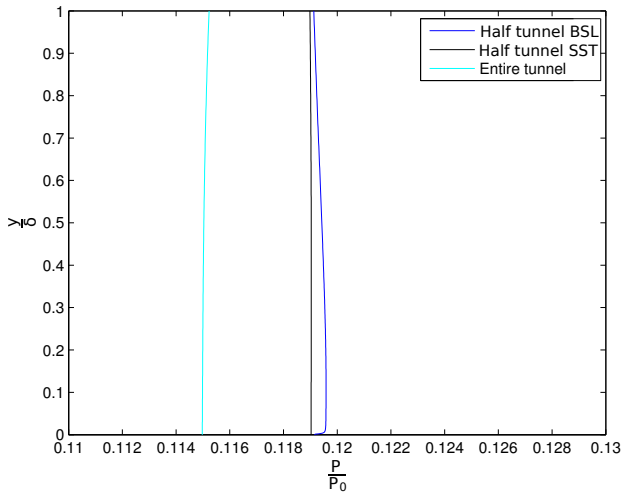

Figure 5.7: Pressure profile at $\frac{x}{L_t} = 0.03$

It can be observed from figure 5.7 that there is a difference between the half, and whole tunnel results. It can be seen that there is a small pressure gradient in the solution from the BSL model. The major gradient is between $4 < y^+ < 50$. For larger y^+ values a small pressure gradient can be observed. This authors expects the cause to be the implementation of the coupling between the wall turbulence model, and the free stream turbulence model.

As will be shown in section 5.3 the flow is still developing for the PIV and Entire tunnel CFD case. Therefore no steady state pressure profile has set in, which is the main reason for the differences between the half tunnel and Entire tunnel CFD. At $\frac{x}{L_t} = 0.5$ there is a good match in the pressure profile.

The last comparison on the inlet will be done on the friction coefficient. For the simulations the friction coefficient can be obtained directly from the numerical results. For the experimental data, a fit to the law of the wall has been made to obtain the friction velocity see section 4.7 for details. In combination with the estimated temperature field, and the assumption of constant pressure, the friction can be calculated.

Two models have also been taken as extra comparison. The models are those from Fernholz [16] and Cousteix [20]. The Cousteix model can be seen in equation (5.1)

$$C_f = \frac{0.0172}{Re_\theta^{0.2}} f^{6/5} \qquad f\left(M_e\right) = \frac{C_f}{C_{f_i}} \tag{5.1}$$

Where C_f is the friction coefficient, Re_θ the Reynolds number based on the momentum thickness and the subscript i stands for incompressible. The fraction of friction coefficients is presented in graphical form by Cousteix, see [20]. The Fernholz model can be seen in equation 5.2.

$$C_f = 2\frac{\rho_w}{\rho_e}\left\{\frac{U_e^* - U_1^*}{U_e}\left[\left(\frac{1}{k} - M\right) ln\left(\frac{y}{\Delta^*}\right)_p - N - \frac{1}{k} ln\left(\frac{y_1}{\Delta^*}\right)\right]^{-1}\right\}^2 \tag{5.2}$$

Where:

$$M = 4.70,\ N = 6.74\ for:\ 1.5x10^3 \leq Re_{\theta_w} \leq 10^5$$

$$ln\left(\frac{y}{\Delta^*}\right)_p = 2.70\ for:\ Re_{\theta_w} \geq 2x10^3$$

$$\frac{1}{k} ln\left(\frac{y_1}{\Delta^*}\right) = -2.67 - ln\left(Re_{\theta_w}\right)$$

$$\frac{U_1}{u_e} = 0.6 + 0.023 M_e\ for:\ Re_{\theta_w} \geq 2x10^3\ and:\ M_e \leq 4.5$$

$$\frac{U^*}{U_e} = \phi^{-\frac{1}{2}} sin^{-1}\left(\frac{2\phi\frac{U}{U_e} - \psi}{\psi^2 + 4\phi^{\frac{1}{2}}}\right)$$

With:

$$\phi = r\frac{T_e}{T_w}\frac{\gamma - 1}{2} M_e^2$$

$$\psi = \frac{T_{aw} - T_w}{T_w} = 0$$

Employing all these models, including a Re_θ value of 13350 the following values for the friction coefficient were obtained:

Table 5.2: Friction coefficients

Data set	$C_f \times 10^{-3}\,(-)$
Half SST	1.66
Half BSL	1.66
Entire tunnel	1.70
PIV	1.88
Cousteix	1.85
Fernholz	2.01

Data set	$u_\tau\ (m/s)$
Half SST	19.31
Half BSL	19.3
Entire tunnel	20.52
PIV	20.38

In table 5.2 all the friction coefficients and friction velocities can be seen. The friction velocity has been obtained by fitting the velocity profile to the law of the wall with standard coefficients. Friction coefficients were obtained from the measured friction velocity, in combination with wall density. For the experimental results, a Croco-busemann relation was used in conjunction with a assumption on constant pressure to calculate the density. From table 5.2 it can be observed that both the half tunnel value compare well. The estimations from Fernholz and Cousteix are in agreement with the experimental results. There are differences between the PIV and CFD results. The differences occur due to differences between in the friction velocity, and due to differences in the flow density. As

can be seen the friction velocity differs between half geometries, Entire tunnel and PIV. Differences between the Entire tunnel and PIV are small. The difference between the half tunnel and Entire tunnel are due to the differences in velocity profile as shown in figure 5.1. The differences in calculated friction coefficient between the PIV and the Entire tunnel PIV are due to uncertainties in the wall pressure. The wall pressure used to calculate the density for the PIV is the mean flow static pressure. For the entire tunnel CFD the numerical pressure data was used. When computing the friction coefficient for the PIV data with the wall pressure obtained from the entire tunnel CFD it is $1.75e-3$, which agrees well with the numerical result.

5.2 Comparison of multiple experiments

Three PIV measurements with a large field of view where made. The goal of these measurements was to validate that the PIV set up and to serve as comparison between all undertaken measurements: CFD, Schlieren and PIV.
Measurements where taken of the flat plate, L48R25 and L06R17 geometries to have a wide range of flow characteristics. Comparisons where done on velocity distributions, flow angles, and density gradients. Measurements where taken in the set-up as described in chapter 4. The PIV cameras where set-up with an overlap of 3.4 cm in the images to make sure that the whole field is visible.

It will be shown by all the results that there is a good agreement between all measurements, and therefore in the rest of this report it can be assumed that all the three datasets display the same flow behavior.

5.2.1 Velocity fields

5.2.1.1 Velocity distribution For the measured cases there is PIV data and CFD available. As has been described in chapter 4 the PIV data does not reach to the wall of the roughness elements since the laser sheet cannot reach to this position. The experimental velocity distributions in all the cases are compared with there CFD counterpart on a line at $\frac{y}{\delta} = 0.76$ above the surface.

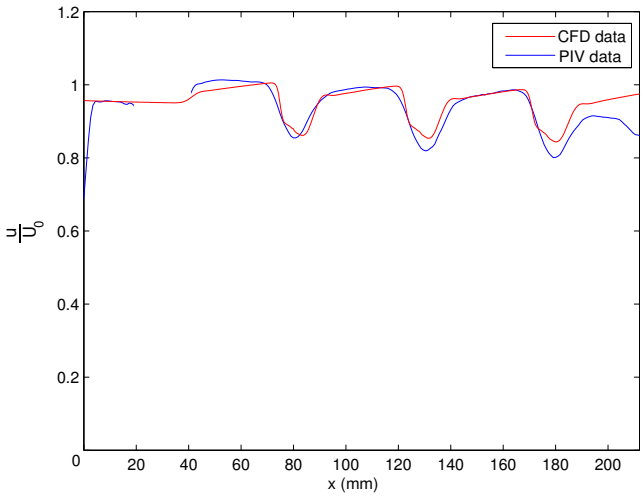

Figure 5.8: L48R25 Velocity distribution at $\frac{y}{\delta} = 0.76$

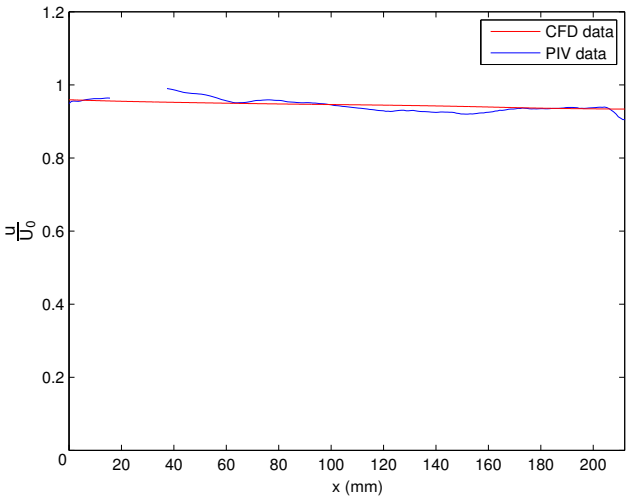

Figure 5.9: Flat plate velocity distribution at $\frac{y}{\delta} = 0.76$

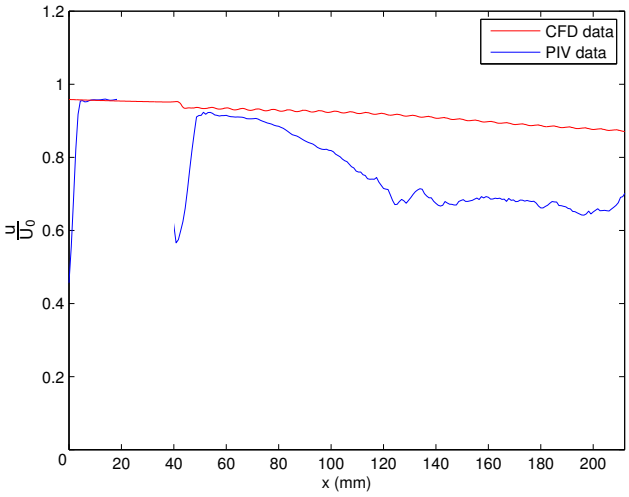

Figure 5.10: L06R17 Velocity distribution at $\frac{y}{\delta} = 0.76$

Figures 5.8-5.10 show the velocity distributions at a line of constant height.

The velocity is normalized with the free stream velocity, the x axis shows the running coordinate through the test section, x. The front insert ranges to 25 mm, after which the flow transitions to the plate. From 0 to 25 mm the wall is flat, and after 25 mm the flow sees a rough surface. At this transition point a big drop in the velocity can be seen. At this position there are reflections in the PIV images, which means that the data quality at this position is poor. As can be seen for the L48R25 case (figure 5.8) there is good agreement between the CFD and PIV results. The velocity variations across the shock match quite well. For the flat case (figure 5.9) there is a non-smooth transition between

the insert and the plate, it can be seen that after the reflection the PIV shows a larger velocity then the CFD. This corresponds to an expansion wave which is created by this non-smooth transition. Apart from these flow features the comparison between the two curves is good. For the L06R17 case (figure 5.10) it can be seen that the experimental data shows a stronger decrease of the velocity than the numerical results show. A possible reason for this mismatch is that these elements produce such levels of turbulence that the turbulence model cannot handle this properly. The turbulence model sets a limit on the turbulence production in order to avoid false turbulence by limitations in the numerical procedures.

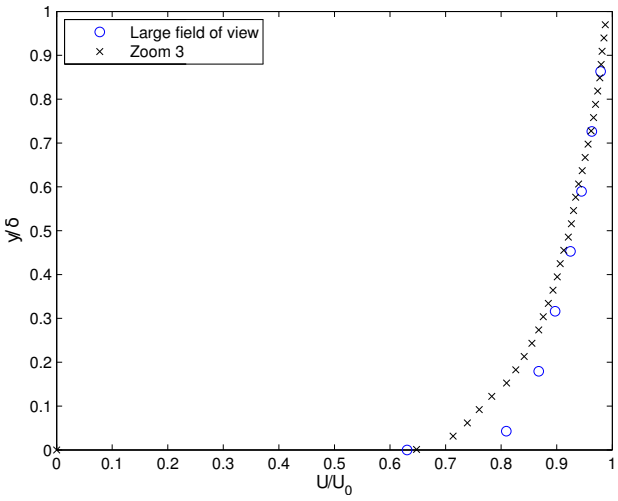

Figure 5.11: Self consistency PIV measurements, at $\frac{x}{L_t} = 0.05$

Figure 5.11 shows a velocity profile of the large field of view, and zoom 3 PIV data. It can be seen that the increase in zoom yields a significant decrease in vector pitch. The first 3 measurements show a discrepancy with the Zoom 3 data, after which both datasets match well. The first vectors for the large field of of view case overlap the wall, which makes that these vectors are an overestimation of the actual velocity.

For the L48R25 case the flow angles have been calculated to show the variation over the shocks. In figure 5.12 one can see the flow angles and line where the velocity data has been extracted. The flow angle has been calculated according to $atan\left(\frac{v}{u}\right)$.

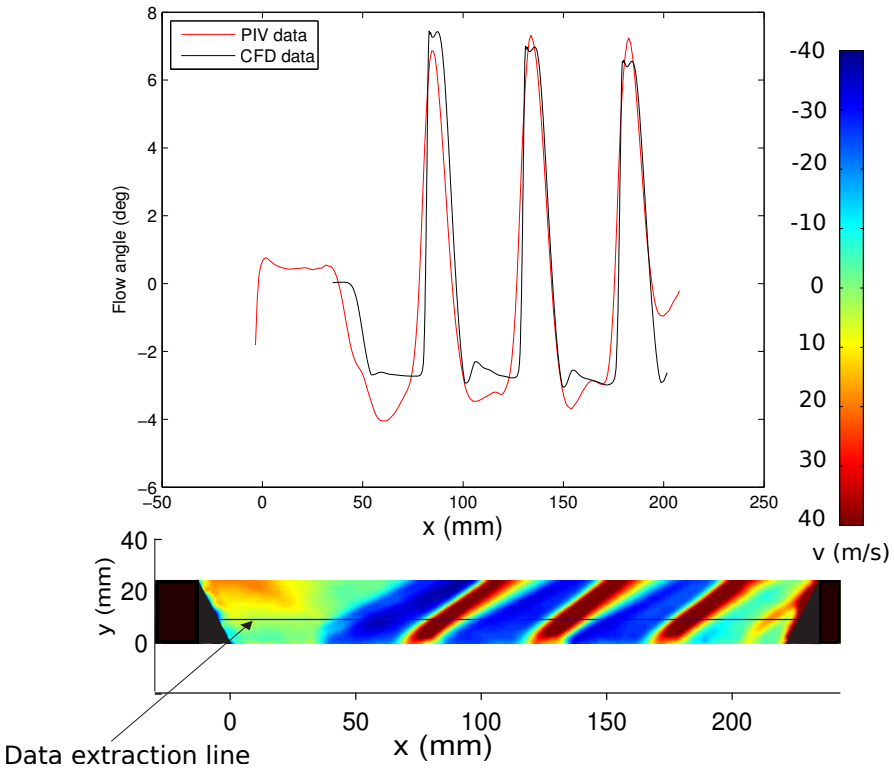

Figure 5.12: Flow angle, Velocity distribution L48R25 geometry

In figure 5.12 on the top the flow angles can be seen. On the bottom of the figure the distribution of the v velocity can be seen. On the contour plot of the v velocity, from the experiments the line which has been used to extract the velocity data can be seen. This is is at a constant $\frac{y}{\delta}$ of 1.37. It can be observed that there is a small discrepancy between the maxima and minima of the PIV and the CFD. PIV has difficulty measuring the velocity over a shock since the particles are not imaged as points due to optical aberrations.

5.2.2 CFD-Schlieren

For comparison between the CFD and the Schlieren measurements a CFD figure was generated of the density gradient in the y direction for the the L48R25 case. This figure overlapped with the same Schlieren figure to observe the similarities,

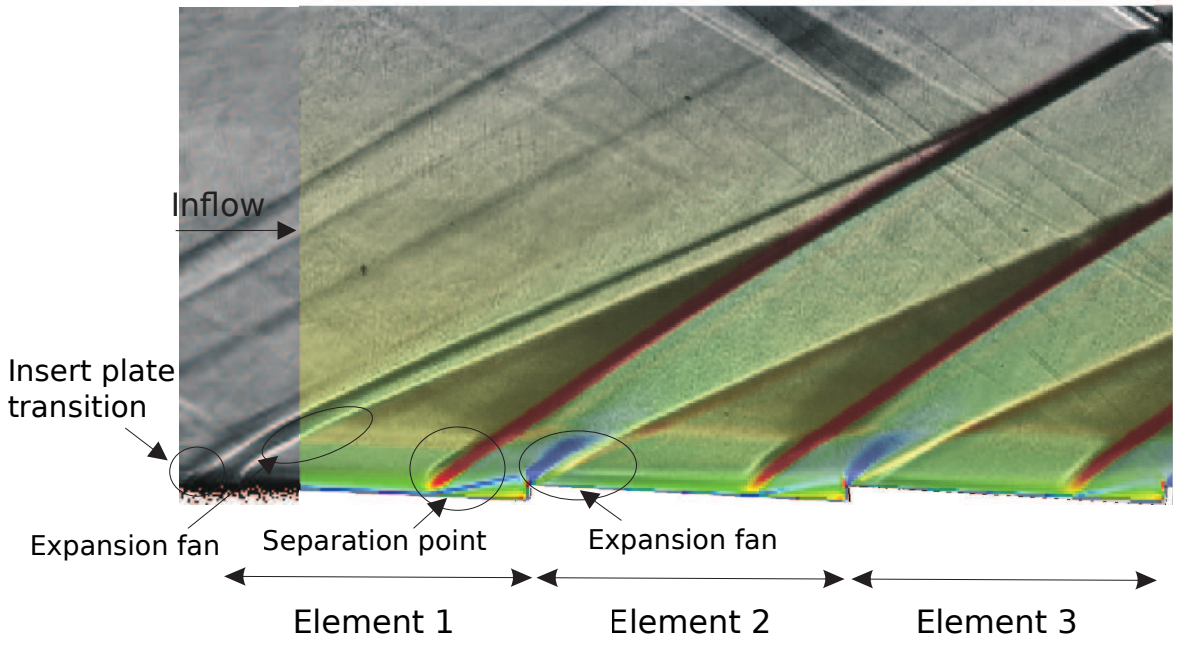

Figure 5.13: CFD-schlieren overlap L48R25 geometry

The Schlieren is shown as the black and white features, while the CFD is shown in color. The flow is from left to right in the image.
As can be seen on the left side of the image there is an initial expansion from the front insert to the plate. After this there in an expansion into the first element. Here it can be observed that the regions overlap quite well. The shock position is well predicted by the CFD, the initial shock shape although deviates from the predicted CFD shapes. The results for the expansion fan between the PIV and the Schlieren also match well.

5.3 Velocity cut-outs

As was shown in the previous sections, there is good agreement at the inflow plane, and on the general flow features. In this section it will be shown that the agreement between the CFD and the experiments also holds for general locations. At a number of locations there are also discrepancies. A number of velocity cut-outs will be presented for the flat plate, L48R25, L06R03 and L10R17 cases to give confidence in the numerical results. As will be shown in chapter 7 the L06R03 profile shows different characteristics then the L48R25 geometry. Therefore it has been added to this section to show how the numerical results compare to the experimental results. The L10R17 geometry is shown in this section instead of the L06R17 geometry, which was shown in the last section, to shows that both high frequency geometries tested show significant deviations with respect to the experimental results. A profile will be shown from both fields of view, and a profile on the end of the roughness geometry. For the L48R25 geometry the profiles are chosen in attached flow regions, since these regions represent the majority of the flow field. For the L06R03 geometry a profile is chosen in an attached flow region, and in a region just in front of an separated flow region. For this profile the separated flow regions occupy a larger region of the geometry, and therefore the flow should be validated here. The L10R17 geometry is completely covered by separated flow, as will be shown, and therefore 2 locations have been chosen, at the start and in the middle of an element.

5.3.1 Flat plate

In section 5.1 a good comparison was found at the inflow between the numerical, and the experimental velocity results. Downstream of the inflow, in the second field of view the comparison is good as well.

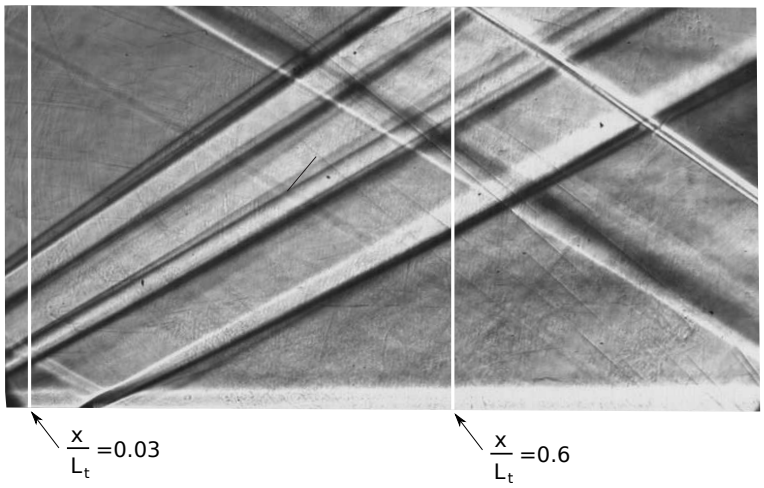

Figure 5.14: Locations profiles flat plate

Figure 5.14 shows the locations of the extracted velocity profiles. The location of the inflow profile is at $\frac{x}{L_t} = 0.03$, while the profile which can be seen in figure 5.15 is located at $\frac{x}{L_t} = 0.6$.

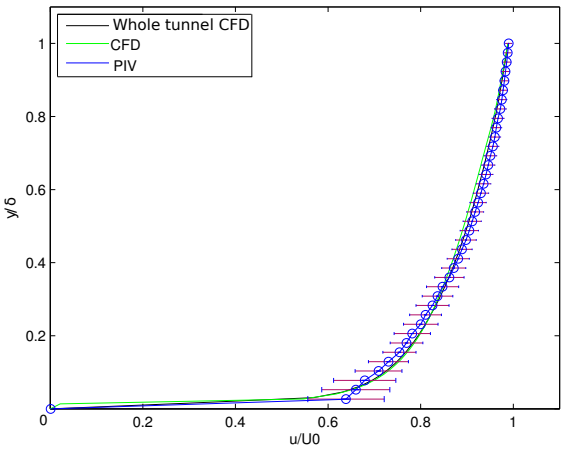

Figure 5.15: Flat velocity distribution at $\frac{x}{L_t} = 0.6$

In figure the 5.15 the comparison between the flat plate half simulation and the experimental data, and the whole tunnel simulation can be seen. Note that the comparison between entire tunnel CFD, the experimental and the numerical data has improved at this location with respect to the inflow. This suggests that the flow at the inflow did not recovered fully from the shock it endured when flowing over the tunnel insert.

5.3.2 L48R25

Figure 5.16 shows the positions were the profiles of the L48R25 profile have been extracted.

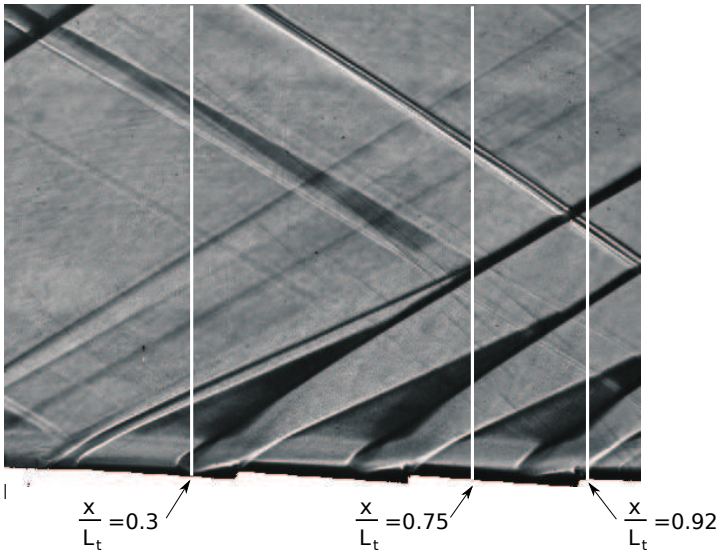

Figure 5.16: Locations profiles L48R25

In figure 5.17 one can see a velocity distribution at an x location of $\frac{x}{L_t} = 0.3$ in the test section.

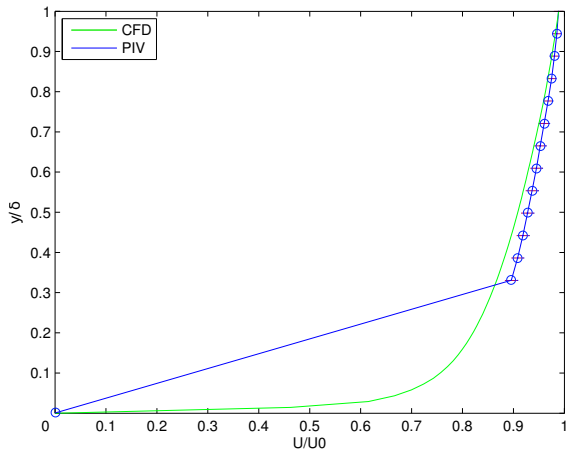

Figure 5.17: L48R25 at $\frac{x}{L_t} = 0.3$

Figure 5.17 shows the velocity distribution in the middle of the first roughness element. Comparison between the two distributions is reasonable, but for a part of the CFD data points are outside the error bounds on the PIV data. As was seen in the section on inflow the experimental velocity results showed more convex behavior then the numerical results. What can be seen here is a remnant of the difference at the inflow.

The reader must note here that this profile occurs at $0.3L_t$ before the profile shown in figure 5.15, also this profile has been through an expansion wave. Therefore one cannot expect the same similarity between the experimental and numerical results, as in the previous case. When going from one element to to a new element one would expect a better comparison between both, since the shock that accompanies the transition destroys the boundary layer and start development of a new one, See results chapter 7. In figure 5.18 the distribution can be seen at $\frac{x}{L_t} = 0.75$.

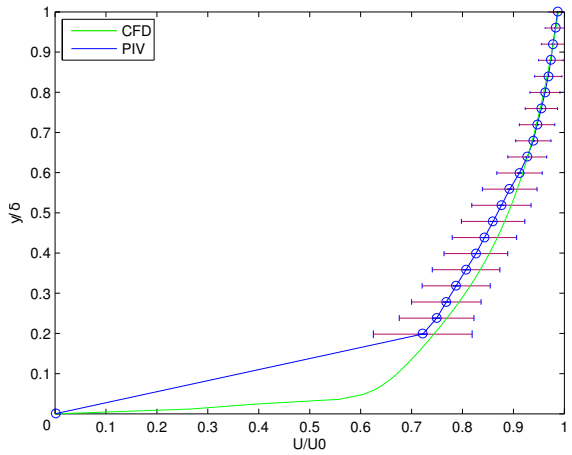

Figure 5.18: L48R25 at $\frac{x}{L_t} = 0.75$

What can be observed from figure 5.18 is that the comparison for this location is now better. Velocities are well within error bounds, and from 0.6 δ the averages compare quite well. This location is in the middle of the roughness element, which occurs after the profile from figure 5.17. In figure 5.19 the velocity profile of the L48R25 geometry can be seen after it has passed the roughness elements

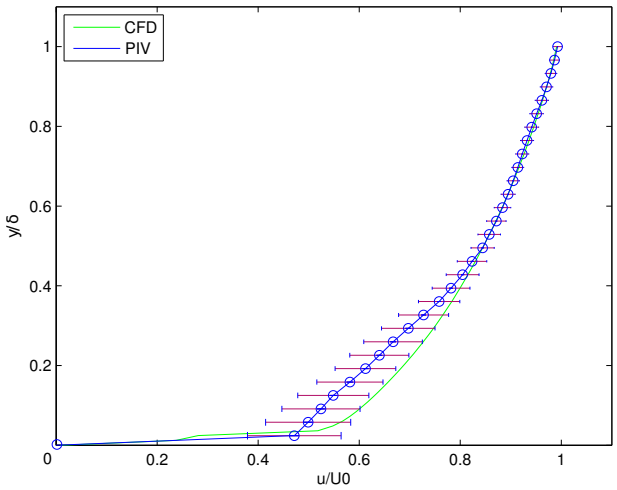

Figure 5.19: L48R25 at $\frac{x}{L_t} = 0.92$

The experimental results show a lower velocity in the lowest part of the boundary layer in comparison with the numerical results.

5.3.3 L06R03

The L06R03 geometry is the smallest geometry that has been tested both the CFD and PIV.

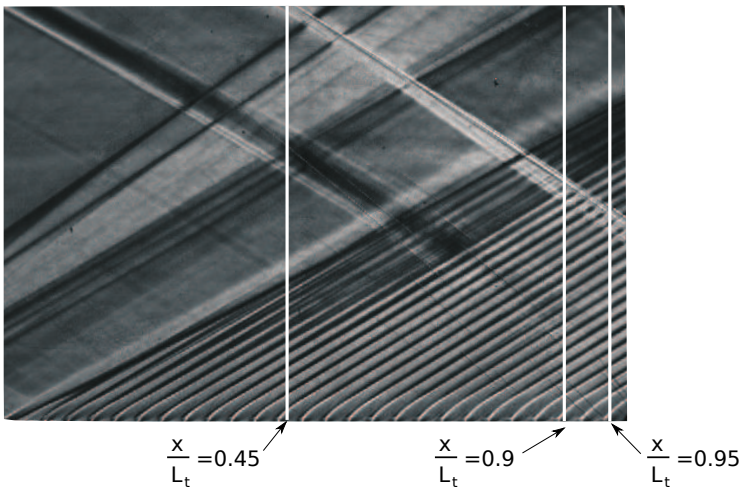

Figure 5.20: Locations profiles L06R03

Figure 5.20 shows a schlieren image of the flow over the L06R03 geometry, and all the locations on which velocity profiles are compared.

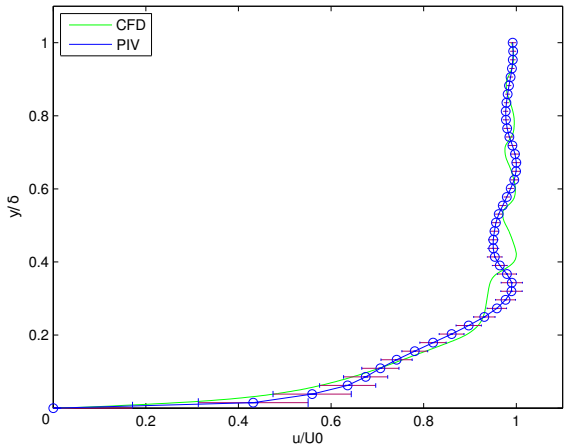

Figure 5.21: L06R03 at $\frac{x}{L_t} = 0.45$

Figure 5.21 shows a comparison of the PIV and CFD velocity profiles at $\frac{x}{L_t} = 0.45$. This location is at the start of an element. A piece of mean flow has also been plotted here. The mean flow varies and therefore the velocity also varies around the 99% free flow velocity.

At $\frac{y}{\delta}$ of 0.4 a mismatch between the data can be seen. CFD predicts this expansion wave higher than the experimental results. Apart from this a good comparison is found between the 2 data sets.

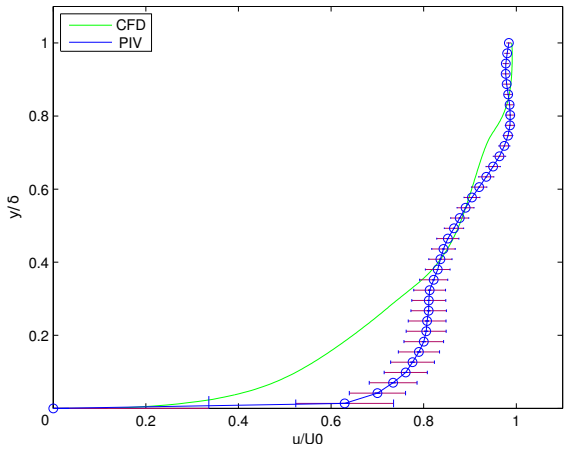

Figure 5.22: L06R03 at at $\frac{x}{L_t} = 0.9$

Figure 5.22 shows the comparison of the PIV and CFD at an $\frac{x}{L_t} = 0.9$. Here the comparison is less good then in the previous figure. This profile is just before a step. Therefore the profile passes though a shock, and a part of a separation area. Therefore both the PIV and CFD can be expected to have discrepancies with respect to the actual flow behavior.

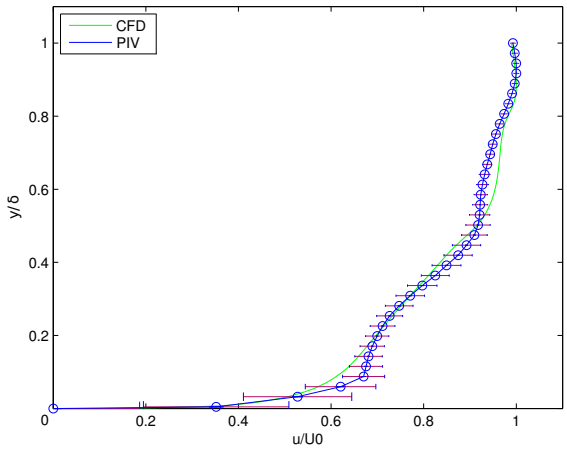

Figure 5.23: L06R03 at at $\frac{x}{L_t} = 0.95$

Figure 5.23 shows the velocity profile comparison at $\frac{x}{L_t} = 0.95$. Here all the roughness profiles have been passed and the flow is reasonably undisturbed. Both data sets correlate well with respect to the last figure.

5.3.4 L10R17

The L10R17 geometry will be discussed here in stead of the L06R17 geometry to show that both high frequency geometries show discrepancies with respect to the experimental results.

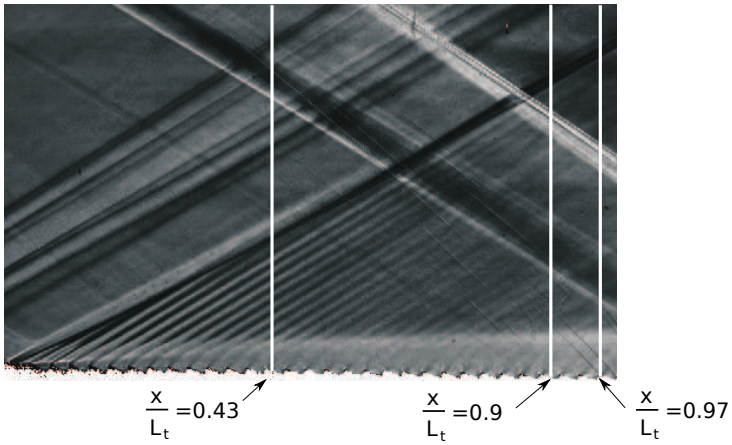

Figure 5.24: Locations profiles L06R17

Figure 5.24 shows the locations where the PIV and CFD have been compared on the L06R17 profile.

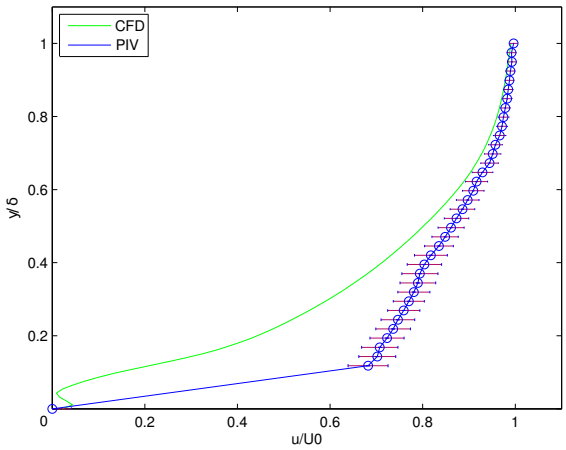

Figure 5.25: L10R17 at $\frac{x}{L_t} = 0.43$

In figure 5.25 one can see the velocity distribution at $\frac{x}{L_t} = 0.43$. The experimental and numerical results show a very different behavior. The location is in the middle of a roughness element.

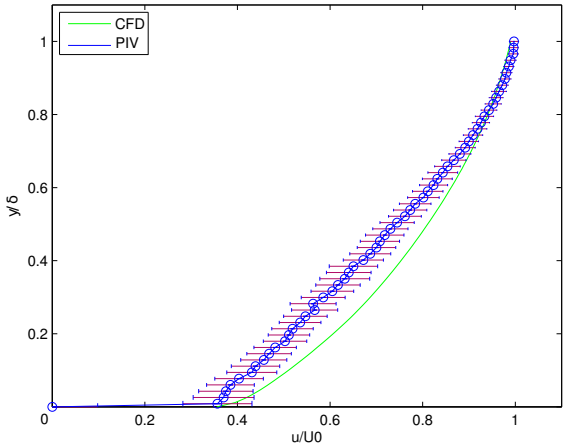

Figure 5.26: L10R17 at $\frac{x}{L_t} = 0.9$

Figure 5.26 displays the velocity distribution at $\frac{x}{L_t} = 0.9$. A match can be seen between the outer edges of the velocity distribution and the simulation. One can see that the velocity distributions show a deviation from CFD profile. The location of this profile, is in the beginning of a roughness element. Figure 5.27 shows a plot of the velocity profiles when the roughness elements have been passed. A good resemblance can be seen with the numerical results can be seen. In the middle of the boundary layer a deficit can be seen with respect to the numerical results.

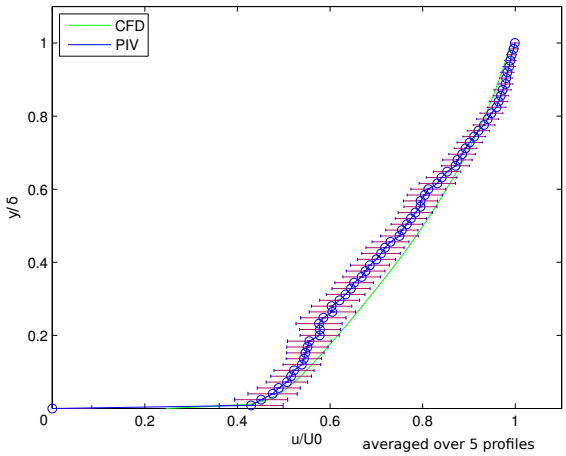

Figure 5.27: L10R17 at $\frac{x}{L_t} = 0.97$

5.4 Integral Boundary layer properties

In the previous section a number of velocity profiles have been presented. To broaden the evidence base as presented there, the integral boundary properties have been calculated. The integral boundary properties are the compressible momentum thickness, and displacement thickness, which are defined as:

$$\begin{aligned} \theta &= \int_0^\infty \frac{\rho u}{\rho_0 u_0}\left(1-\frac{u}{u_0}\right) dy \\ \delta^\star &= \int_0^\infty \left(1-\frac{\rho u}{\rho_0 u_0}\right) dy \end{aligned} \tag{5.3}$$

Equation 5.3 shows the definition of the momentum thickness θ, and the displacement thickness $\delta^\star$. As can be seen in the previous section the velocity profile can be disturbed due to shocks. Therefore this author defines the boundary layer as the first maxima as seen from the wall. In the case of a varying velocity profile care has been taken to insure that this maxima is representative for the flow field and that the free stream velocity lies close to the undisturbed free stream velocity. For the comparison between the CFD and the experiments this is not critical since the same procedure should be applied to both data sets.

To calculate the above mentioned properties from the CFD data two approaches were used, the density from the CFD calculation itself was used and the density was calculated by means of a Crocco-Busemann relation with the assumption of constant pressure, see section 4.7 for details. These two approaches are used since the density is also not knows a-priori for the PIV, were the density was also calculated with a Crocco-Busemann relation. Since two methods of density calculation are used the differences due to the calculation methods, and the differences due to the physics are be identified.

The boundary layer development over the plates should be the same. Therefore the development of the above mentioned boundary layer properties in the CFD should match with the experiments. The data has been taken at a point just after the roughness elements, to make sure that experimental results are available all the way to the wall. The ratio of these properties have been calculated between the inflow and outflow plane and they are shown in figures 5.28 and 5.29. Shows are the properties calculated from the PIV data, the properties calculated from the CFD data, with the density taken from the CFD (CFD density:CFD) and the properties calculated from the CFD data whereby the density was calculated with a Crocco-busemann relation.

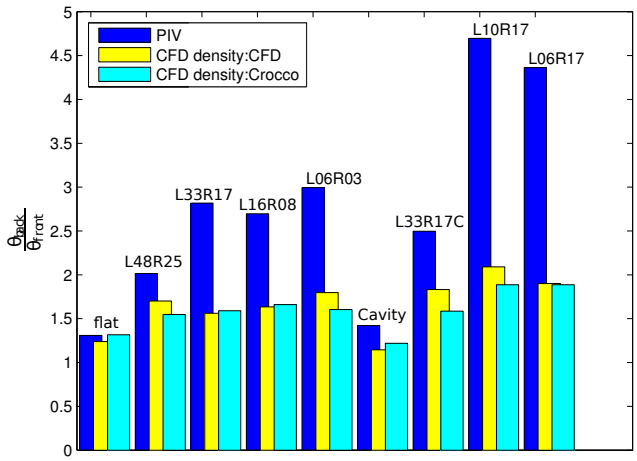

Figure 5.28: Momentum thickness development

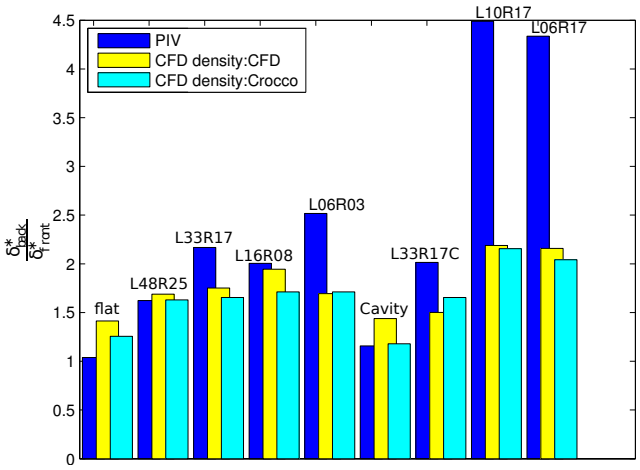

Figure 5.29: Displacement thickness development

In both figures it can be observed that all geometries except the L10R17 and L06R17 show reasonable agreement. Also both methods of density calculation for the CFD results show good agreement for all cases. For the L10R17 and L06R17 geometries the differences are significantly larger then the other geometries. In the velocity profiles, of the L10R17 geometry it could be observed that there is a significant mismatch between the experimental and numerical result.

5.5 Summary

From this chapter it can be seen that the inflow conditions show a not fully developed boundary layer profile. Comparison between the numerical and experimental results on the inflow conditions is good. The results for the flat and L48R25 case show a good resemblance with the numerical data at all tested locations. For the high frequency geometry it can be seen that there is a discrepancy between the numerical and experimental results. The experimental results can be seen lagging the numerical results. For the numerical results except the high frequency cases, the numerical solution is deemed in accordance with the experimental data, and will hereafter be used to derive results. The high frequency geometries results will also be used for results gathering, but it must be noted that the validation was not completely satisfactory.

Chapter 6

Flow description

In the current section the flow for each plate will be discussed. The schlieren images, PIV results and the the boundary layer details, derived from the CFD results will be shown for each case. For the original geometry no experimental data is available, and therefore the discussion on the flow topology will be based on the CFD results for this geometry. For the L48R25, L06R03 and L10R17 geometry single elements will be shown to discus the specific flow in the element. In this chapter the standard convention that the flow flows from left to right is upheld in all figures. In all figures where PIV results are displayed the Zoom level is shown, see chapter 4 for specifications. For a review of the shapes the reader is referred to chapter 3. Also shown are the distribution of the boundary layer thickness, shape factor and wall temperature. The boundary layer thickness and shape factor have been normalized by there values at the start of the test section. The wall temperature has been normalized by the theoretical flat plate adiabatic wall temperature of 275 Kelvin.

6.1 Flat plate

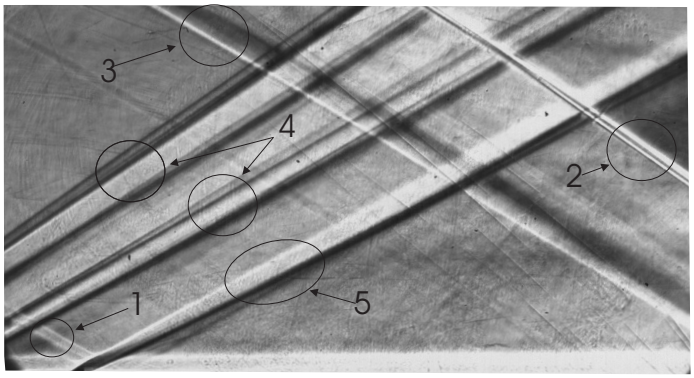

Figure 6.1: Flat plate Schlieren image

Figure 6.1 shows the Schlieren image of the flat plate. All of the flow structures that can be seen have been generated upstream. Number 1 is generated by a screw hole, just upstream of the nozzle. Number 2 is generated by the leading edge of the insert that has been inserted into the flow. Shock number 3 is generated by screw holes in the top nozzle block. Shocks 4 are the front and back part of the screw holes in the insert. Expansion wave number 5 is from the height difference between the front piece and the insert.

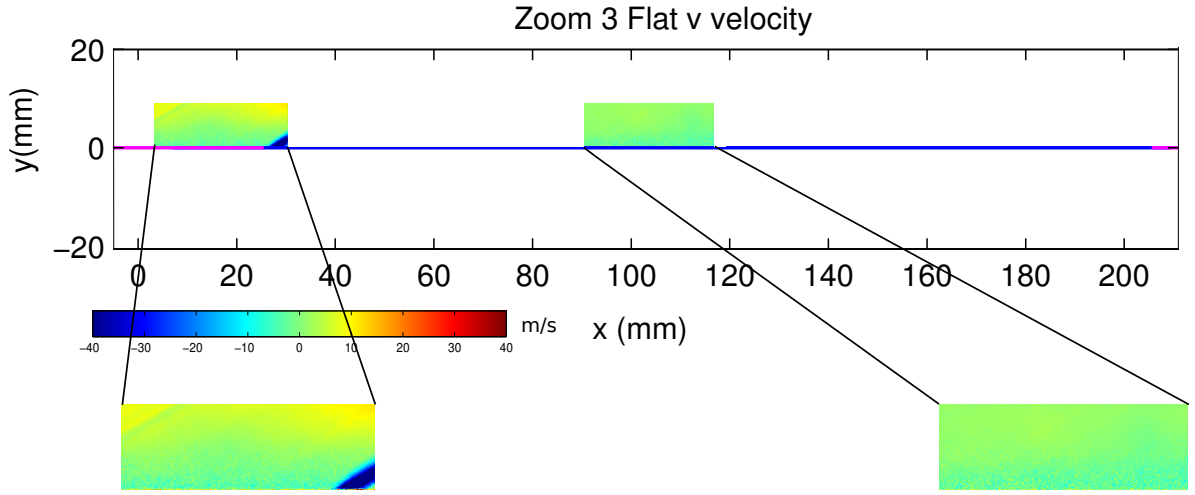

Figure 6.2: PIV results, Zoom 3, Flat plate v velocity

Figure 6.2 shows the experimental results for the v velocity. Due to the fact that this is a flat plate flow no noteworthy flow phenomenon can be seen except the transition from front insert to plate. Due to manufacturing difficulties no smooth transition was achieved

here. Therefore an expansion wave can be observed at the transition point, which occurs around 25 mm in x direction.

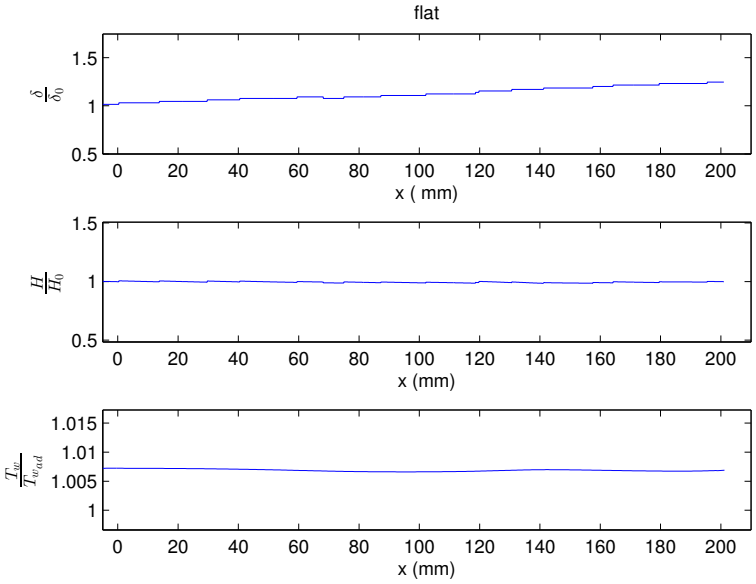

Figure 6.3: Flat plate wall and boundary layer properties

Figure 6.3 shows the results of the CFD calculations of the boundary layer thickness(upper panel),the shape factor(central panel), and the wall temperature (bottom panel) of the flat plate plate section. Due to in increase in Reynolds number the boundary thickness can be seen growing through the test section. The constant shape factor can be attributed to a stable boundary layer profile. Wall temperature remains constant, as can be seen. For a detailed explanation on the variation of the boundary layer thickness over a flat plate a textbook can be consulted, for example White [12].

6.2 L48R25

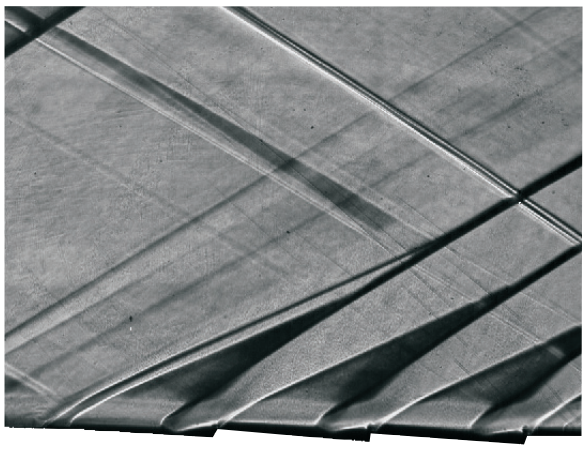

Figure 6.4: L48R25 Schlieren image

Figure 6.4 shows the Schlieren image of geometry L48R25. The disturbances in the flow show similar patterns as the flat plate picture, discussed previously. Noteworthy is here that the transition between the frontal part of the insert, and the plate is non-smooth. The first expansion wave that is visible, is the wave that originates at the transition from the frontal plate to the insert. The second expansion wave visible is the expansion into the first element. When approaching the step there is separation of the flow, and the formation of a shock, see figure 5.13 for a detailed description of the flow phenomenon. It can be observed that the boundary layer thickness has a minimum just after the shock. There is a recirculation region just after the shock, and in front of the step. The same flow topology can be seen in the next two elements. A growth of the boundary layer thickness can also be observed when moving over the elements.

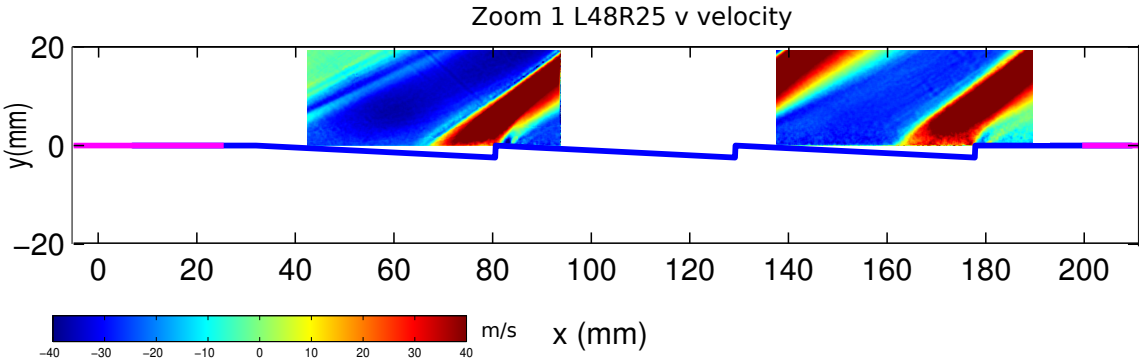

Figure 6.5: PIV results, Zoom 1, L48R25 v velocity

Figure 6.5 shows the PIV results for the L48R25 geometry. The figure displays the distribution of expansion waves, and shocks , which are caused by downward flow into the element, and the upward flow in front of the step.

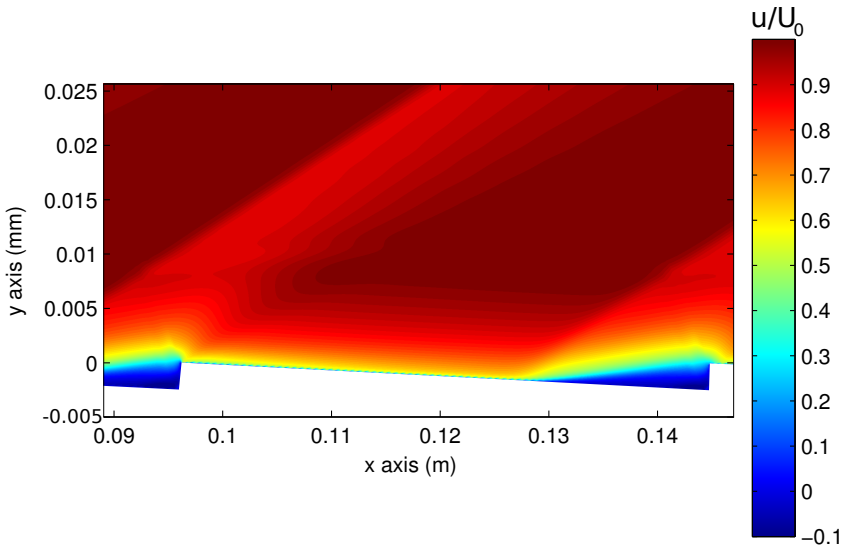

Figure 6.6: Zoom L48R25 element flow, u velocity

Figure 6.6 shows a zoom of the second to last element of the L48R25 geometry. An expansion fan can be seen which makes that the flow transitions onto the new element. A large section of flat flow is visible. At the separation point a shock and shear layer are visible. At this point a separation vortex is initiated in front of the roughness element.

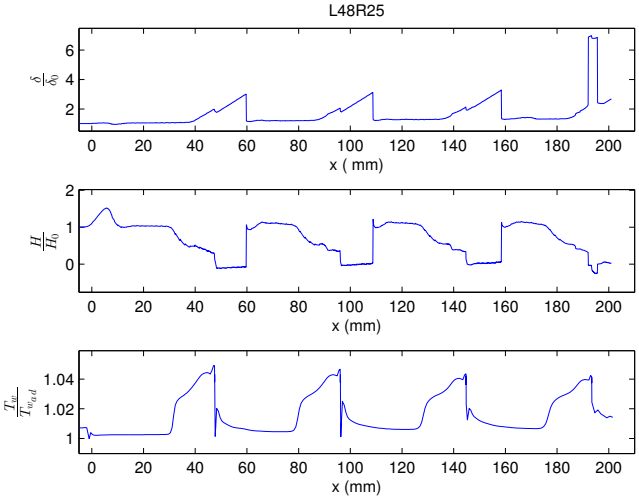

Figure 6.7: L48R25 geometry wall and boundary layer properties

Figure 6.7 shows the boundary layer thickness, shape factor and the wall temperature of the L48R25 geometry. The boundary layer thickness increases at the locations of the elements. The shape factor decreases in the roughness elements to a value of almost zero. Due to the separation of the flow, the air in the elements goes to an almost standstill, and therefore the temperature approaches the total temperature. In the boundary layer thickness a jump can be seen around x=190. At this point the flow will exit the last element. Here the flow will have to develop a new flat plate boundary layer, and it goes through an expansion fan. Therefore a large boundary layer thickness can be seen.

6.3 L33R17

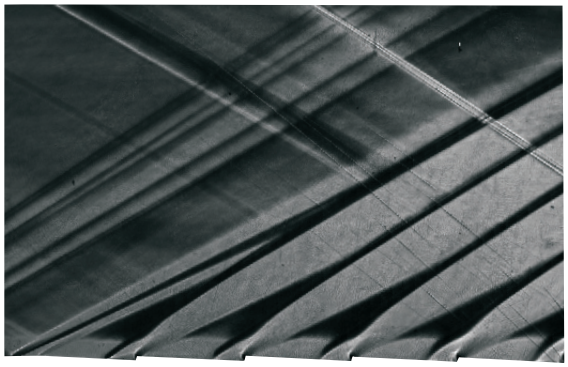

Figure 6.8: L33R17 Schlieren image

Figure 6.8 shows the Schlieren image of the L33R17 geometry. Again there is a non-smooth transition between the front insert to the plate. When the flow has reached the roughness elements the same series of expansion wave, shock wave, separated flow can be observed, equal to what can be seen in figure 6.4. Therefore it can be concluded that the overall flow topology is comparable to the L48R25 geometry.

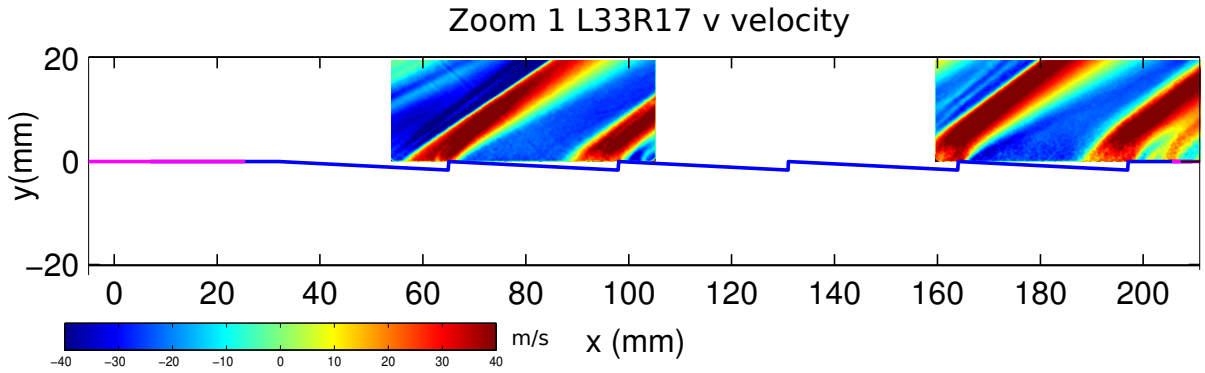

Figure 6.9: PIV results, Zoom 1, L33R17 v velocity

Figure 6.9 shows the v velocity of the L33R17 geometry. As can also be observed in the Schlieren image there are still distinct flow patterns emerging. The shock waves at the faces of the roughness elements are still clearly distinguishable.

6.4 L16R08

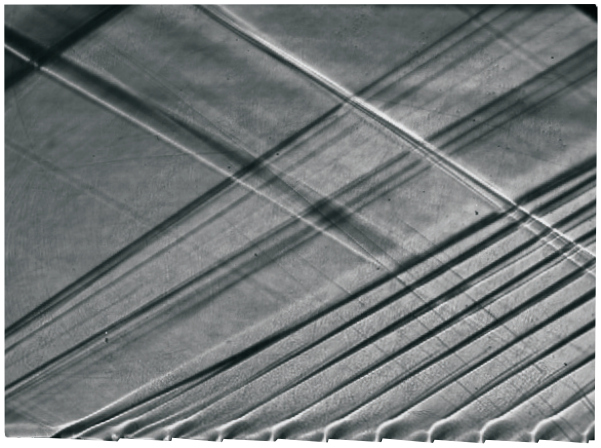

Figure 6.10: L16R08 Schlieren image

Figure 6.10 shows the Schlieren image of the L16R08 geometry. At the step positions individual flow features can still be seen. The size of the disturbances is decreasing with respect to the L33R17 geometry (figure 6.8)

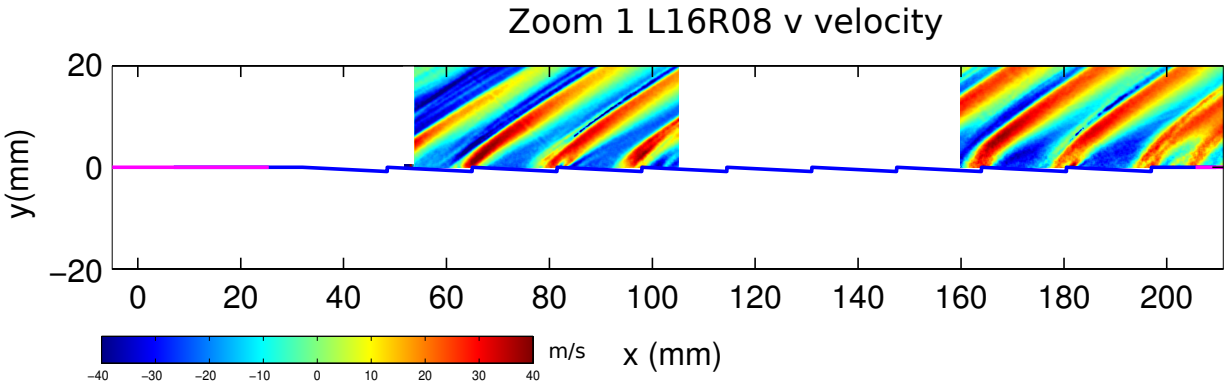

Figure 6.11: PIV results, Zoom 1, L16R08 v velocity

Figure 6.11 shows the v velocity if the L16R08 geometry. Noteworthy is that the strength of the shocks is decreasing with respect to the L33R17 geometry (figure 6.9).

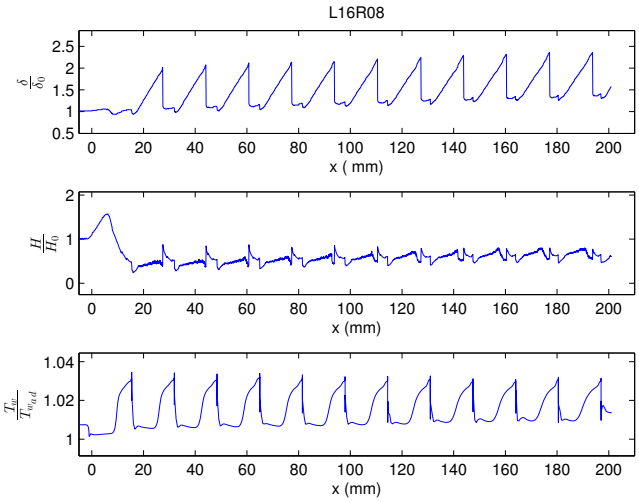

Figure 6.12: L16R08 geometry wall and boundary layer properties

Figure 6.12 shows the properties of the L16R08 geometry. An increase in boundary layer thickness and wall temperature is visible over the elements. The separation inside the elements is less then inside the L48R25 and L33R17 geometries, which can be seen because the shape factor does not change with the same magnitude as the previous cases.

6.5 L06R03

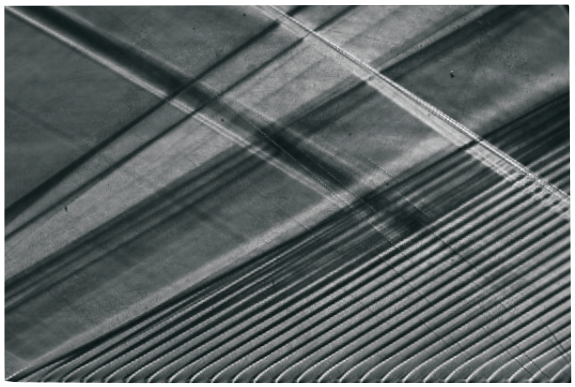

Figure 6.13: L06R03 Schlieren image

Figure 6.13 shows the Schlieren image of the L06R03 case. When one moved down the plate in stream wise direction it can be observed that the expansion waves coming out of the elements are still visible but the shocks become less visible. As will be shown in chapter 7 this is due to the deceleration of the flow. As will also be shown in chapter 7 a stable boundary layers forms on this geometry.

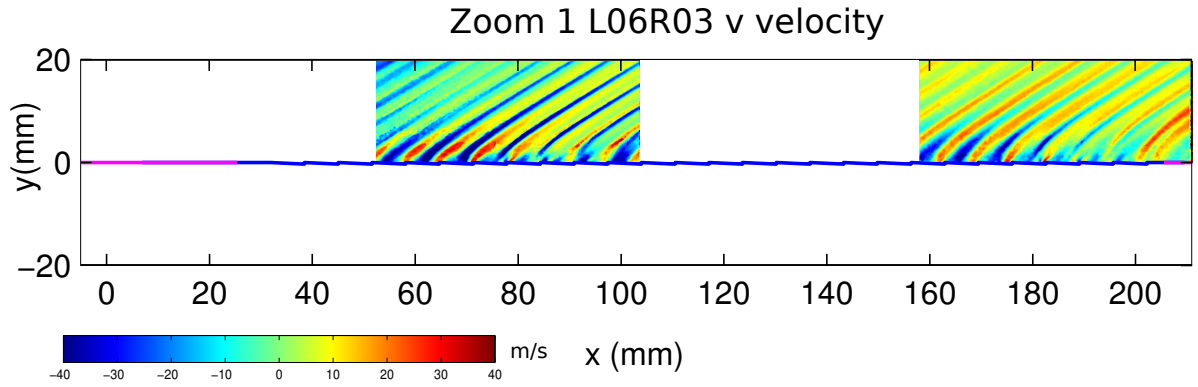

Figure 6.14: PIV results, Zoom 1, L06R03 v velocity

Figure 6.14 shows the v velocity of the L06R03 geometry. A decrease in shock strength is visible with respect to the L16R08 geometry (figure 6.11).

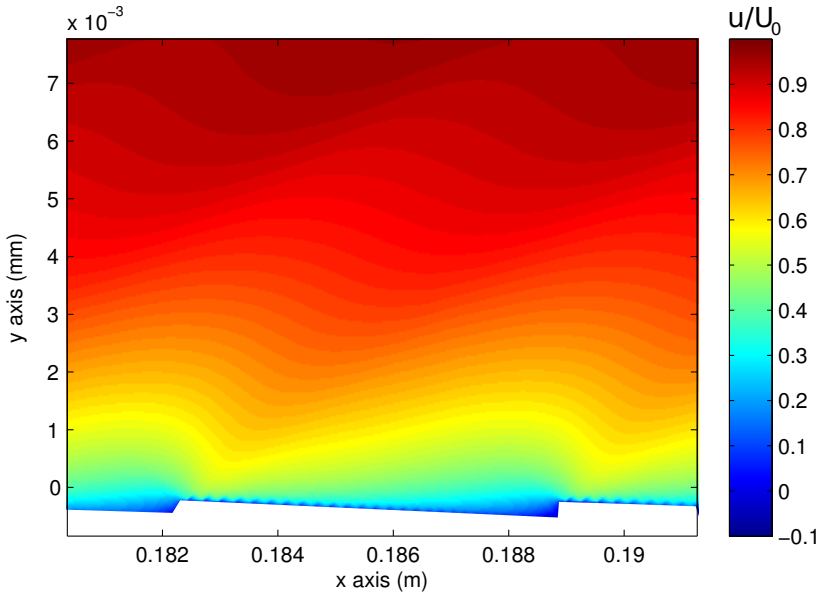

Figure 6.15: Zoom L06R03 element flow, u velocity

Figure 6.15 shows zoom of the second to last element of the L06R03 geometry. When compared to to the L48R25 a smaller separation size can be seen. Also no dominant flow phenomenon can be observed.

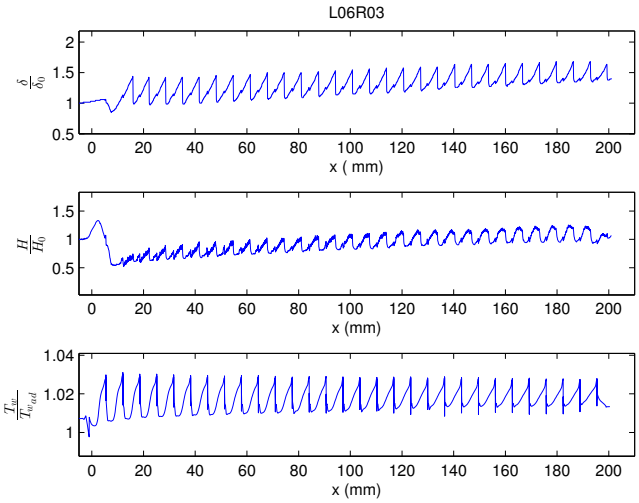

Figure 6.16: L06R03 geometry wall and boundary layer properties

Figure 6.16 shows the L06R03 properties. What can be observed is that the boundary thickness fluctuations become less than in the previous cases. The shape factor fluctuates

with the frequency of the roughness elements, but the amplitude of the fluctuations is small, which indicates a small influence of the roughness elements on the flow.

6.6 L03R02

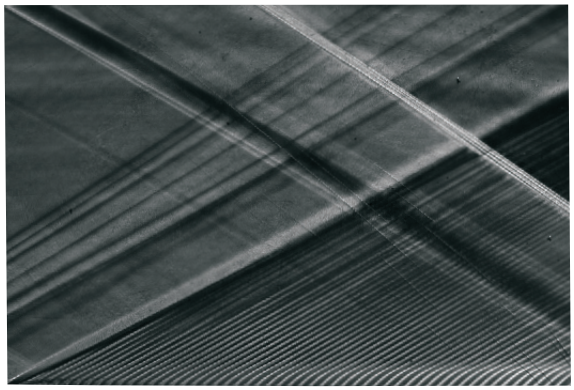

Figure 6.17: L03R02 Schlieren image

Figure 6.17 shows the Schlieren image of the L03R02 geometry. A large expansion wave can be seen coming from the from of the front of the plate. When the flow has reached the roughness elements, small shocks still emanate from the roughness elements. It must be noted that the shocks that come from the roughness elements are weaker, certainly with respect to the upstream disruptions.

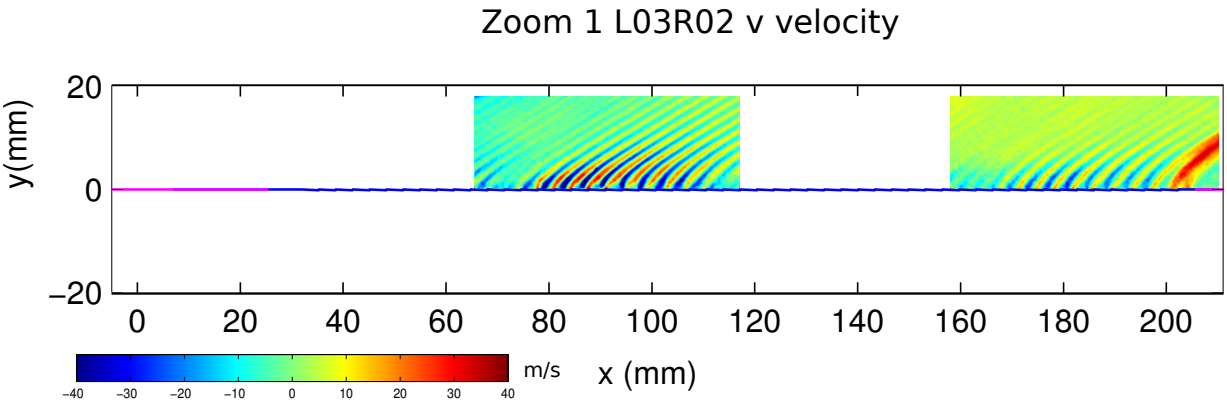

Figure 6.18: PIV results, Zoom 1, L03R02 v velocity

Figure 6.18 shows the v velocity of the L03R02 geometry. This is the smallest geometry tested. In relation to the schlieren image, the same phenomenon can be seen. The shocks in the far field are visible, but weak. At the wall the individual shocks are very small and therefore individual shocks are hard to recognize.

6.7 L33R17C

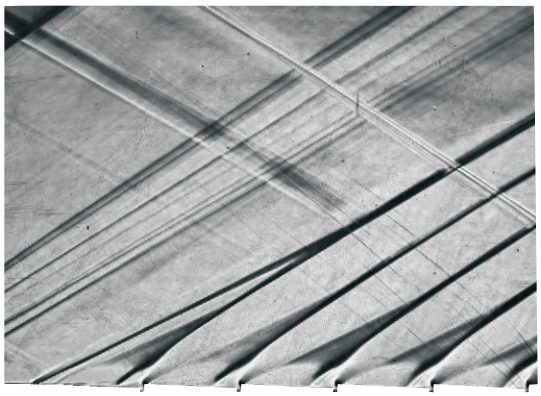

Figure 6.19: L33R17C Schlieren image

Figure 6.19 shows the schlieren image of the L33R17C geometry. Comparing the Schlieren image of the L33R17 geometry (figure 6.8) and the current image a comparable flow field can be observed. The main difference being that the cavity induces is a local difference. The point where the flow separates in the element is close to the base of the shock. It can be therefore be observed that the flow separated before the cavity, and therefore the velocities in the cavity will be relativity low.

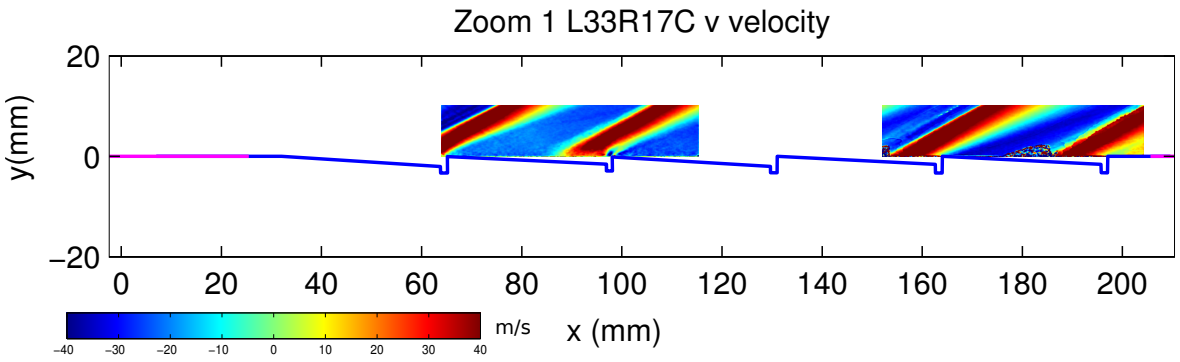

Figure 6.20: PIV results, Zoom 1, L33R17c v velocity

Figure 6.20 shows the v velocity of the L33R17C geometry. In the external flow geometry no notable changes can be observed in comparison with the L33R17 geometry which does not have a cavity, (figure 6.9).

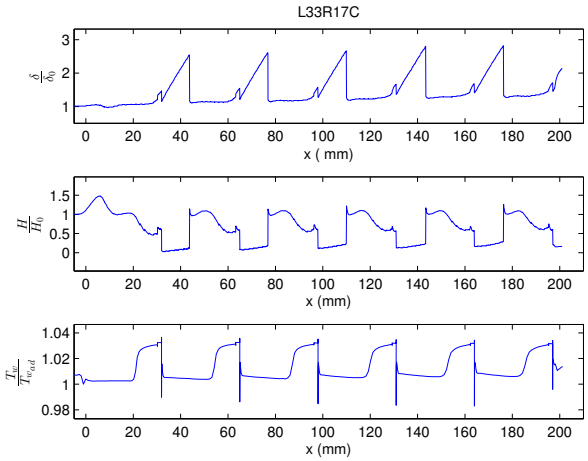

Figure 6.21: L33R17C geometry wall and boundary layer properties

Figure 6.21 shows the properties of the L33R17C geometry. The results for the boundary layer thickness, the shape factor, and the wall temperature are very similar to those of the L33R17 geometry, also implicating that the influence of the cavity is minor.

6.8 Cavity

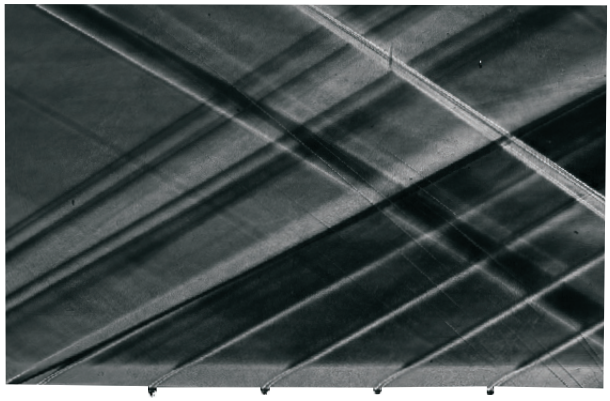

Figure 6.22: Cavity Schlieren image

Figure 6.22 shows the Schlieren image of the cavity flow. As in all the plates there is a relative large expansion wave at the start of the plate due to the transition from the insert to the plate. The cavities produce relative small disturbances that travel though the domain. The boundary layer thickness does not show clear changes in thickness.

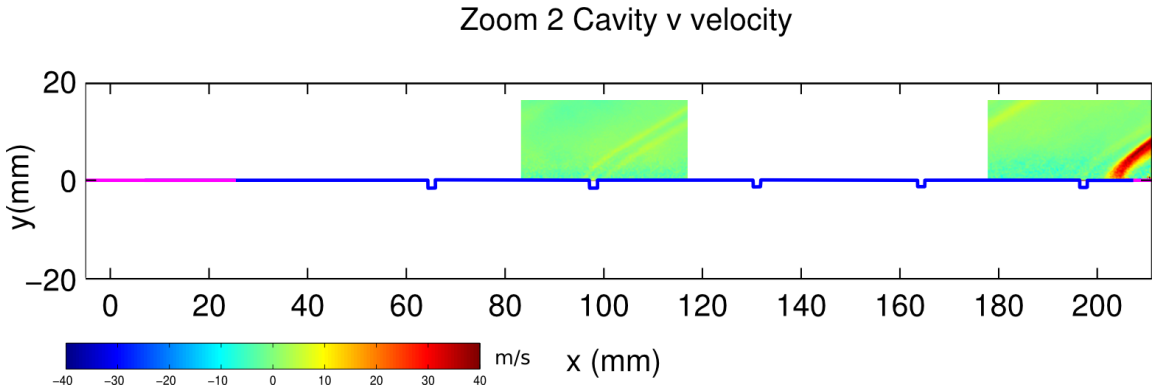

Figure 6.23: PIV results, Zoom 2, Cavity v velocity

Figure 6.23 shows the v velocity of the cavity geometry. The disturbances that the elements generate are small, even with respect to the downstream transition of the plate to the insert (205 mm).

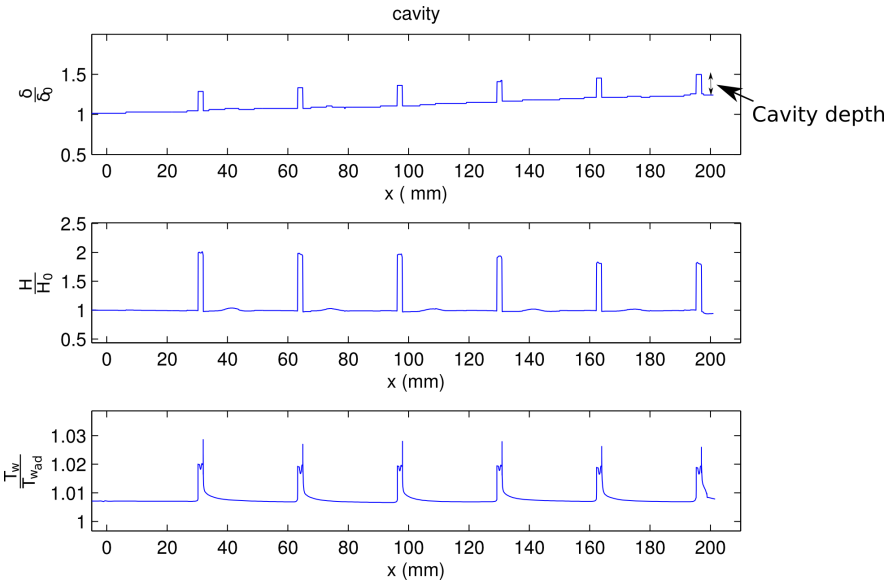

Figure 6.24: Cavity geometry wall and boundary layer properties

Figure 6.24 shows the cavity properties. The shape factor, and the boundary layer thickness show discrete jumps. This is due to the fact that boundary properties are determined from the wall position upward. Therefore in the cavities the measurement of the boundary layer thickness starts at a lower level then outside of the cavity. Apart from the discrete jumps the boundary layer does develops as a normal boundary layer. The cavities them-selfs are stagnation regions in the flow, and therefore the wall temperature increases.

6.9 Original Geometry

The original geometry was simulated with CFD to validate the assumption that the original geometry will yield a forward facing step and a cavity flow.

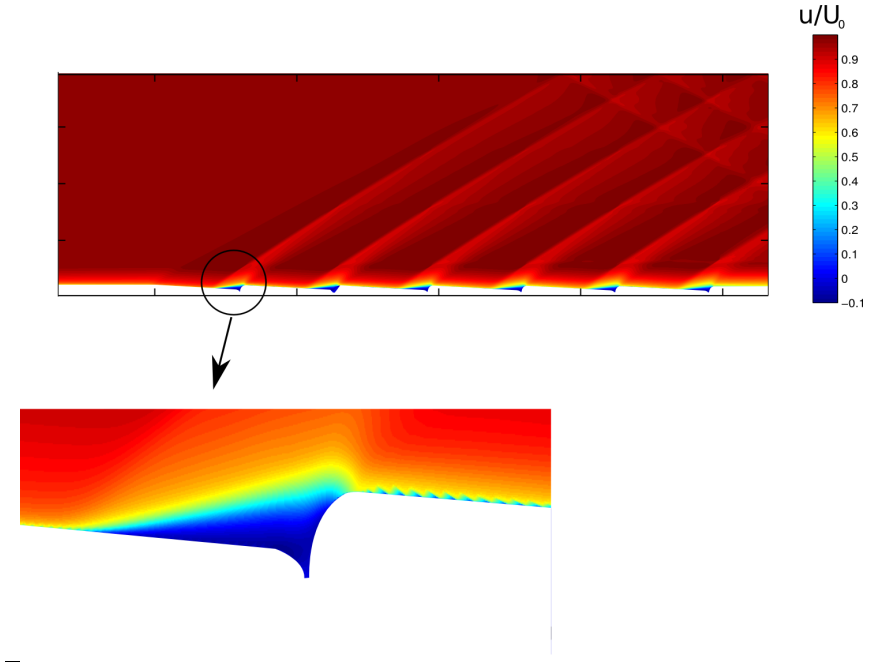

Figure 6.25: Original Geometry u velocity

Figure 6.25 shows the u velocity of the original geometry. Due to confidentiality reasons x and y values have been removed from the axis. A picture similar to all the forward facing step geometries that have been presented before can be seen. The elements show a shock wave-expansion fan train. First the flow expands into the elements, after which the flow separates to flow over the roughness element. From the zoomed section it can be seen that separation occurs on the flat part of the profile, and before the flow turns into the cavity. A contour plot for a single element is shown in figure 6.26.

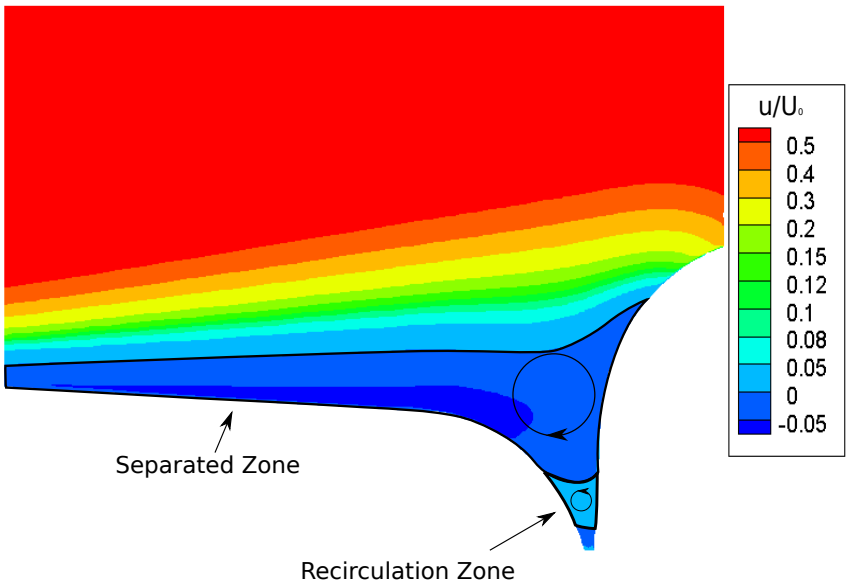

Figure 6.26: Original Geometry, individual element.

Figure 6.26 illustrates the flow in one of the elements. Important to observe in the picture is the directions of the flow. The top, large recirculation region can be attributed to the forward facing step. In the region originally attributed as cavity there is a second recirculation zone. Velocities in this region are small (in the order of 1 m/s). Therefore it is concluded that main flow features are caused by the forward facing step part of the geometry.

6.10 L10R17

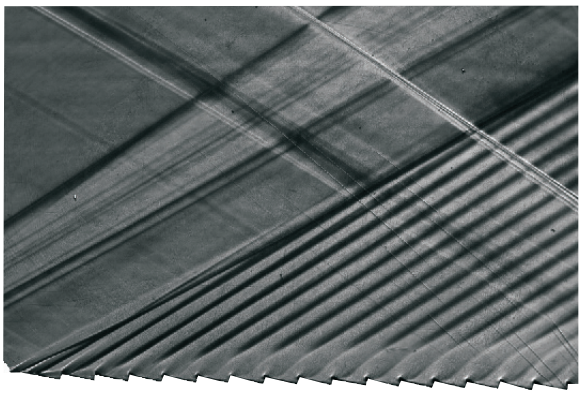

Figure 6.27: L10R17 Schlieren image

Figure 6.27 shows the Schlieren image of the L10R17 geometry. On this plate the frequency of the elements has been increased. A clear and growing boundary layer can be observed. Light expansion fans turning into each element can also be seen.

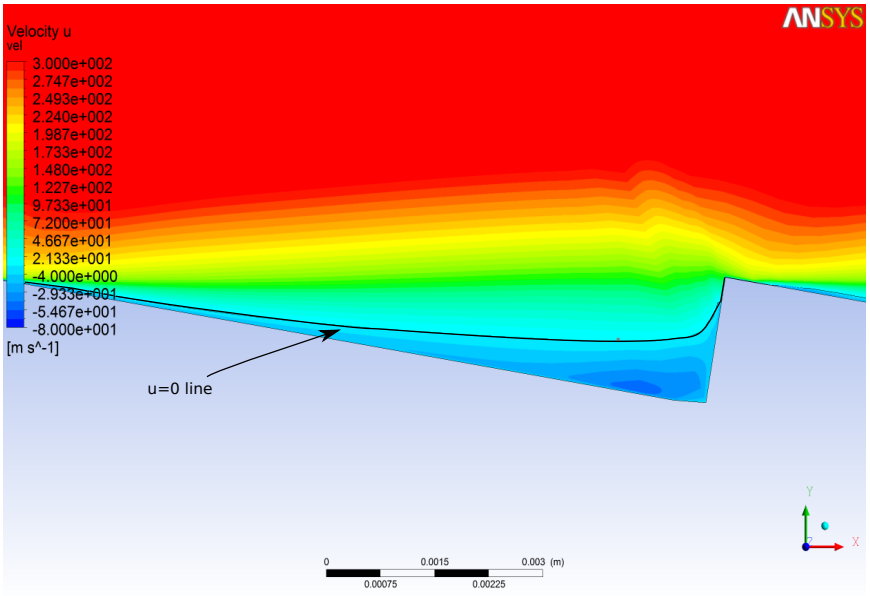

Figure 6.28: Contour plot element L10R17 geometry

Figure 6.28 shows the contour plot of the u velocity of a single element, also the u=0 ISO line has been added to the figure. It can be observed that separation occurs early in the element.

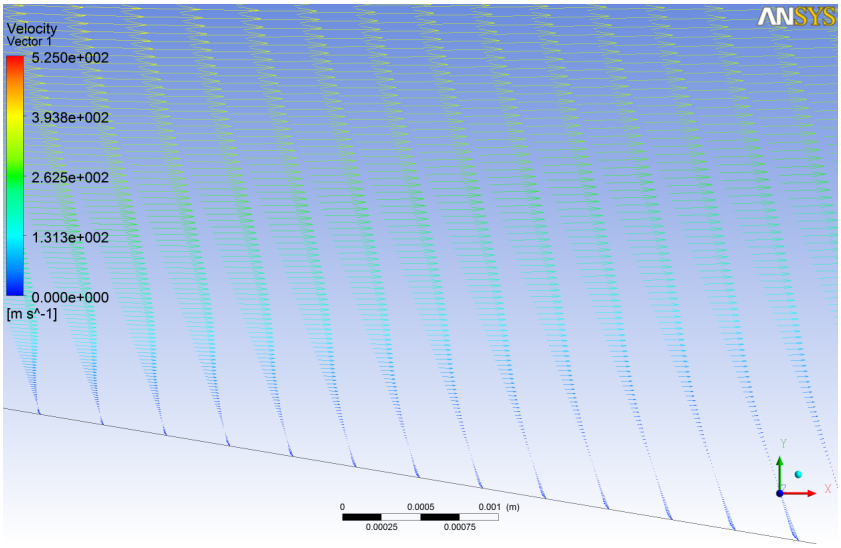

Figure 6.29: Velocity vectors L10R17 geometry

Figure 6.29 shows the velocity vectors of the L10R17 geometry. The velocity behavior of a free shear layer can be seen [10]. At the wall reverse flow occurs. It will be shown in chapter 7 that because of this shear layer the velocity gradients at the wall are very small, and therefore the viscous drag is negligible.

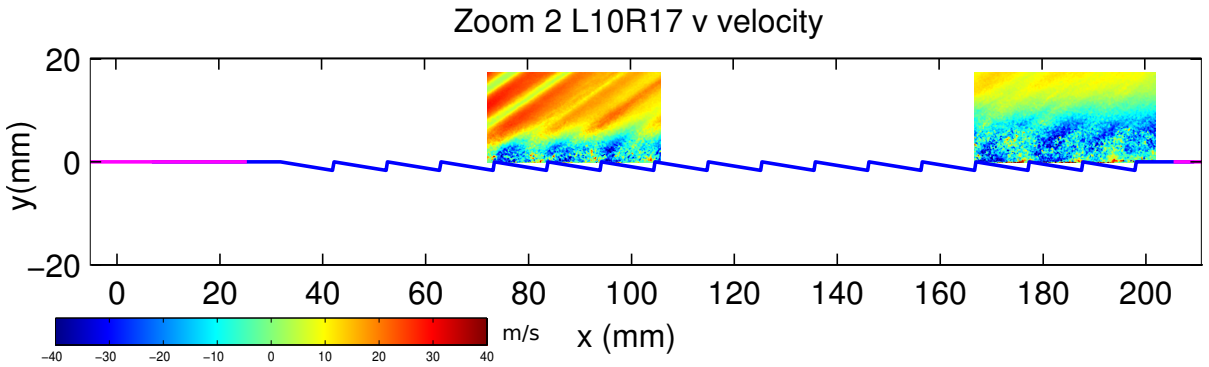

Figure 6.30: PIV results, Zoom 2, L10R17 v velocity

Figure 6.30 shows the v velocity of the L10R17 geometry. From this data it can be observed that there is a large boundary layer growth when flowing downstream over the elements. Individual features emanating from individual elements cannot be seen anymore.

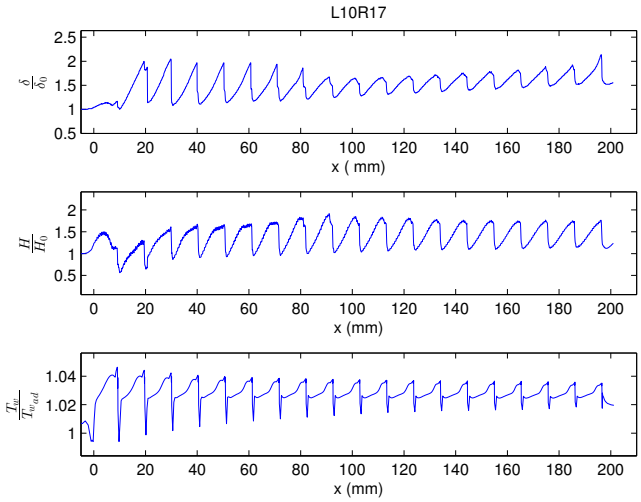

Figure 6.31: L10R17 geometry wall and boundary layer properties

Figure 6.31 shows the properties of the L10R17 geometry. The boundary layer thickness shows a fluctuating pattern associated with the elements in the plate, and a weak but steady increase. The fluctuations over the elements decrease when running over the plate. The same can be seen when looking at the Shape factor and the wall temperature.

6.11 L06R17

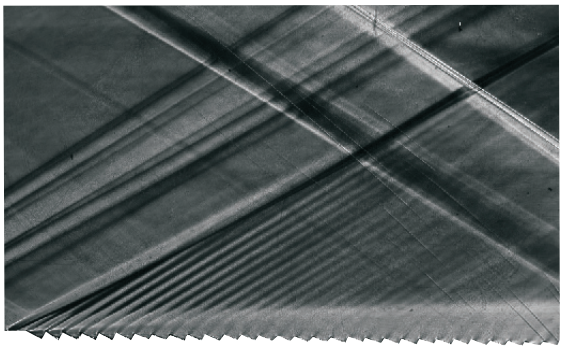

Figure 6.32: L06R17 Schlieren image

Figure 6.32 shows the Schlieren image of the L06R17 geometry. Downstream on the plate it can be seen that the shocks emanating from the boundary layer are negligible. Furthermore a clear boundary layer growth can be observed. This geometry has the same separated flow regions in the element, as the L10R17 geometry.

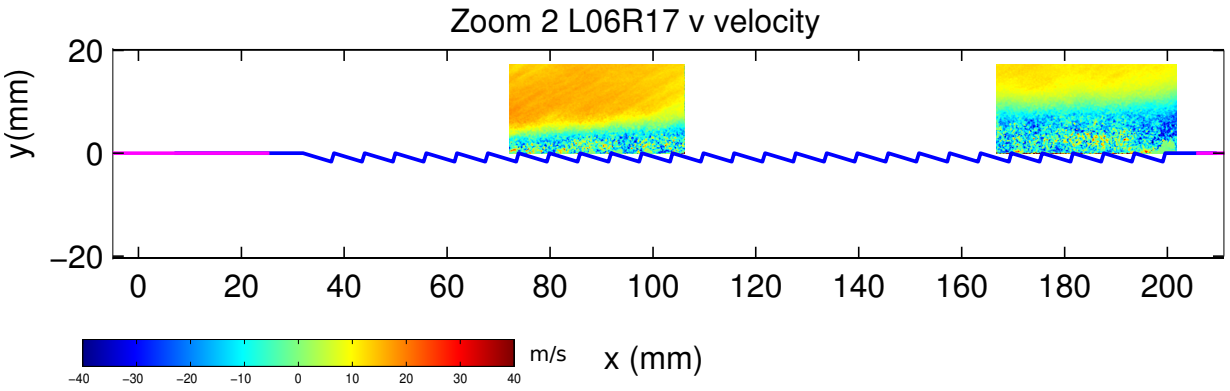

Figure 6.33: PIV results, Zoom 2, L06R17 v velocity

Figure 6.33 shows the v velocity of the L06R17 geometry. As in the L10R17 case, no individual flow phenomenon are observed.

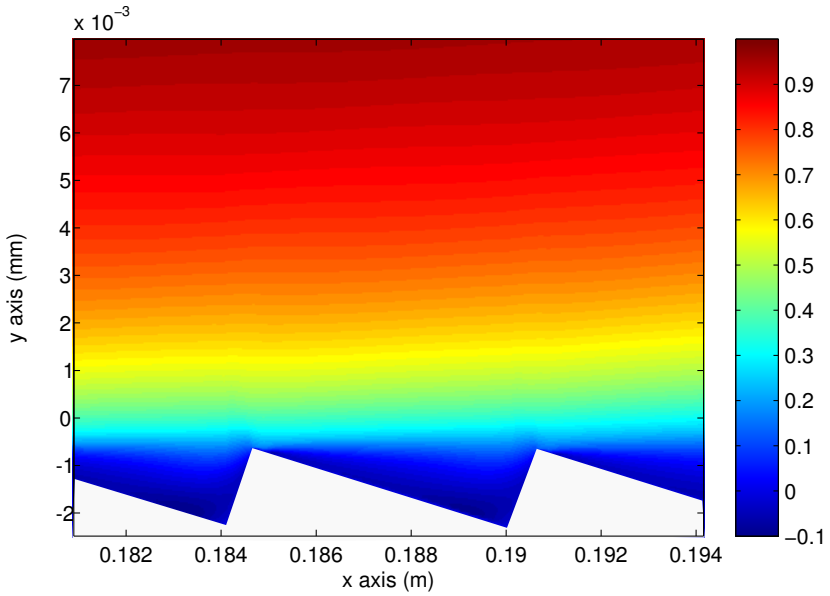

Figure 6.34: Zoom L06R17 element flow, u velocity

Figure 6.34 shows a zoom of the last elements of the L06R17 geometry. The absence of individual flow phenomena is clearly visible. The shear layer can be seen clearly, velocities inside the elements are small.

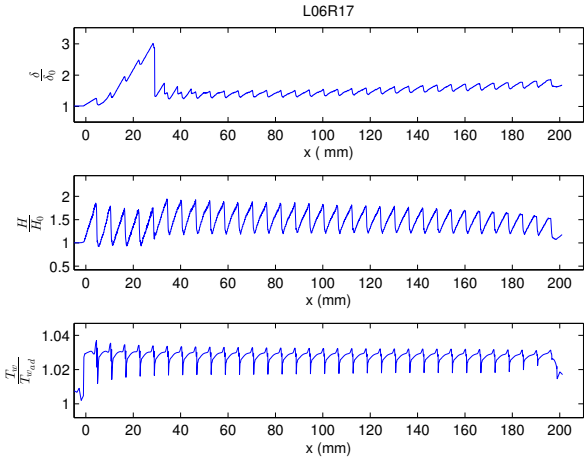

Figure 6.35: L06R17 geometry wall and boundary layer properties

Figure 6.35 show the properties of the L06R17 geometry. From the initial expansion the variations in the boundary layer thickness are minor. The same behavior can be observed with the shape factor, and the wall temperature.

6.12 Summary

From the results presented in this Chapter multiple observations can be made.
The L48R25, L33R17 and L16R08 geometries show a similar flow topology. Since the elements are long there is a piece of undisturbed flat plate flow. When the flow approaches an elements it separates, and a shock wave forms. When the flow has passed the element it expands into the next element with an expansion fan.
For the L06R03 and L03R02 geometries a boundary layer on top of the rough geometry can be observed.

For the L10R17 and L06R17 geometries cavity flow formation can be seen. The distance between the crests of the elements is small, and therefore the flow has no opportunity to attach inside an element. Therefore there is a region of separated flow inside the elements, and the main boundary layer is on top of the elements. For the L33R17C a comparable flow field can be seen to the L33R17 flow field. The results from the cavity assist in this assessment, since the disturbances caused by the cavity are minimal.

Chapter 7

Analysis

In this section the analysis of the results presented in chapter 6 are discussed. The drag forces and heat transfer are presented first. The tested flows are divided into 3 types based on the separation mechanisms. For each type of roughness a modeling approach is presented for the drag and heat transfer.

7.1 Forces

The roughness elements as presented have been been shown to influence the flow (chapter 6) and thus also the wall shear, and heat transfer. The forces and the heating that are generated will be discussed in the nest two sections, based on the numerical data. The total force on the elements is calculated by an integration of the pressure and shear data on the wall.

7.1.1 Wall integration

The forces acting on the wall are caused by the pressure, and the wall shear. Both are available from from the numerical results. Integration of these forces along the wall will yield the total force on the wall. As the roughness of the surface consists of a series of elements the forces were calculated for a single roughness element.

See figure 7.1 for the force calculation.

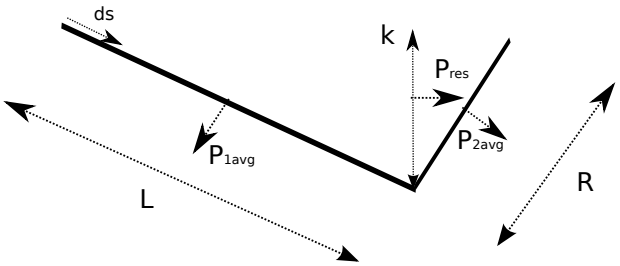

Figure 7.1: Element force breakdown

Figure 7.1 shows a model of a forward facing step. To calculate the total force on these elements the average pressure on the side with length L was calculated to be P_{1avg}, and the average pressure on the side with length R was calculated to be P_{2avg}. The resultant pressure is then P_{res}. The total force on this element can then be calculated

$$F_{tot} = P_{res} * k + F_{viscous} = (P_{2avg} - P_{1avg})\, k + \int_0^{L+R} \tau_x ds \tag{7.1}$$

The drag force given by equation (7.1) depends on the roughness height k, the difference in pressure and the line integral of the friction in the x direction τ_x.

The drag force on the wall is then obtained by applying equation (7.1) on all the elements on the wall. The drag force can be subdivided into a pressure and viscous term, which represent the force due to the pressure, and due to friction. See figure 7.2 for the friction coefficient based on the drag force for all the geometries.

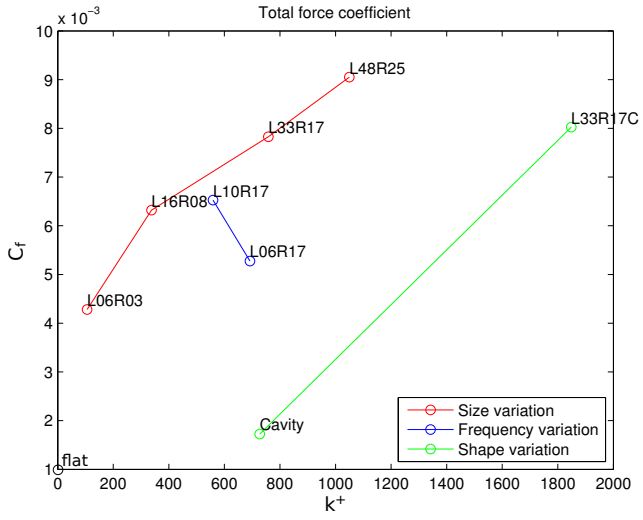

Figure 7.2: Drag coefficient Roughness geometries

Figure 7.2 shows the friction coefficients for all the geometries. The three different lines illustrate the effects of variation in size (red), of variation in frequency (blue), and the variation in shape (green). The first three data points of the red curve show a linear decrease in friction coefficient with the k^+. From the L16R08 to the L06R03 geometry the decrease is larger. The cavity shows an increase in friction with respect to the flat plate. The frequency variation, show an increase in k^+ for a decrease in the length and a decrease in friction.

To investigate which phenomenon has the strongest effect on the drag, the friction coefficients have been plotted for the force components generated by the pressure, and by the wall shear.

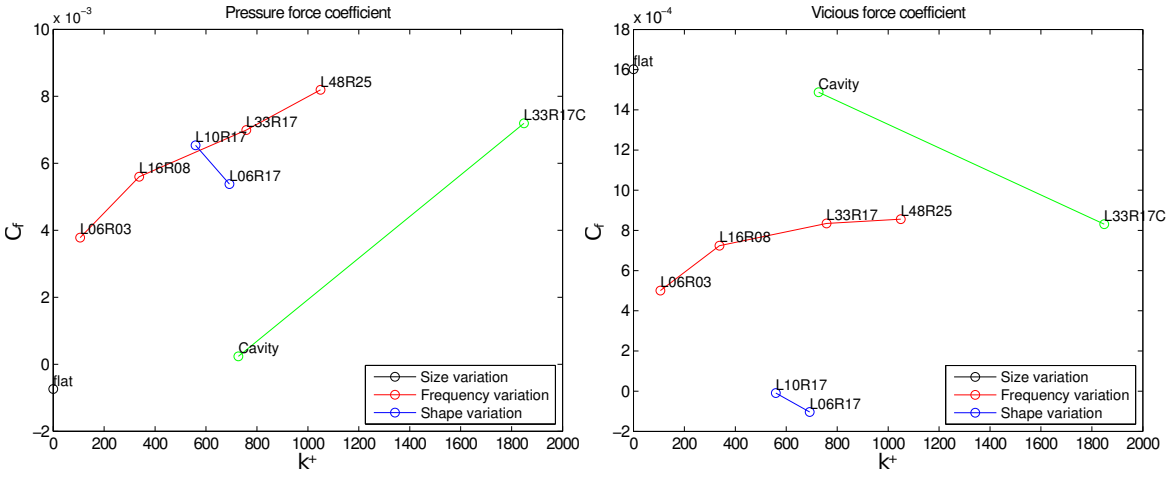

Figure 7.3: Drag coefficients due to pressure and wall shear

Figure 7.3 shows the drag coefficients due to the pressure and viscous force. Noteworthy is that the force coefficients due to the pressure are much larger then those due to the viscous forces. Thus the total forces are dominated by the pressure forces. Interesting to note is also that the viscous forces in the L10R17 and L06R17 geometries are close to zero. This is due to the fact that the flow between the elements separates, and therefore the wall sees a separated flow which is traveling much slower, than the mean flow.
With the method as presented the force is calculated for each individual element. To calculate the drag force a sum is taken over all individual elements.

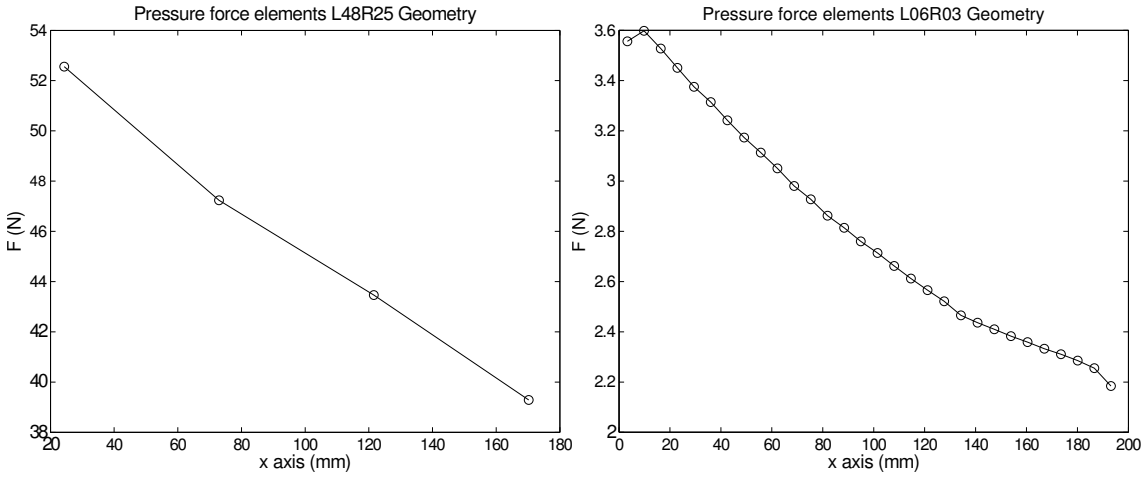

Figure 7.4: Drag distributions L48R25 and L06R03 geometries

Figure 7.4 shows the force distributions on the elements of the L48R25 and L06R03 geometries. The x locations have been taken at the mid-point of each element.

A continuous decrease in the drag can be seen.

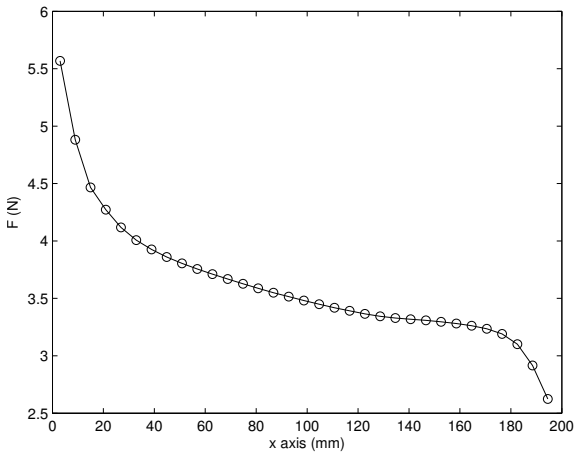

Figure 7.5: Drag distribution L06R17 geometry

Figure 7.5 shows the distribution of the pressure force for the L06R17 geometry. Again a continuous decrease can be seen. The last elements show a stronger decrease to the drag distribution than in the middle of the plate. The force is dependent on the flow Mach number. A stronger decrease of the velocity in the boundary layer could explain the current behavior.

7.2 Heat transfer

When there is no heating or cooling in a wall bounded flow, the wall temperature is driven by the flow temperature, and attains the so-called adiabatic wall temperature. When the flow has reached the adiabatic wall temperature there will be no heat transfer. On the other hand, when active control over the wall temperature is maintained, the temperature will differ from the adiabatic wall temperature, causing heat transfer. In the present study the influence of the roughness elements was studied at a wall temperature higher, and lower than the adiabatic wall temperature respectively. The adiabatic wall temperature is given by

$$T_{wad} = T_e + r\frac{U_e^2}{2C_p} \tag{7.2}$$

Equation (7.2) is the Crocco-Busemann relation for $T = T_e$, $U = U_e$, see section 4.7 for details. As can be seen the adiabatic wall temperature T_{wad} depends on the static temperature of the flow, T_e, the recovery factor r, the velocity outside the boundary layer U_e and the specific heat at constant pressure C_p. For the adiabatic wall temperature distributions, see chapter 6. To test the heat transfer the choice was made to acquire numerical data of the flat, L48R25, L06andR03 and L06R17 geometries at a wall temperature of 0.5, and of 1.5 times the adiabatic wall temperature respectively. The flat plate adiabatic wall temperature is 275 kelvin and therefore the test wall temperatures are 137.5 and 412.5 kelvin respectively. Heating is commonly described by Newtons law of cooling

$$q = h * (T_w - T_{wad}) \tag{7.3}$$

Equation (7.3) relates the heat flux q via a the heat transfer coefficient h to the difference between the wall temperature T_w and the adiabatic wall temperature T_{wad}. The adiabatic wall temperature varies with location. To evaluate the average heat transfer coefficient, a weighted average should be done on the local heat transfer coefficient. For the total heat transfer the sum on all heat transfers is required. Both are given by

$$\begin{aligned} \dot{Q} &= \int_0^{L_{tot}} q\,(s)\; ds \\ h_{avg} &= \tfrac{1}{L_t} \int_0^{L_{tot}} \tfrac{q(s)}{T_w - T_{wad}(s)}\, ds \end{aligned} \tag{7.4}$$

In equation (7.4) the total heat flux $\dot{Q}$, is given by the integral of the local heat flux over the surface. For the average heat flux the local heat transfer coefficient is calculated, and then averaged. The local adiabatic wall temperature was taken from the adiabatic numerical data.

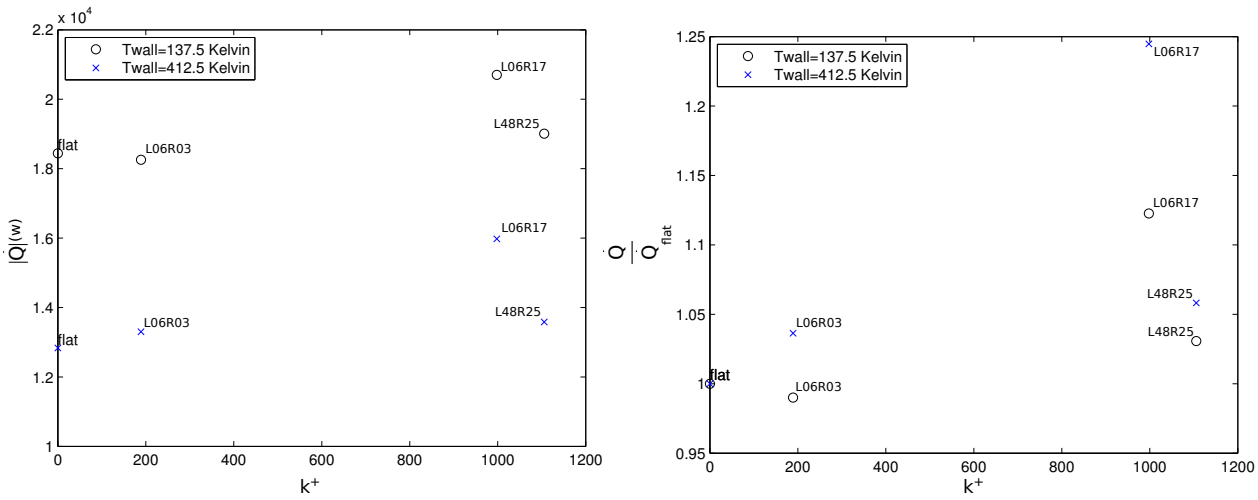

Figure 7.6: Total heat flux magnitude (left), normalized total heat flux (right)

Figure 7.6 (left) shows the absolute total heat flux for the cooled, and the heated wall. Figure 7.6 (right) shows heat flux normalized by the flat plate heat transfer. The heat flux for the cooled wall is negative since the flow heats the wall is this case. In the heated case the wall heats the flow, and the heat transfer is positive. A number of phenomena can be observed. The absolute heat transfers do not have the same value for the heated and cooled case. This is due to the fact that the boundary layer grows, by which the heat transfer reduces[25]. Due to the change in boundary layer thickness k^+ changes. Between the heated and cooled case, the distribution of the heat transfer coefficient changes.

In figure 7.6 (right) it can be seen that the data for the L48R25 geometry is differs little between the heated and cooled wall. This can be explained since this geometry is dominated by flat plate heat transfer, see section 7.6. Therefore we can conclude that changes in wall temperature have little effect on the relative heat transfer in geometries whereby the heat transfer is dominated by the flat plate heat transfer. As will be shown in section 7.6, the L06R03 geometry shows little flat plate regions, therefore the changes in heating are larger. As will be shown in section 7.6 for the L06R17 geometry the heating in influenced by the shear layer on top of the element, and not by the wall bounded flow. Therefore influences are larger then the other cases.

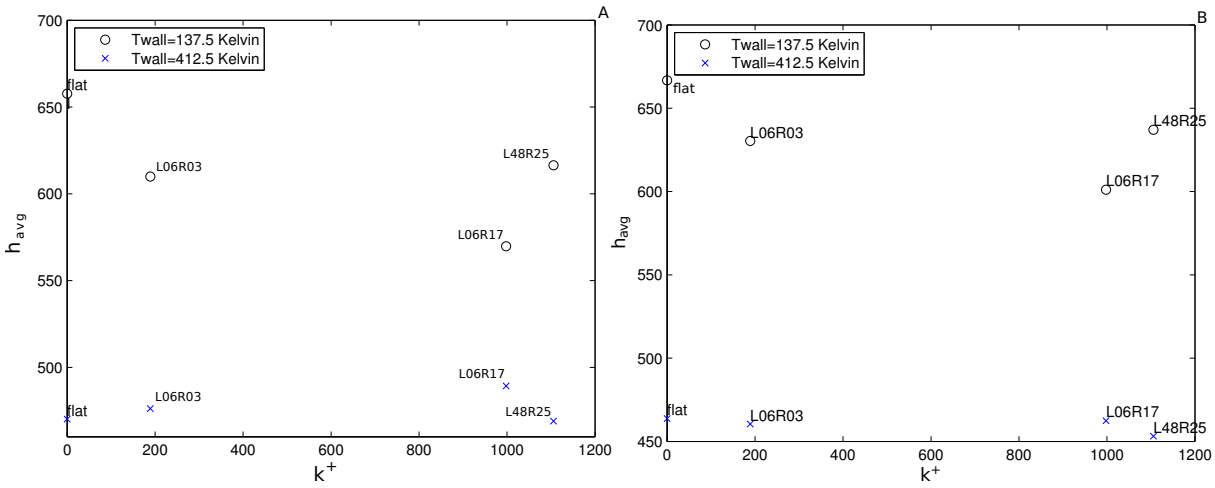

Figure 7.7: Average heat transfer coefficients, Variable T_{wad} (A), Constant T_{wad} (B)

Figure 7.7 shows the average heat transfer coefficients. In sub figure A the standard definition as shown in equation (7.4) is employed. Since the distribution $T_{wad}(s)$ is not always know, the heat transfer has also been calculated with a constant adiabatic wall temperature of 275 Kelvin. As with the absolute heat flux it can be seen that the cool wall shows a larger heat transfer coefficient, then the heated wall. Interestingly The L06R16 geometry shows a relative large heat transfer coefficient for the heated wall, while it is relatively low for the cooled wall. The main reason for this relative change is the high adiabatic wall temperature. This makes that the driving temperature difference is relatively high for the cooled wall, and relatively flow for the heated wall. This makes that although the heat flux is relatively high in both the heated and cooled wall, the heat transfer coefficients, varies.

Calculating the heat transfer with constant adiabatic wall temperature yields variations in the value of the heat transfer coefficient, since the value of the driving temperature difference changes.

It can be seen that the there is a relative shift in the geometries with respect to figure 7.6. This shift is larger then the shift in the adiabatic wall temperature since the wetted area of the geometries is included following equation (7.4).

The heat transfer that is observed is convective heat transfer, which is a viscous phenomena. Therefore it would be expected that for attached flows the heating scales with the viscous shear. It can be seen that for the L48R25 case the total heating is larger then for the L06R03 case, which complies with this assessment. The heat transfer does not scale exactly the same as the vicious shear while in the L06R03 case other mechanism also play a role. As will be shown in section 7.6 the heat transfer scales with the total drag. Because of this change there is little difference between the heat flux of the L48R25 and L06R03 geometries.

For the L06R17 case it was shown that a cavity type flow exist. Therefore the heating is governed by different phenomena. The viscous shear is negligible for the L06R17 case, but as will be shown in section 7.7 the pressure drag for the geometry is balances by a viscous shear in the shear layer. This shear layer makes that the heating is coupled to the total drag and therefore the heating is larger then the other cases.

7.3 Boundary layer development

Roughness elements disturb the boundary layer. As was discussed in chapter 2, flow over rough walls with elements under a certain height can still be characterized as a boundary layer flow. As has been discussed in section 7.1 all elements display a pressure drag that is on average a factor 10 larger then the viscous drag and which is, hence the dominant contribution to the surface drag of the rough plate. To model this pressure drag, and to reproduce the heating results a model has to be derived. A starting point is the determination if the flow can be modeled as a boundary layer flow, or as an element flow. The choice between boundary layer flow and element flow will be made on the basis of the change in boundary layer properties over the roughness element. This change in properties will be the basis of the decision into which class the elements should be positioned.

For the determination of criteria to divide the elements into a boundary layer flow, or an element flow it is import to discuss the when a profile can be called a boundary layer profile. For a profile to be deemed a boundary layer profile the log law region must remain present and any influence should be a shift in the profile. For this to be the case any disturbance should be small enough to make sure that the log law does not change. Therefore if a flow is deemed a boundary layer flow over a rough wall the roughness elements will induce small disturbances to the mean profile and therefore the profile by approximation will react similarly to each roughness element. Because a boundary layer grows the influence of the roughness will decrease and therefore a decrease of the change in boundary layer properties over the elements can be expected when moving downstream. An increase in the change of boundary layer properties when moving over roughness elements is impossible though. In this section the boundary layer thickness will be shown, and the change in boundary layer thickness when moving over the roughness elements. If this change in boundary layer thickness grows it will be concluded that the flow behaves as an element flow, while is the change decreases an boundary layer flow will be assumed.

Figure 7.8 shows the boundary layer development for the L33R17 geometry. A similar behavior is obtained for the L48R25 geometry and the original geometry.

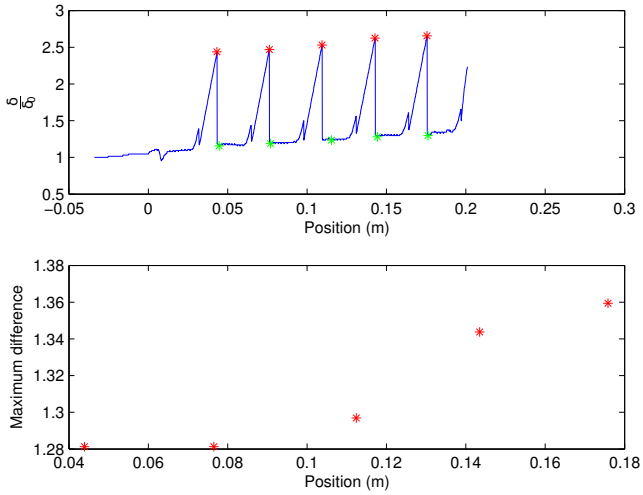

Figure 7.8: Boundary layer thickness development L33R17

The top panel of figure 7.8 shows the development of the boundary layer thickness through the test section. The bottom panel shows the difference between the maxima and minima of the boundary thickness distribution. The difference between the maxima and minima grows with the position in the test section. If the flow over these elements could be treated as a boundary layer flow the difference between the maxima and minima should not increase since this indicates non-stable behavior. Therefore this flow is not a boundary layer flow.

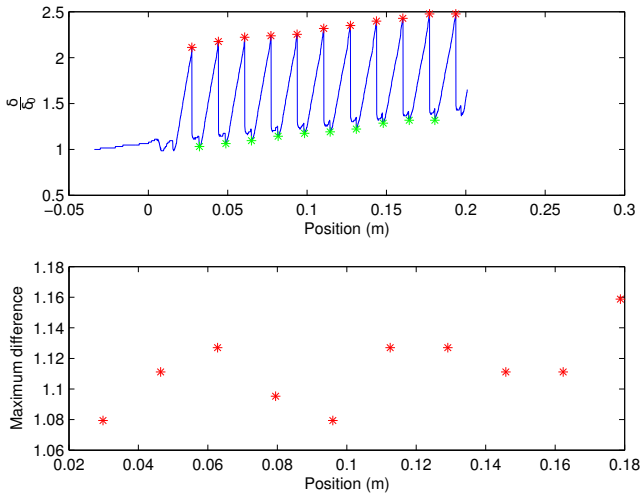

Figure 7.9: Boundary layer thickness development L16R08 case

Figure 7.9 shows the boundary layer development over the L16R08 geometry. The boundary layer development in figure 7.9 shows a varying pattern with places where the disturbances of the roughness elements die out, and there are places where the difference in the boundary layer thickness increases. From figure 7.9 no clear statement can be made on the development of the boundary layer.

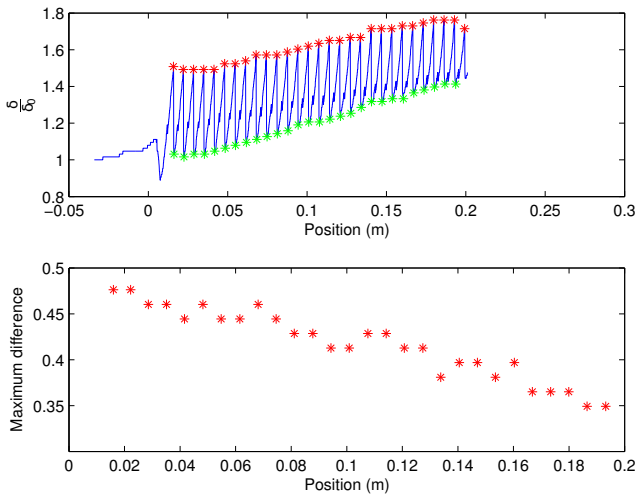

Figure 7.10: Boundary layer thickness development L06R03 case

Figure 7.10 shows the boundary layer development over the L06R03 geometry. The changes in boundary layer thickness over the elements decreases in the test section. Therefore this is a boundary layer flow.

It was shown in chapter 6 that the cavities in the wall had very little impact on the boundary layer thickness, and also the over all flow field. For the L33R17C case it was seen that the main flow had already separated before the cavity, and therefore the flow field was similar to that of the L33R17 geometry.

Figure 7.11 shows the boundary layer thickness distribution of the L06R17 geometry. A similar behavior was found for the L10R17 geometry.

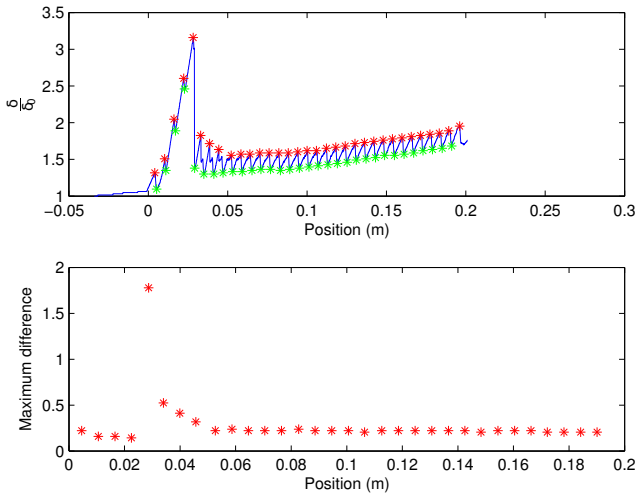

Figure 7.11: Boundary layer thickness development L06R17 case

Figure 7.11 shows that after the initial boundary layer growth due to the transition from rough to flat plate, the boundary layer quickly sets into an equilibrium state, where the boundary layer disturbances do not grow. Therefore the conclusion is drawn that flow is a boundary layer flow.

In summary the L48R25, L33R17 and L33R17C case show a growth in roughness effect in the test section, the more elements that were passed the bigger the effects become. This behavior does not suit the behavior of a boundary layer over rough elements, and therefore it must be concluded that this is not a boundary flow over rough elements. The L16R08 case does not display a clear growth or decay. The L06R17, L10R17 and L06R03 case display convergence to a stable boundary layer flow.

7.4 Boundary layer modeling

To validate if the flow at the wall behaves as a boundary layer, a boundary layer model will be fitted to velocity data.

The standard law of the wall is given by

$$u^+ = \frac{1}{\kappa} ln(y^+) + B \tag{7.5}$$

After some rewriting we obtain

$$u^+ = \frac{1}{\kappa} ln\left(\frac{y}{k}\right) + \frac{1}{\kappa} ln\left(k^+\right) + B = \frac{1}{\kappa} ln\left(\frac{y}{k}\right) + B_{rough}\left(k^+\right) \tag{7.6}$$

Equation (7.6) shows the rough walled form of the law of the wall, see chapter 2 for details. According to I. Tani [19] the constant B_{rough} goes to 8 for a value of k^+ larger then 70.

If the current geometries show a behavior where B_{rough} has a value close to 8 it can be seen as a confirmation that the boundary layer is a rough walled boundary layer. To check the behavior of the geometries tested equation 7.5 was fitted to all calculated boundary layer profiles over the roughness elements. u_τ and B_{rough} were calculated simultaneously in the fitting procedure. This procedure yielded a B_{rough} distribution over the roughness elements. The average of this distribution are shown in figure 7.12.

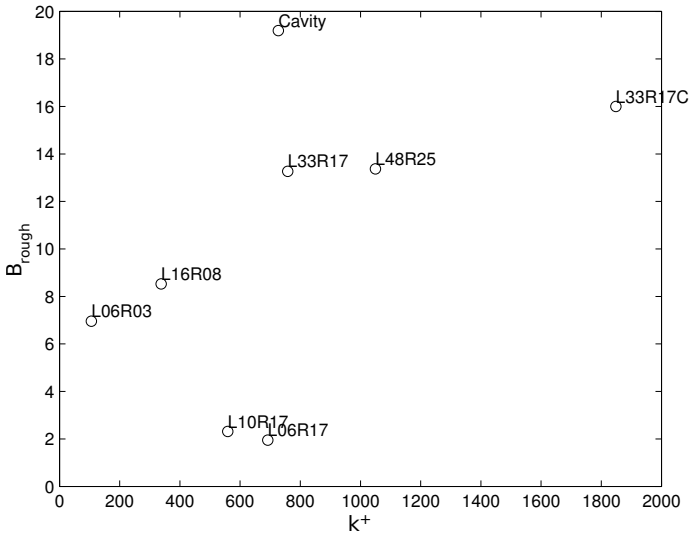

Figure 7.12: Law of the wall constant B_{rough}

Figure 7.12 shows the average value of the constant B_{rough} for the different geometries. For the L06R03 and L16R08 geometries the average value of B_{rough} lies close to 8. For the L33R17 and L48R25 geometries B_{rough} attains a value close to 13. The L10R17 and L06R16 cases show a value of B_{rough} of about 2. As was shown the cavity geometry produces a flow that is similar to the flat plat since the disturbances by the cavities are very small. The value of B_{rough} for the cavity is large with respect to the rest of the test points because applying this model to that flow, is equivalent to fitting a flat plate flow with this law of this wall. Fitting a flat plate flow with this model is impossible since the model will result in infinity, due to zero roughness height.

Interesting to note is that the B_{rough} value of the L33R17C geometry is different from the B_{rough} value of the L33R17 geometry because of the different k^+values of both geometries. The B values of both differ by 1.25. This again shows that the influence of the cavity is minor.

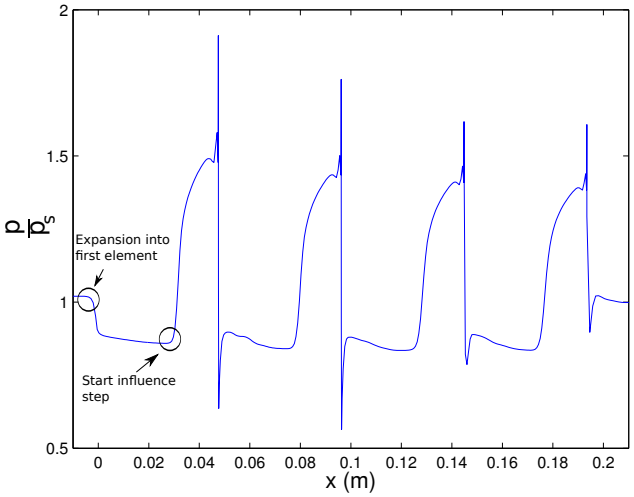

Figure 7.13: Wall pressure L48R25 geometry

Figure 7.13 shows the wall pressure on the L48R25 geometry. The L33R17 geometry displays the same behavior. It can be observed that the effects of the roughness elements are discrete. There is an expansion of the flow into an element which results in a rapid decrease in pressure. Then a section of uninfluenced flow over which the pressure varies only little, after which the flow begins to 'feel' the influence of the step and the pressure starts to rise. Due to the discreteness of the roughness element influence, the unsteady boundary layer behavior and B_{rough} values that are almost the same for the L48R25 and L33R17 geometries. The conclusion can be drawn that these geometries belong to a class of geometries with large roughnesses.

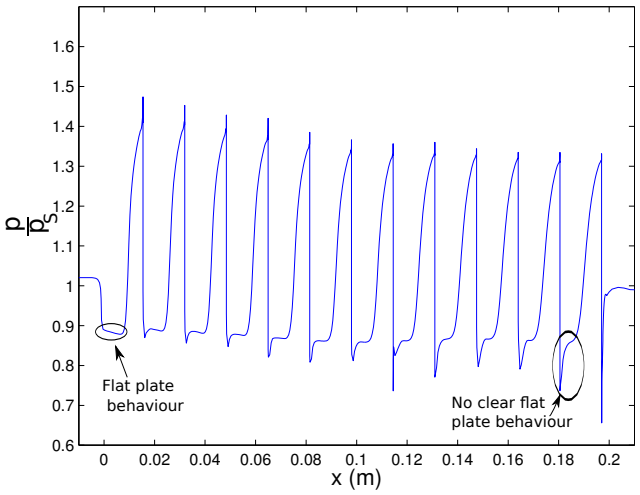

Figure 7.14: Wall pressure L16R08 geometry

Figure 7.14 shows the wall pressure of the L16R08 geometry. It can be seen that the behavior of the pressure of the elements changes. In the first element there is plat plate behavior, while in the last element, this cannot be clearly distinguished. Most elements in the pressure distribution do show flat plate behavior. For a stable boundary layer all elements should show a decrease in disturbances when traveling over the roughness elements. Since there are elements where the flow shows an increase in disturbances the L16R08 case should be placed in the same class as the L33R17 and L48R25 geometries.

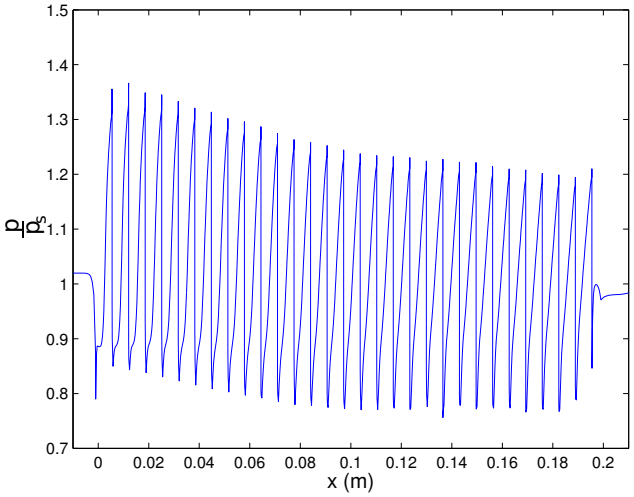

Figure 7.15: Wall pressure L06R03 geometry

Figure 7.15 shows the wall pressure of the L06R03 geometry. It can be seen that in the first element, flat plate behavior is distinguishable, but in the elements thereafter a continuous

variation of the wall pressure can be observed. Because different behavior with respect to the L48R25 geometry is observed, the L06R03 geometry represents a class of geometries where the roughness heights are small.

To have a better understanding of why these classes are as they are one should observe the separation phenomenon. In the long step geometries separation is driven by the steps. Figure 7.16 shows a density gradient plot of the flow around the L06R03 geometry.

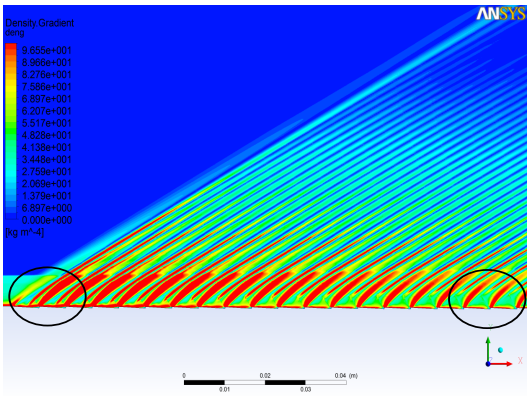

Figure 7.16: Density gradient L06R03

In the first elements of the L06R03 case it can be seen that a shock and expansion train exists. But later on the velocity has decreased by to a value that no shock is produced and there is only a small separated region in front of the elements. This can be understood when one observes figure 7.15, the wall pressure increases continuously, and therefore the separation cannot be large, otherwise this could be observed. In the L48R25 case, the influence of the step starts at a distinct point, meaning that the separation mechanism is stronger.

In the L10R17 and L06R17 case the elements are not long enough to gain reattachment in the element. Therefore they represent a special case where separation in the elements dominates.

7.5 Class determination

It was shown in the previous section that three classes of flows appear in the tested geometries, a large roughness class, a small roughness class and a cavity type roughness.

No experiments have been done to precisely determine the boundaries of these classes. Therefore boundaries as stated in theory will be used here. According to Jimenez [21] the change from a continuous boundary layer model to an element model, or the change from small roughness class to large roughness class occurs at a $\frac{k}{\delta} > 0.2$. The L16R08 geometry had a $\frac{k}{\delta}$ of 0.15 and the L06R03 case has a $\frac{k}{\delta}$ of 0.06. Therefore in the current data set the transition between small and large roughness class is between $\frac{k}{\delta}$ 0.15 and 0.06. Boundary layer development means that the boundary layer thickness varies over a section. The fraction of $\frac{k}{\delta}$ changes therefore as well over this plate, and therefore it is possible that a certain geometry has both the small and large class of flows.
In the previous section it could be seen that in the first elements of the L06R03 geometry the separation was achieved by a shock and an expansion fan train. Downstream on the plate the separation mechanism changed, which suggest that the transition point lies closer to 0.06 then to 0.15.
It was seen that the L10R17 and L06R17 geometries display cavity flow behavior. This is because the total length over depth ratio of the elements is smaller then 10. For a forward facing step as used the total length to depth ratio can be calculated by $\frac{L}{k} = \frac{Lcos(\alpha)+Rsin(\alpha)}{Rcos(\alpha)}$, see chapter 3 for the definitions of the geometry. According to van Pelt [17] a cavity flow is formed if the $\frac{L}{k}$ ratio is equal or smaller then 10. When computing the ratio for the current geometries one sees that the L10R17 and L06R17 have an $\frac{L}{k}$ ratio of 6.27 and 3.63 respectively. Therefore the current geometries are complying with ratios for cavity formation.

Table 7.1: Summary roughness classes

Model	Model used	k (mm)	L/k	k/δ	Roughness class
Flat plate	Flat plate	0	-	-	-
L48R25	Saw Tooth	2.45	19.8	0.46	Large
L33R17	Saw Tooth	1.65	19.9	0.31	Large
L16R08	Saw Tooth	0.83	19.8	0.16	Large
L06R03	Saw Tooth	0.33	19.8	0.06	Small
L03R02	Saw Tooth	0.17	19.8	0.03	Small
Cavity	Cavity	1.65	19.9	0.31	Cavity
L33R17C	Saw Tooth&Cavity	3.21	19.9	0.60	Large
Original geometry	Full	1.65	19.9	0.31	Large
L10R17	Saw Tooth	1.65	6.05	0.31	Cavity
L06R17	Saw Tooth	1.64	3.2	0.30	Cavity

Table 7.1 shows a summary of the geometries, and there roughness class. For the L03R02 geometry no CFD information was available and there no conclusive evidence that this geometry belongs to the small roughness class. Schlieren images (see chapter 6) show a flow field similar to that of the L06R03 geometry, therefore it is concluded that the L03R02 geometry also belongs to the small roughness class.

7.6 Large and small roughness class

As was stated in the previous section the roughness elements L48R25 L33R17 and L16R08 belong to a class of large roughness elements. In the current section a proposal will be made for the modeling of the drag coefficient and the heat transfer coefficient. It will also be shown that the correlation can be extended to include also the small roughness class which includes the the L06R03 and L03R02 geometries.

7.6.1 Pressure drag

The pressure drag and viscous drag analysis presented in section 7.1 shows that the pressure drag is 10 times larger then the viscous drag. Thus modeling the pressure drag on these element is important.

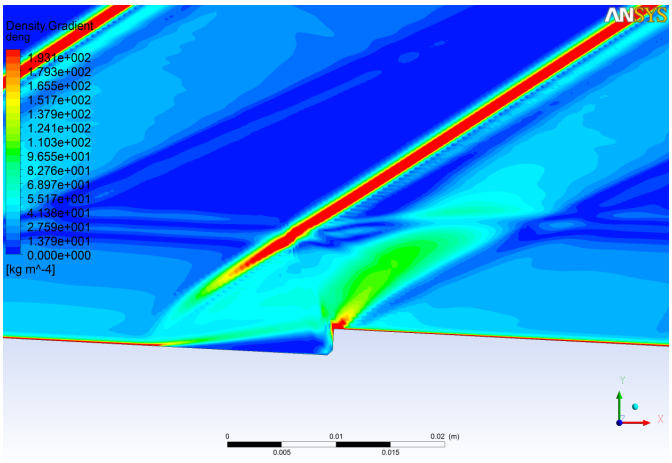

Figure 7.17: Density gradient L48R25 step

Figure 7.17 shows the density gradient in front of a step of the L48R25 geometry. In front of the step a separation region exist. This separation region triggers a shock. The oncoming flow passes through this shock, travels over the element, and via an expansion wave expands onto the next element.

Therefore the following model is proposed for the large roughness class, see figure 7.18.

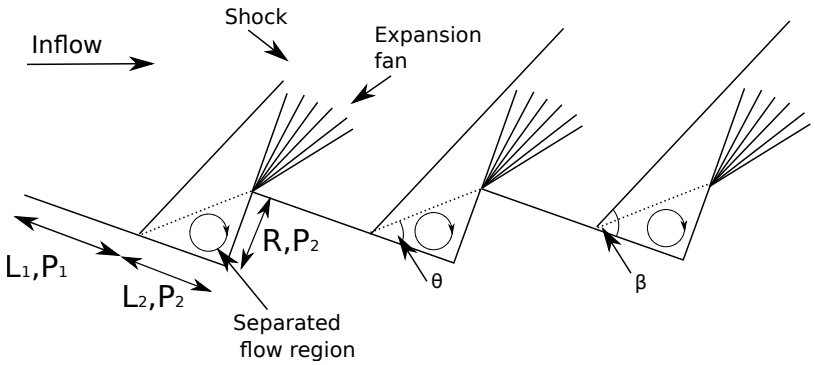

Figure 7.18: Large roughness class model

We assume that there is first a region L_1 of attached flow along the roughness element. Then there is a separated region with a length L_2. upstream of the forward facing step. The assumption is made that the pressure is constant in the separated region, and so the wall pressure on the L_2 and R length is P_2. The proposed model is such that the weighted average of P_1 and P_2 should describe the pressure over the long face of the saw tooth geometry. It will be shown later that an L_2 bigger then the separation length should be taken to yield good results.

The assumption is made that P_1 is caused by a Prandtl Meyer expansion, which means that P_1 depends on the angle under which the element is positioned. According to a Prandtl Meyer expansion, the Mach number is increased over the expansion, and with that the pressure drops. For the current case the elements are under an angle of 2.89 deg, and the initial Mach number is 2. Applying standard Prandtl-Meyer theory which can be found in any aerodynamics textbook [26], we find that the static pressure drop over the elements should be 0.787.

Table 7.2: P_1 pressure Geometries

Geometry	P_1/p_s
L48R25	0.776
L33R17	0.787
L10R17	0.797
L06R03	0.814

Table 7.2 shows the average values of P_1/p_s as obtained from the numerical data. The pressures matches well with the prediction from Prandtl-Meyer theory, therefore we can conclude that all geometries, even the L06R03 case, have a P_1 region that is governed by a Prandtl-Meyer expansion fan.

For an analysis on this geometry the size of the separated region needs to be known. Kaufman and Kirchner [28] propose a theoretical treatment whereby the separation point can be calculated as function of the step size and the Mach number. There main observation is that the the flow separates at the point where the difference between the shock angle (β), and the angle of the shear layer (θ) is at a minimum. This derivation yields an expression for the shock angle:

$$\frac{\gamma - 1}{8} M^2 = \frac{cos\left(\beta\right)^2 cos\left(2\beta\right)}{sin\left(\beta\right)^2} \tag{7.7}$$

From the shock angle, the angle of the shear layer can be calculated with the Mach-beta-theta relation, see Anderson [26].

$$tan\left(\theta\right) = 2\frac{M^2 sin\left(\beta\right)^2 - 1}{M^2\left(\gamma + cos\left(2\beta\right)\right) + 2} cot\left(\beta\right) \tag{7.8}$$

The length of the separation zone can now be calculated by

$$x_s = \frac{R}{tan\left(\theta\right)} \tag{7.9}$$

Whereby x_s is the length from the step to the start of the separation zone. To see if this model yields a correct prediction for the separation length and can be used for the drag estimate a discussion is warranted about the initial assumption made: the pressure rise starts at the separation point. Figure 7.19 is a reproduction of a figure from Zukoski [11] where he elegantly explains the pressure build up before a forward facing step.

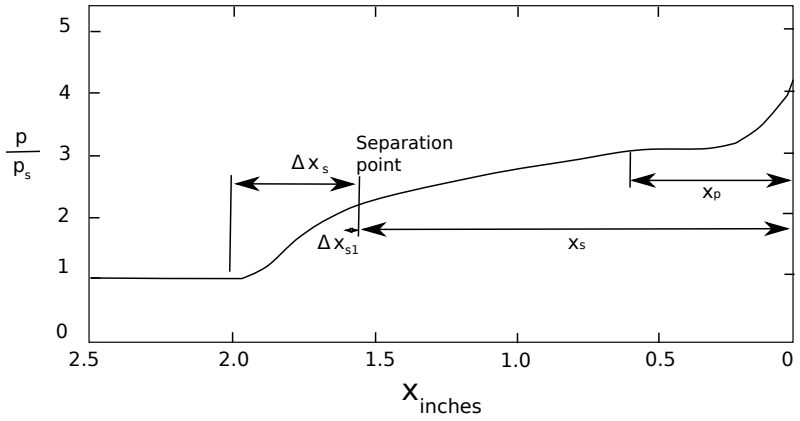

Figure 7.19: Pressure build up forward facing step

The step location is defined to be at x=0. Figure 7.19 shows that the pressure build up starts a distance $\triangle x_s$ from the separation point. The separation point is a distance x_s away from the step, and at a distance x_p before the step the pressure stays constant before the stagnation point. The value of L_2 should be such that the weighted average of P_1 and P_2 yields the average pressure on this side of the element. Therefore, using Zukoski reference frame we can write

$$\int_0^{x_p} pdx + \int_{x_p}^{x_s+\triangle x_s} pdx + \int_{x_s+\triangle x_s}^{L} pdx = L_1 * P_1 + L_2 * P_2 \tag{7.10}$$

In equation 7.10 the flow positions from Zukoski are related to the model from this author. The term $\int_0^{x_p} pdx$ indicates the force generated by the stagnation pressure. As can be seen from figure 7.19 this pressure can be taken constant by approximation and it can be calculated with equation 7.14. The term $\int_{x_s+\triangle x_s}^{L} pdx$ represents the force generated by the wall section which is not influenced by the step. This pressure can by approximation also taken constant and can be calculated by a usage Prandtl-Meyer theory as was shown in table 7.2. A proper determination of the term $\int_{x_p}^{x_s+\triangle x_s} pdx$ is therefore important to be able to determine L_1 and L_2. Incorporating both constant pressures we can write:

$$(L - (x_s + \triangle x_s))\, P_1 + \int_{x_p}^{x_s+\triangle x_s} pdx + x_p P_2 = L_1 * P_1 + L_2 * P_2$$

whereby :

$$\int_{x_p}^{x_s+\triangle x_s} pdx = \int_{x_p}^{x_s} pdx + \int_{x_s}^{x_s+\triangle x_s} pdx$$

Setting the pressure in the term $\int_{x_p}^{x_s} pdx$ constant as the stagnation pressure, and setting the pressure in the term $\int_{x_s}^{\triangle x_s} pdx$ constant as the pressure calculated by Prandtl-Meyer theory,

yields an underestimate for the size of the separation zone. Therefore this author proposes the following:

$$\int_{x_p}^{x_s+\triangle x_s} pdx = \int_{x_p}^{x_s+\triangle x_{s1}} pdx + \int_{x_s+\triangle x_{s1}}^{x_s+\triangle x_s} pdx = \left(\left(x_s+\triangle x_{s1}\right)-x_p\right)P_2 + \left(\left(\triangle x_s - \triangle x_{s1}\right)P_1\right)$$

Therefore we can now write

$$\left(L - x_s + \triangle x_{s1}\right)P_1 + \left(x_s + \triangle x_{s1}\right)P_2 = L_1 * P_1 + L_2 * P_2 \tag{7.11}$$

From equation 7.11 it can be seen that L_2 should be taken as

$$L_2 = x_s + \triangle x_{s1} = \frac{R}{tan\left(\theta\right)} + \triangle x_{s1} \tag{7.12}$$

In equation (7.12) the term $\frac{R}{tan(\theta)}$ represents the size of the separation zone, and $\triangle x_{s1}$ the distance from the point where the pressure rise due to the step starts, to the separation point. $\triangle x_{s1}$ has been fitted to the data (figure 7.20) and for a value of 1.6 mm the model correlates well with the data.

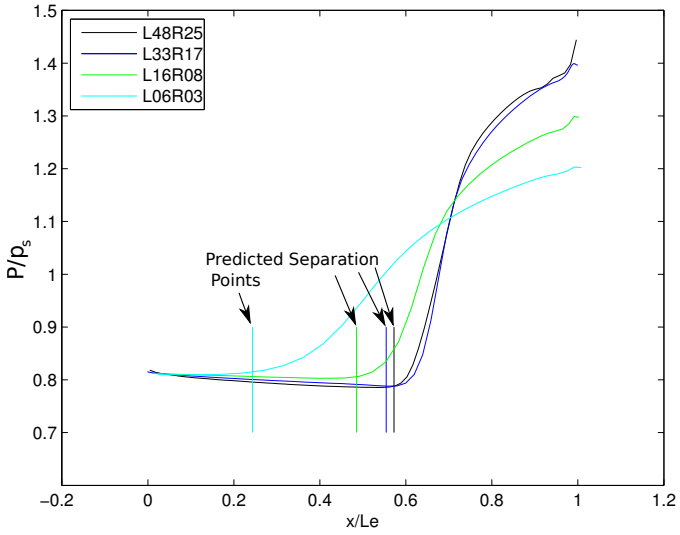

Figure 7.20: Separation point in pressure profile

Figure 7.20 shows the face pressure over the element. The x coordinate has been normalized by the length of the respective element. As can be seen the L48R25 and L33R17 geometries show a similar behavior. For the L16R08 and L06R03 geometries a clear change in distribution can be seen.

The separation point is shown including $\triangle x_{s1}$ with a value of 1.6 mm. It can be seen that the points are in the neighborhood of the point where the pressure starts to rise above the flat plate pressure. For the L06R03 case, it can be observed that almost the entire element consists of separated flow since the separation starts after 20% of the element has been passed.

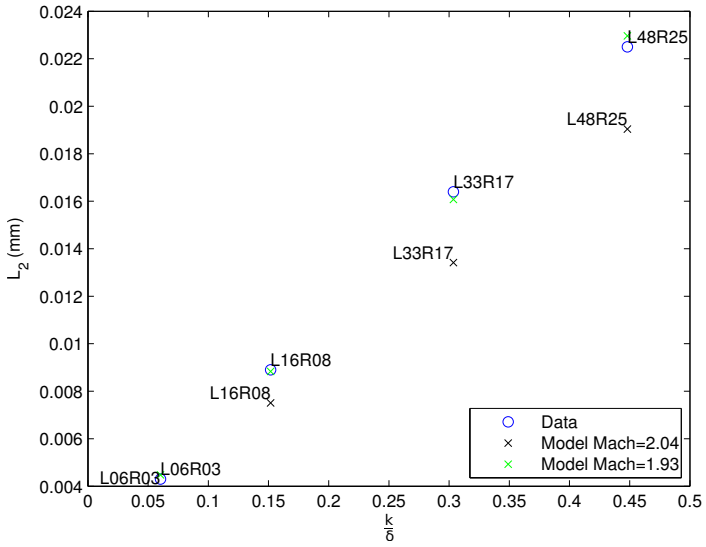

Figure 7.21: Length L_2

Figure 7.21 shows the data from the separation length, and the model prediction. The model data has been calculated with a free stream Mach number of 2.04. It can be observed that the model under-predicts the data. The model data for a Mach number of 1.93 is also shown. It can be seen that for this Mach number the model follows the data well. Because the model with Mach 1.93 follows the data well, it is concluded the the difference between the model and the data occur in the calculation of $tan\,(\theta)$, and that $\triangle x_{s1}$ is constant with roughness height for this case. Zukoski [11] shows that $\triangle x_s/\delta$ is independent of Mach number. The hypothesis of this author is therefore that also $\triangle x_{s1}/\delta$ is constant with Mach number.

To calculate the pressure two approaches where taken.

- The assumption was made that the shock is caused by the separation region, and is mainly responsible for the pressure rise

- Empirically correlate the pressure with the roughness geometry

First the shock assumption is treated. This means that the angle of the separated region is driving for the shock, which on his part drives the pressure rise. The angle of the separated region is given by:

$$\theta = atan(\frac{R}{L_2})$$

With the Mach-beta-theta relation the angle of the shock can be calculated as a function of the angle of the separated region, and the Mach number. With standard shock wave theory the pressure difference can be calculated by:

$$\frac{P_2}{P_1} = 1 + \frac{2\gamma}{\gamma - 1}\left(M_1^2 sin^2(\beta) - 1\right)$$

The results of this implementation yields:

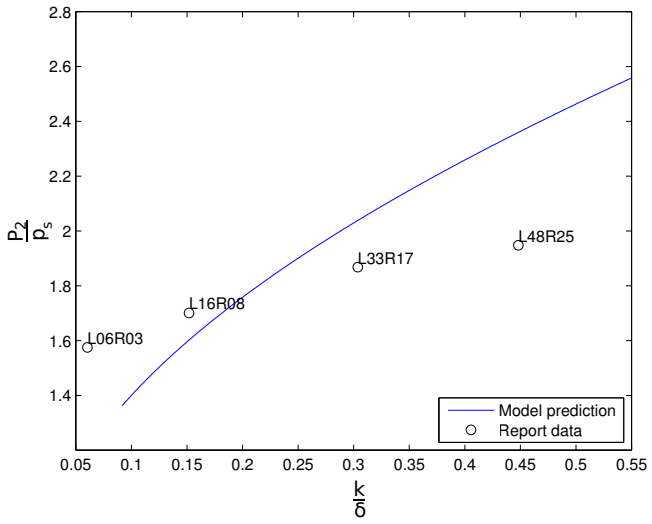

Figure 7.22: Pressure rise due to shock

Figure 7.22 shows the pressure rise due to the shock as a function of $\frac{k}{\delta}$. As can be seen in figure 7.22 the proposed model overestimates the pressure in the separated region for large $\frac{k}{\delta}$. With small $\frac{k}{\delta}$ the model underestimates the pressure rise. The Mach number used in these calculation is the Mach number at the height of the roughness element. Taking the free steam Mach number results in a large over prediction. This method still shows

large differences between the data and the model. Therefore another approach is warranted.

Another possibility is to fit a model through the current data which were obtained at Mach 2. The data sets available to the author are the data presented in this report, the data by by Bogdonoff et all [9], which was obtained at Mach 2.92 and the data by Zukoski [11] obtained at Mach 3.85. Zukoski reports a linear variation with Mach number , $N = 1$.

$$\frac{P_2}{P_s} = a * M^N \tag{7.13}$$

According to Zukoski the main parameter of influence for the geometry is $\frac{k}{\delta}$. When fitting this model to the available data it was found that a fourth order polynomial in $\frac{k}{\delta}$ is able to capture the behavior for different roughness heights. To correctly model the behavior for different Mach number it was found by fitting that an N value of 0.9 is able to collapse the data on one line.

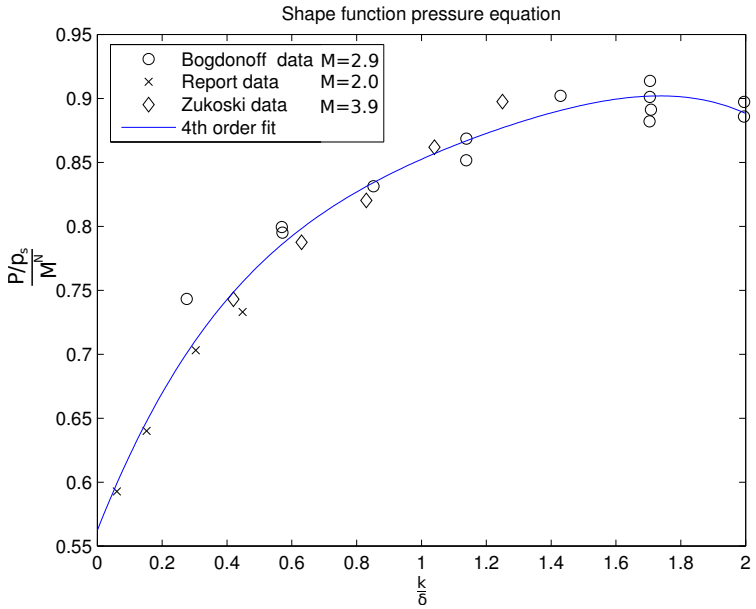

Figure 7.23: Pressure rise forward facing step for N=0.9

Figure 7.23 shows the parameter a for an N value of 0.9. The 4th order polynomial fit is able to capture the behavior of all data sets. The fit is of the following from,

$$\frac{P_2/p_s}{M^N} = a_1\left(\frac{k}{\delta}\right)^4 + a_2\left(\frac{k}{\delta}\right)^3 + a_3\left(\frac{k}{\delta}\right)^2 + a_4\left(\frac{k}{\delta}\right) + a_5 \tag{7.14}$$

With

$$a_1 = -0.062 \quad a_2 = 0.301 \quad a_3 = -0.59 \quad a_4 = 0.64 \quad a_5 = 0.56$$

Given a $\frac{k}{\delta}$ and a Mach number and equation 7.14 the pressure rise on the step can be determined. With equation (7.9) the size of the separation area can be determined. The drag on one element can then be determined by equation 7.15.

$$F_{element} = \left(P_2 - \frac{P_1 * L_1 + P_2 * L_2}{L_1 + L_2}\right) * k = (P_2 - P_1)\left(1 - \frac{L_2}{L_1 + L_2}\right) k \tag{7.15}$$

Equation 7.15 displays all the variables of influence on the pressure drag. In the case that L_1 is zero (separated flow in the entire element), the equations shows that there should be no pressure force. This being evidence that the flow field as presented in figure 7.18 does not occur in geometries L10R17 and L06R17.
Calculating the separation length by taking a Mach number of 2.04, $\triangle x_s$ of 1.6 mm and determining the pressure rise by equation 7.14 yields

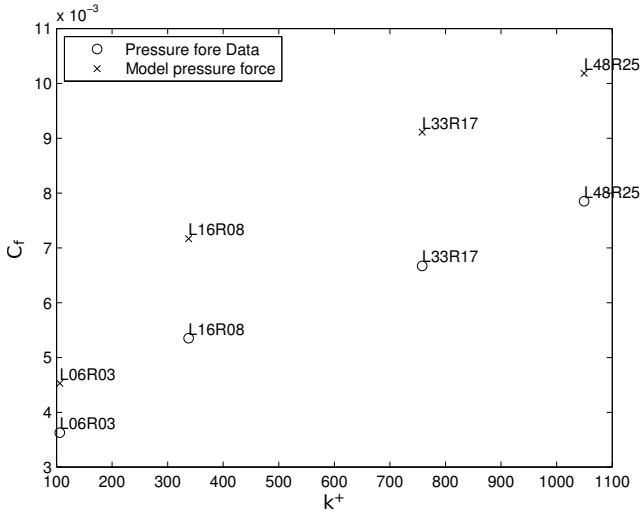

Figure 7.24: Pressure forces

Figure 7.24 shows the pressure force coefficients on the basis of the proposed model, and the current data. It can be seen that the model over predicts the data by on average 30%. It can be seen that for smaller k^+ the prediction improves. This is due to the separation model, where the prediction also improves for smaller k^+. Evaluating the separation length at a Mach number of 1.93 reduces the error in the pressure forces to a maximum of 10%.

7.6.2 Viscous drag

In the previous section the pressure drag was computed. To calculate the total force on the elements, and to calculate the heating, the viscous force is of importance. To model the viscous force two modeling strategies will be presented. One is an empirical fit through the data, and the other is a sand grain roughness approach. The empirical fit is more accurate and better on the current dataset, but has no theoretical background, while the sand grain roughness approach does have a theoretical background, and can therefore more easily be used in different flows.

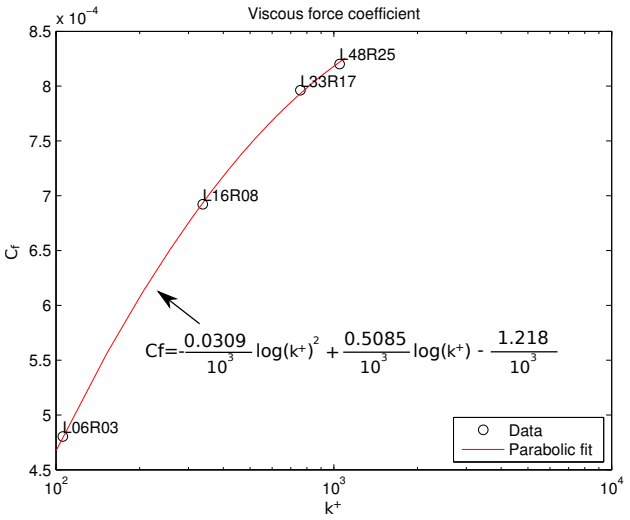

Figure 7.25: Empirical fit viscous shear

In figure 7.25 an empirical parabolic fit through the data is presented. The friction coefficient is based on the wetted area. As can be seen the parabolic fit follows the data points, but as was stated no theoretical background is available, so we cannot prove what the behavior will be with Mach number or for other geometrical shapes. We can make an hypothesis about what will change in the presented fit though. With different velocities two phenomena change with the viscous drag. The viscous shear on the parts where there is attached flow, and the size of the separation area. The viscous shear varies with a 1/5 power of the Reynolds number, while the region of attached flow varies linearly. Therefore the hypothesis of this author is that the presented fit will vary linearly with Mach number. The other option is to compute the equivalent sand grain roughness, and use this parameter. For an equivalent sand grain roughness approach the assumption is made that the average boundary layer profile can be written as:

$$u^+ = \frac{1}{\kappa} ln(\frac{y}{k_{eq}}) + B_{rough} \tag{7.16}$$

With k_{eq} denoting the equivalent sand grain roughness and B_{rough} denoting the boundary layer constant. The values for B_{rough} where presented in section 7.4. For all the computed profiles the equivalent sand grain roughness was calculated.

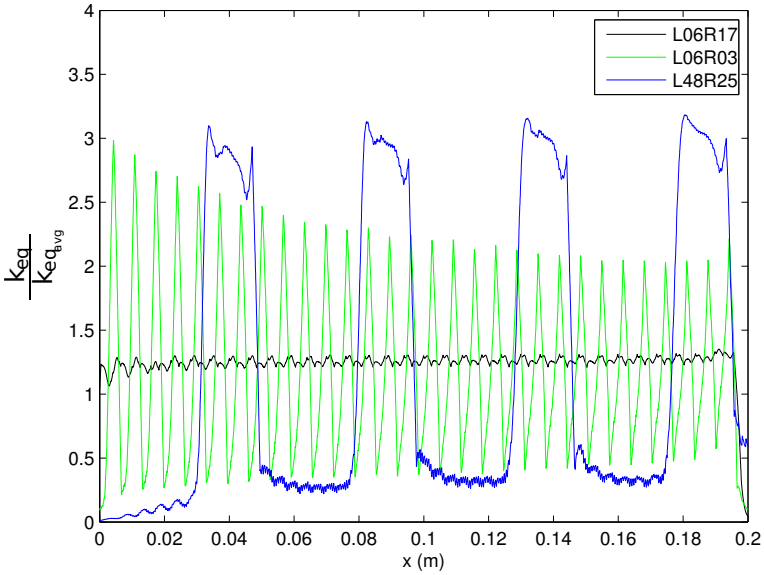

Figure 7.26: Equivalent sand grain distribution

Figure 7.16 shows the equivalent sand grain roughness distribution over the elements for the L48R25, L06R03 and the L06R17 geometries. The values have been normalized with their mean values. Significant variations around the mean value can be seen, which depend on the size of the roughness elements.

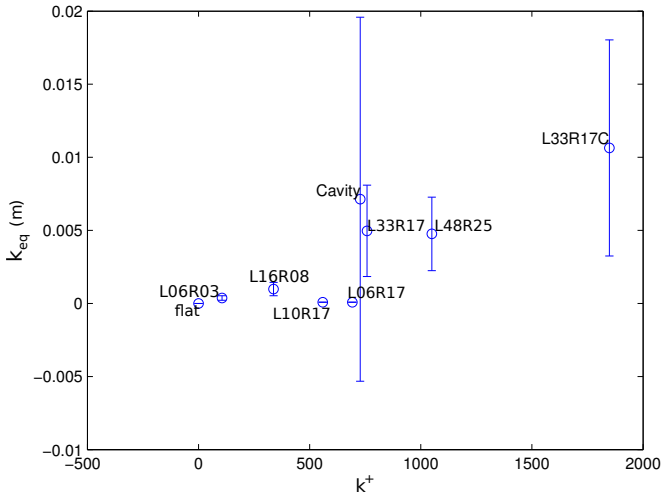

Figure 7.27: Equivalent sand grain roughness

Figure 7.27 shows, the mean equivalent sand grain roughnesses for the different configurations. The error bars indicate the standard deviation in the data corresponding to the variations as observed in figure 7.16. The standard deviations are large with respect to the mean value. No clear pattern can be distinguished between k^+ and the mean value of the equivalent sand grain roughness k_{eq}.

With the mean sand grain roughness the friction coefficient can be calculated using equation (7.17) from van Pelt[17] .

$$\frac{1}{\sqrt{\xi}} = 2log\left(\frac{Re\sqrt{\xi}}{1 + 0.1 * \frac{k_{eq}}{d} Re\sqrt{\xi}}\right) \tag{7.17}$$

In equation 7.17 $\xi = 4 * C_f$, Re is the Reynolds number based on the tunnel diameter, and d is the tunnel diameter. For the diameter of the tunnel the hydraulic diameter has been used. The current relation is based on a fully developed pipe flow. This is not the current flow case, but it was shown in [17] that this relations yields good results. Computing the friction yields the results as can be seen in figure 7.28.

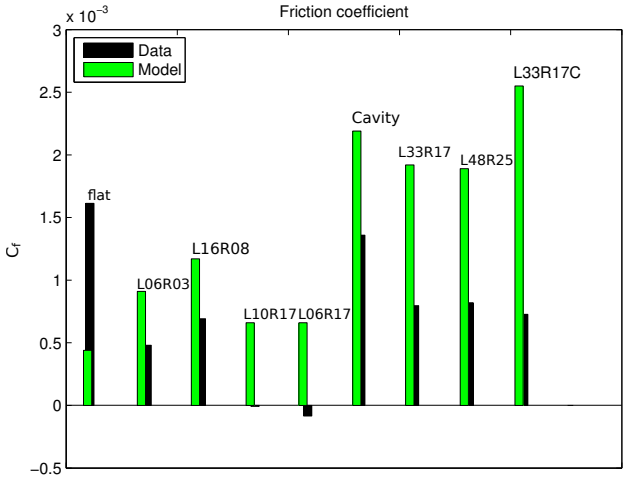

Figure 7.28: Wall friction equivalent sand grain roughness

Figure 7.28 shows the friction coefficients based on the data, and the equivalent sand grain roughness. For the flat plate case usage of an equivalent sand grain roughness model is unlogical, since the roughness is zero. For the other rough data points the over prediction of the model is due to the separation zones. For this approach, a boundary layer model was fitted to the data. In this model the intrinsic assumption is that all the wetted area contributes to the friction. In th current case there are separated flow areas which by approximation do not contribute to the friction. Therefore we define a friction coefficient

which is compensated for the separated zones:

$$C_{f_{sep}} = C_{f_{model}} * \frac{L_w - L_{sep}}{L_w} \tag{7.18}$$

With L_w denoting the wetted length of the geometry, L_{sep} is the total length of separated flow taken from the separation model presented in equation (7.9), $C_{f_{model}}$ the original C_f from the model, and $C_{f_{sep}}$ the corrected friction coefficient.

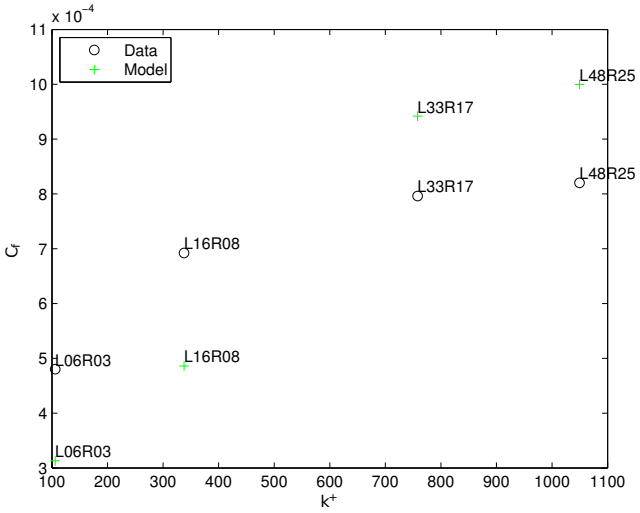

Figure 7.29: Corrected Friction coefficient

Figure 7.29 shows the corrected heat friction coefficients. It can be seen that the differences between the model and the data are smaller then in figure 7.28. For all the points the errors are in the order of 20 %. It can be observed that for the lowest two data points the model under predicts the data, while for the highest two data points, the model over predicts the data.

7.6.3 Heat transfer

The results of the previous section were obtained with an adiabatic wall condition. Therefore there is no heat transfer from the wall to the flow, or vice versa. To understand how the heat transfer is affected by the roughness elements, a number of numerical simulations where done with a heated and cooled wall. For the heat transfer Newton's law of heat transfer will be used, as was done in section 7.2. The adiabatic wall temperature was taken from the numerical simulations done with adiabatic wall condition. Figure 7.30 shows the heat transfer coefficient of the L48R25 geometry. The heat transfer coefficient has been normalized by the mean flat plate heat transfer coefficient h_0.

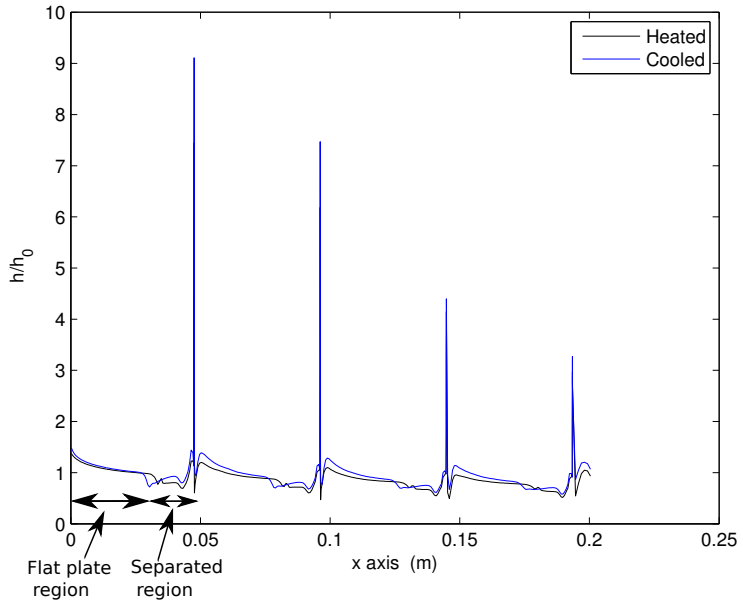

Figure 7.30: L48R25 Heat transfer coefficient

Figure 7.30 shows the heat transfer coefficient of the L48R25 geometry. The normalization has been done on the basis of the results obtained from the flat plate simulation. Two zones can be seen, a flat plate region with heat transfer coefficients around 1, and a separated region where the heat transfer coefficient is lower. It can be seen that the separation point is different in the heated and cooled case, which is due to differences in the boundary layer thickness.

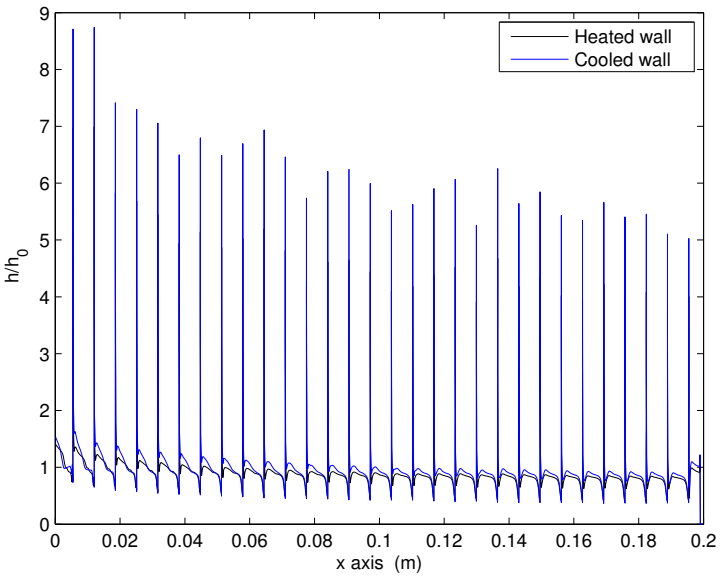

Figure 7.31: L06R03 heat transfer properties

Figure 7.31 shows the heat transfer coefficient for the L06R03 geometry. It can be seen that the heat transfer coefficients for the cooled case are larger than in the heated case. Furthermore it can be observed that the behavior is different from that in figure 7.30 in which a clear section of flat plate behavior was seen, before the heat transfer properties 'feel' the influence of the step. In the current case no such section can be seen.
For these cases it can be observed that the overall heat transfer is dominated by the attached flow regions, which behave similar as flat plate flow. Therefore it is assumed to be justified to model the heat transfer by a Reynolds analogy approach, see chapter 2. The Prandtl number is based on the reference temperature, which is calculated by

$$\frac{T^*}{T_e} = 1 + 0.0032 * M + 0.58 * \left(\frac{T_w}{T_e} - 1\right) \tag{7.19}$$

In equation 7.19 is taken from Anderson [25], T^* is the reference temperature.

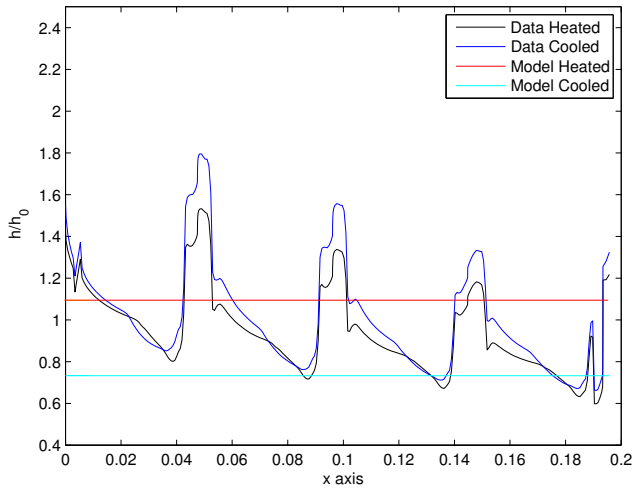

Figure 7.32: Heat transfer coefficient prediction L48R25

Figure 7.32 shows the heat transfer coefficient of the L48R25 case compared to the model. A moving average has been applied to incorporate the stagnation point heat transfer into the mean level. For this model the friction coefficient was taken from the equivalent sand grain roughness analysis. The friction coefficient was subsequently transformed via a Reynolds analogy into a heat transfer coefficient. For the friction coefficient the original friction coefficient as derived from the equivalent sand grain roughness was taken and not the prediction corrected for separation. The underlying assumption made here is that the average heat transfer coefficient on the flat plate section represents the average over the entire plate.

As was discussed for the L06R03 geometry there is no flat plate flow in the element, and therefore this method does will not yield satisfactory results.
Therefore a different approach is taken, by coupling the heat transfer to the total drag coefficient.

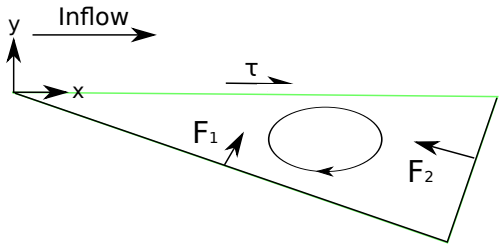

Figure 7.33: Heating control volume

Figure 7.33 shows the control volume drawn around any element by connecting the tops. Any force applicable to the walls in the x direction is balanced by shear force in flow.

Effectively this states that the total drag coefficient can be driving for the heat transfer. A shear layer is similar to a boundary layer in the sense that it reduces the velocity above the shear layer to a value below it. It is therefore deemed allowed to calculate a heat transfer via the Reynolds analogy based on the shear force in this shear layer. It was found that using the total drag coefficient for this calculation, yields an over prediction, using half of the friction coefficient and transforming this by a Reynolds analogy to a heat transfer coefficient yields good agreement with the data.

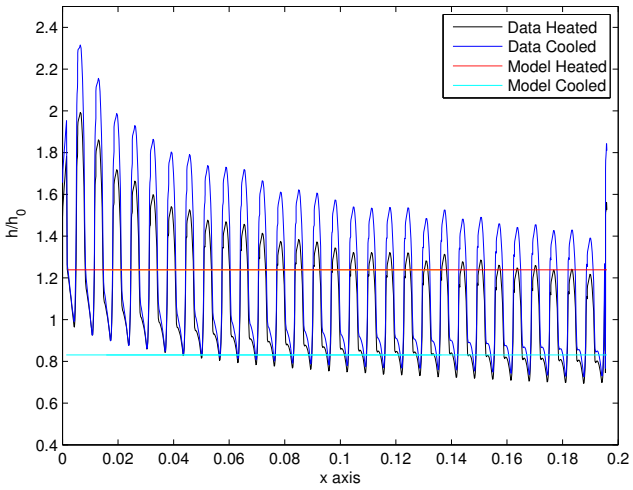

Figure 7.34: Heat transfer prediction L06R03 geometry

Figure 7.34 shows the heat transfer predictions and heat transfer values for the L06R03 geometry. Again a moving average has been applied to incorporate the stagnation points heat transfers. The heated values again exceed the cooled value.

Table 7.3 Shows the integrated values for a comparison between the mean values of the heat transfer.

Table 7.3: Mean heat transfer values

Geometry	h/h_0 Data Heated	h/h_0 Model Heated	h/h_0 Data Cooled	h/h_0 Model Cooled
L48R25	1.03	1.09	0.95	0.73
L06R03	1.23	1.25	1.11	0.81

The heated values compare well between the model and data, the differences for the L48R25 geometry are in the order of 5%, while those of the L06R03 geometry are in the order of 1.6%. For the cooled values the model shows lower values with respect to the data. Differences are 24% and 27% for the L48R25 and L06R03 geometry respectively.

7.7 High Frequency roughness class

As was presented the plates L10R17 and L06R17 are of a class called the high frequency geometries. The name refers to the high spatial frequency (short wave length) of the elements, so that a relatively depth element, with respect to its length, results. Between the subsequent elements a cavity type flow occurs. In this section the forces and heat transfer on this type of plate will be discussed.

7.7.1 Forces

As was shown in section 7.1, the drag forces of the high frequency geometries are dominated by pressure drag. Viscous drag is negligible as the viscous force is much smaller then the pressure force. Viscosity is important though when one considers the control volume as shown in figure 7.35, It is assumed that the flow behaves as a perfect cavity flow.(Region between elements completely filled with recirculating fluid).

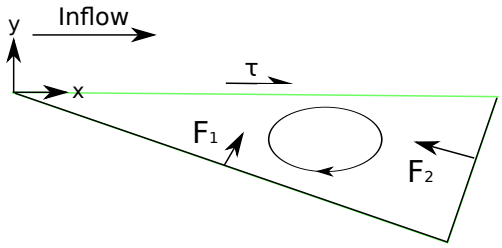

Figure 7.35: High frequency geometry control volume

In Figure 7.35 it can be seen that the flow in the high frequency elements has been modeled as a perfect cavity flow. The forces F_1 and F_2 are dominated by pressure effects. The chosen control volume shows that these pressure forces are balances by a shear stress in the flow. To compute the drag on the elements this shear stress τ will be modeled by the method proposed by McGregor and White [30].

McGregor and White assume that the velocity profile above the cavity can be written as a third order polynomial,

$$u = a_0 + a_1 y + a_2 y^2 + a_3 y^3 \tag{7.20}$$

In the third order polynomial proposed the four coefficients needs to be determined in terms of flow parameters. The parameters are solved by matching the solutions of equation 7.20

to the external flow. The solutions of the coefficients can then be written as:

$$\begin{aligned} a_3 &= \frac{2u_u+(y_l-y_u)u_u^{'}}{(y_l-y_u)^3} \\ a_2 &= \frac{-u_u^{'}-3\left(y_l^2-y_u^2\right)a_3}{2(y_l-y_u)} \\ a_1 &= u_u^{'}-(2y_ua_2+3y_u^2a_3) \\ a_0 &= u_u-(y_ua_1+y_u^2a_2+y_u^3a_3) \end{aligned} \tag{7.21}$$

where u_u is given by

$$u_u = u_\infty \left(\frac{y_u}{\delta}\right)^{\frac{1}{n}}$$

For the power law a value of n=7 has been assumed for all further implementations, the prime denotes differentiation w.r.t y. The quantities y_u and y_l are the lower and upper boundaries of the shear layer given by:

$$y_l = \frac{1.5x}{\sigma}$$

$$y_u = \frac{1.2x}{\sigma}$$

Where x is the running coordinate from the downstream corner of the cavity and σ is the mixing parameter given by

$$\sigma = 12 + 2.758 * M$$

Assuming that the shear in the center of the shear layer is representative for the average shear of the entire cavity, the drag coefficient can be written as:

$$C_D = \frac{1}{4\sigma^3}\frac{\rho_w}{\rho_\infty}\left(\frac{a_1 b}{u_\infty}\right)^2 \tag{7.22}$$

In equation (7.22) the drag coefficient of a cavity can be seen, where the subscript w represents the wall values, ∞ free stream values and b is the width of the cavity.

The results of the model are shown in Table 7.4.

Table 7.4: Results Cavity drag model

Geometry	k^+	Data C_f	Model C_f
L10R17	558.8	6.526e-3	6.0e-3
R06R17	692.2	5.276e-3	4.9e-3

The differences are in the order of 8 %, from which we conclude that the cavity assumptions works well.

7.7.2 Heat transfer

To determine the heat transfer the same strategy as with the L06R03 geometry will be used. Figure 7.14 shows the wall pressure of the L16R08 geometry. It can be seen that the behavior of the pressure of the elements changes. In the first element there is plat plate behavior, while in the last element, this cannot be clearly distinguished. Most elements due show flat plate behavior, and the boundary layer behavior did not show clear steady behavior, therefore the L16R08 case should be placed in the same class as the L33R17 and L48R25 geometries due to the unsteadiness. geometry will be followed, making the assumption that half of the total friction coefficient is the driving friction for the heat transfer. Using a Reynolds analogy then yields the heat transfer.

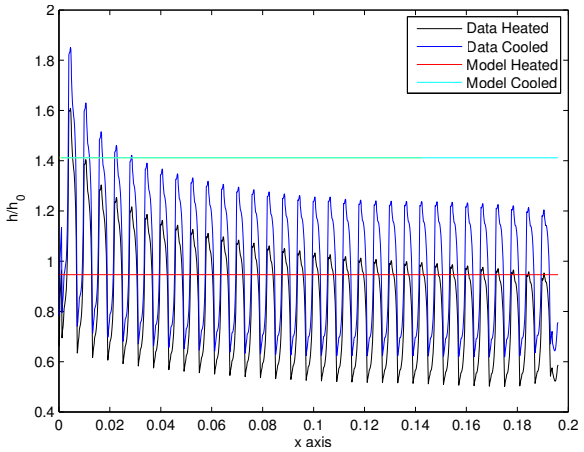

Figure 7.36: L06R17 Heat transfer prediction

Figure 7.36 shows the heat transfer coefficient for the L06R17 geometry. Due to the application of a moving average no stagnation points are visible. At the end of the plate a stable oscillatory behavior can be observed.

The numerical values are shown in Table 7.5.

Table 7.5: L06R17 heat transfer coefficients

Geometry	h/h_0 Data heated	h/h_0 Model Heated	h/h_0 Data cooled	h/h_0 Model cooled
L06R17	1.04	1.41	0.94	0.97

In the L48R25, and L06R03 geometries the heated model correlated better then the cooled version. For this geometry a reverse behavior can be seen, the differences for the cooled wall are smaller than for the heated wall. Differences are in the order of 26 and 3 % of the heated and cooled case respectively.

Chapter 8

Summary and Conclusions

8.1 Introduction

A surface can be aerodynamically smooth, or rough. The roughness of a material can have a profound influence on the flow and therefore on the drag and on the heat flux. A reliable prediction of the effects of roughness on the flow is thus important for aerodynamic design. Roughness is characterized by a k^+ value. For k^+ values lower than 5 the roughness has no influence on the flow and the effect of the surface roughness is the same as of a smooth surface. In the k^+ range of $5 < k^+ < 70$ the influence of viscosity becomes apparent on the flow behavior. For $k^+ > 70$ viscosity is of no influence anymore because the roughness protrudes into the log region of the boundary layer. When the value of $\frac{k}{\delta}$ exceeds 0.2, the shape of the individual roughness elements needs to be taken into account.

This study has focused on roughness elements with a specific shape that have been machined into a material. The shape that was used as a baseline for this research is a combination of two basic shapes: a saw tooth shape and a cavity shape. Therefore the shapes that where chosen consisted of a flat plate, a saw tooth, a cavity and a saw tooth combined with a cavity. The saw tooth shapes were further varied in their height, and in their spatial frequency.

8.2 Experimental and Numerical set-up

The geometries were investigated with a computational method, Computational Fluid Dynamics (CFD), and two experimental methods (Schlieren and Particle Image Velocimery (PIV)). The experimental approaches aimed at validating the computational results. All the geometries were investigated at a flow Mach number of 2.
The CFD investigation was done with the commercial software CFX, and with an equation set that consisted of the RANS equations. The SST and BSL Reynolds stress turbulence models were used as turbulence models. The SST model was used for most investigations, and the BSL model was only used as a reference, to check the Reynolds stresses, that were also measured with the PIV. The computational domain consisted of the nozzle geometry and the test section of the flow facility where the experimental investigations were done. The geometries of the test plates were positioned in the test section. In the computational investigations the roughness geometries were incorporated into the wall for simplicity. In the experimental investigations this was not possible, and therefore the roughness geometries were fabricated onto plates, which were held in place by a front and back insert. For validation purposes a numerical investigation was done on the exact geometry as placed in the windtunnel. Schlieren measurements have been made to validate the CFD results, and to help the understanding of the overall flow field. A set of PIV measurements where taken for a detailed experimental results. The measurements were performed at four different zoom levels.

8.3 Validation

The experiments were done in order to validate the CFD results. The validation has been done extensively on four geometries, since these produce different flow phenomena. It was found that on the inflow plane there is good agreement between the experimental and the numerical result, obtained on the same geometry. Between the experimental results and the numerical results obtained on the simplified geometry, where roughens geometries incorporated in the wall, there were differences. Analysis confirmed that this was due to the experimental set-up. At the inflow plane the boundary layer had not fully recovered from the disturbances generated by the front insert. More downstream reasonable agreement was obtained between the numerical and experimental results. Also general flow features including shocks expansion fans were compared to show that their positions matched. Velocity profiles were compared to show the agreement and differences between both sets of results. The displacement thickness and momentum thickness were compared at the beginning and at the end of the roughness elements to investigate the development of the boundary layer over the roughness elements.

Only for the geometries with increased spatial frequency a mismatch between the numerical

solution and the experimental results existed. A possible reason for this mismatch is that these elements produce such levels of turbulence that the numerical approach cannot handle this properly. The turbulence model sets a limit on the turbulence production in order to avoid false turbulence by limitations in the numerical procedures.

8.4 Results & Conclusions

For the measured flow field three types of flows were found. For the largest forward facing steps a piece of undisturbed flat plate flow was observed. When the flow approaches the step there is an increase in pressure which is followed by separation. At this point a shock is produced and the separated region is covered by a shear layer.
At small roughness height the behavior of the separated region is different from the larger cases. There has been no detailed investigation on the point where the flow changes between these two cases. From literature the change between the two cases is at $\frac{k}{\delta} = 0.2$.
For the geometries with increased spatial frequencies early separation was found. The separation was caused by the pressure gradient induced by the high angle of the wall with respect to the mean flow. In these cases the flow displays a cavity type behavior. The cavity flow caused minor disturbances in the mean flow. Noteworthy here though is that a steady simulation has been done. Multiple investigators, for example [8], have shown that unsteady behavior in a cavity flow can have large influences on the results.

For the forward facing step plus cavity geometry, it was shown that the flow separates before the cavity was reached. Then the cavity only sees separated flow and its influence is minor.
To model the results each class of roughness models was treated differently. It was shown that the large and small roughness class could be studied with the same model for the drag. The pressure and friction were modeled differently. For the pressure a model was proposed in which the stagnation pressure was modeled by a fit. This fit was able to predict the behavior for difference in Mach number and different roughness heights. The pressure before the separation point was found to match well with the pressure obtained from a Prandtl-Meyer expansion wave. For the separation length a function of Mach number and roughness height was found to work well.

For the heat transfer the large and small roughness class were modeled differently. It was found for the large roughness class that the heat transfer could be modeled quite well when the average friction of the flat plate sections of the geometry was converted into a heat transfer coefficient with a Reynolds analogy. The friction coefficient can be calculated with a equivalent sand grain roughness approach.
For the small roughness class no clear flat plate section could be seen and therefore the last approach did not work. For the small roughness class, half of the total friction coefficient

was found to be driving for the total heat flux.
For the high frequency elements the friction was modeled by assuming a cavity flow. The amount of shear in the shear layer was modeled. This agreed well with the found friction coefficient. For the heat transfer half of the friction coefficient was found to be driving for the heat transfer coefficient. In appendix B a detailed summery of a number of important calculated quantities can be found.

In the introduction of this report the following research question was posed:

'*Determine the surface drag and heat transfer over a non-smooth wall, where the size of the non-smooth profiles ranges from small w.r.t the boundary layer thickness, to in the same order of magnitude of the boundary layer thickness*'.

To answer this question, we have proven that depending on the size and distribution of the elements a certain flow type will establish. Large roughness flow establishes, for roughness larger than $\frac{k}{\delta} = 0.2$. Drag increases by a factor of 9-13 depending on the roughness height have been shown. Heating on the non-adiabatic walls remains within 7 percent of the flat plate value. Small roughness flow establishes for roughness smaller then $\frac{k}{\delta} = 0.2$. Drag increases have been measured by a factor of 4.7 and heating varies between 7 precent of t he flat plate value. It can therefore be concluded that any element in the large and in the small roughness class causes a large increase in drag and heat transfer.

If the length to height ratio of the roughness element is smaller than 10, a cavity type flow will set in. Friction increases of 6.1 and 7.5 times the flat plate friction were measured. Heat transfer variations on the non-adiabatic walls of 14% with respect to flat plate value have been shown.

Chapter 9

Discussion & Recommendations

Test methods included CFD, Schlieren and PIV. For the CFD the tested geometries were included in a nozzle shape, which corresponds to the nozzle used in the test facility. In further research that includes a nozzle shape an ideal nozzle contour should be used to avoid unwanted disturbances.

The high frequency plates showed discrepancies between the numerical and experimental data. Further research on these geometries is needed to achieve good validation between numerical and experimental results. Other numerical routines (DES, LES) might improve the match between the numerical and experimental data.

The change in flow behavior from small to large roughness class has by most researchers (Jimenez[21]) been defined at $\frac{k}{\delta} = 0.2$. In the present research, however it was shown that for $\frac{k}{\delta}$ ratio smaller than 0.2 still large element flow was observed. Therefore a detailed investigation into this transitional range would be useful.

An important part of the theories presented in the report revolves around the determination of the size of the separation zone. For a proper pressure evaluation the size of the separation zone was adjusted by a constant, which for the tested Mach number yielded good results for all roughness heights. No evaluation of the adjustment good be done at different Mach numbers since no data was available. Therefore an evaluation of the separation size at different Mach numbers would yield the data necessary to evaluate the performance of the separation model at different flow velocities.

In this report three flow classes where shown to exist. Another further roughness class that general exist has not been analyzed in this report, namely material roughness. All the flows that have been analyzed were dominated by pressure, while material roughness

is completely dominated by friction. So in total there are four roughness classes.
To determine if these are all the classed the question has to be posed, 'what is the maximum height of an element to consider it still as a roughness element, and when does it become an object in the flow?'. There is no sharp transition between shapes consisting of roughness elements or of individual objects, but one can argue that a change in roughness height should have an influence on the flow. When one observes the shape function which handles the pressure rise in the large element class (Fig. 7.23), one can see a limiting behavior for large $\frac{k}{\delta}$ ratio. This means that if the elements have a $\frac{k}{\delta}$ ratio which approaches 1.6 or larger the elements become so big that there is no more pressure rise with enlargement of the elements. This means that the size of the elements is so large that the elements cannot be viewed as a roughness element anymore. Therefore we can argue that with the enlargement of roughness elements the shape will pass from the material rough class to the small roughness class to the large roughness class. In the small and large roughness class, a cavity flow behavior can occur if the elements are close together.

Bibliography

[1] Ariane 5 68th flight from French Guiana on February 7, 2013. *http : //www.arianespace.com/news − image_library/ariane5.asp*, 2013.

[2] Welding Technologies used in Rocket Engine Manufacturing. *http : //cs.astrium.eads.net/sp/launcher − propulsion/manufacturing/welding − technologies.html*, 2013.

[3] Ansys inc. ANSYS CFX-Solver Modeling Guide | Turbulence and Near-Wall Modeling 2009. *http://www1.ansys.com/customer/content/documentation/120/cfx/xthry.pdf*.

[4] Ansys inc. Discretization of the Governing Equations. *http://www.sharcnet.ca/Software/Fluent13/help/cfx_thry/i1311648.html#i1311959*.

[5] Ansys inc. Total energy model. *http://www.sharcnet.ca/Software/Fluent13/help/cfx_thry/i1299421.html#BGBCHDHC*.

[6] Ansys inc. Two Equation Turbulence Models. *http://www.sharcnet.ca/Software/Fluent13/help/cfx_thry/i1302321.html*.

[7] B. Hodge and R. Taylor. Application of the Discrete-Element Surface Roughness Model to Rocket Nozzle Heat Transfer Computation. *AIAA-91-2435*, 1991. 27th Joint Propulsion Conference, Sacramento, California, USA.

[8] C Tarn, P.D. Orkwis and P.J. Disimile. Algebraic Turbulence Model Simulations of Supersonic Open-Cavity Flow Physics. *AIAA Journal*, 34(11):2255–2260, 1996.

[9] C.E. Kepler and S.M. Bogdonoff. Interaction of a turbulent boundary layer with a step at Mach=3. *Prinston University Press*, 1953.

[10] D. E. Nestler, A. R. Saydah and W. Auxer. Heat transfer to steps and cavities in hypersonic turbulent flows. *AIAA-68-673*, 1968. Fluid and Plasma Dynamics Conference, Los Angeles, USA.

[11] E. E. Zukoski. Turbulent Boundary-Layer Separation in Front of a Forward-Facing Step. *AIAA Journal*, 5(10):1746–1753, 1970.

[12] F.M. White. *Vicous Fluid Flow, Thrid edition.* Mc-Graw Hill, 2006.

[13] G.R. Inger. Discontinuous Supersonic Flow past an Ablating Wavy Wall. *AIAA Journal*, 7(4):762–764, 1969.

[14] G.R.Inger. Compressible Boundary layer past a swept wavy wall with heat transfer and Ablation. *Astronautica Acta*, 1971.

[15] G.S. Settles. *Schlieren and Shadowgraph Techniques.* Springer, 1st edition 2001.

[16] H Fernholz. "Ein halbempirisches Gesetz für die Wandreibung in kompressiblen turbulenten Grenzschichten bei isothermer und adiabater Wand". *ZAMM Zeitschrift für Angewandte Mathematik und Mechanik*, 51, 1971.

[17] H. van Pelt. Literature Study, Heat transfer modeling in supersonic flows with large roughness heights . 2013.

[18] H.Schlichting, K.Gersten. *Grenzschicht-theorie.* Springer, 2005.

[19] I. Tani. Turbulent boundary layer development over rough surfaces. *Springer-Verlag*, 1987.

[20] J. Cousteix. Turbulence et Couche Limite. *CEPADUE-Editions*, 1st edn, 1989.

[21] J. Jimenez. Turbulent flows over rough walls. *Annual Review of Fluid Mechanics*, 36:173–196.

[22] J. Nikuradse. Laws of flow in rough pipes. *NACA*, 1950.

[23] J.L. Everhart, S.J. Alter, N.R.Merski,W.A. Wood. Pressure Gradient Effects on Hypersonic Cavity Flow Heating.

[24] Joe Yoon. First Manmade Supersonic Object. *http : //www.aerospaceweb.org/question/history/q0217a.shtml*, 2005.

[25] John D. Anderson Jr. *Hypersonics and High-Temperature Gas dynamics.* AIAA, 1st edition 2006.

[26] John D. Anderson, Jr. *Fundementals of Aerodyncamics.* Mcraw Hill, 2001.

[27] Lavision. Imager intense, Lavision. *http://www.lavision.de/en/products/cameras/piv_ cameras.php.*

[28] L.G. Kaufman, R.D. Kirchner. High speed flow separation ahead of finite span steps. *DTIC*, 1978.

[29] Lt. Robert A Hoover. NASA Dryden Flight Research Center Photo Collection: E60-6204A. *http://www.dfrc.nasa.gov/gallery/photo/index.html*, 1947.

[30] O.W. McGreGor , R.A. White. Drag of Rectangular Cavities in Supersonic and Transonic Flow including the effects of Cavity Resonance. *AIAA Journal*, 1970.

[31] P. S. Klebanoff. Characteristics of turbulence in a boundary layer with zero pressure gradient. *Naca*, 1955.

[32] PIVpart45. PIVTECH. *http://www.pivtec.com/*.

[33] Quantel. Quantel Twins BSL. *http://www.quantel-laser.com/products/item/142.html*.

[34] R. Menter. Two-equation eddy-viscosity turbulence models for engineering applications. *AIAA*, 1994.

[35] Software and Engineering Associates, inc. *Two Dimensinal Kinetics solver*. http://seainc.com/?products=product-1, 2005.

[36] T. Mathijssen. *Stereoscopic PIV on a delta wing in Supersonic flow*. Tu Delft, MSc thesis, 2008.

[37] Z. Sun, F. F. J. Schrijer, F. Scarano, and B. W. van Oudheusden. The three-dimensional flow organization past a micro-ramp in a supersonic boundary layer. *Physics of Fluids*, 2012.

Appendix A

Geometries

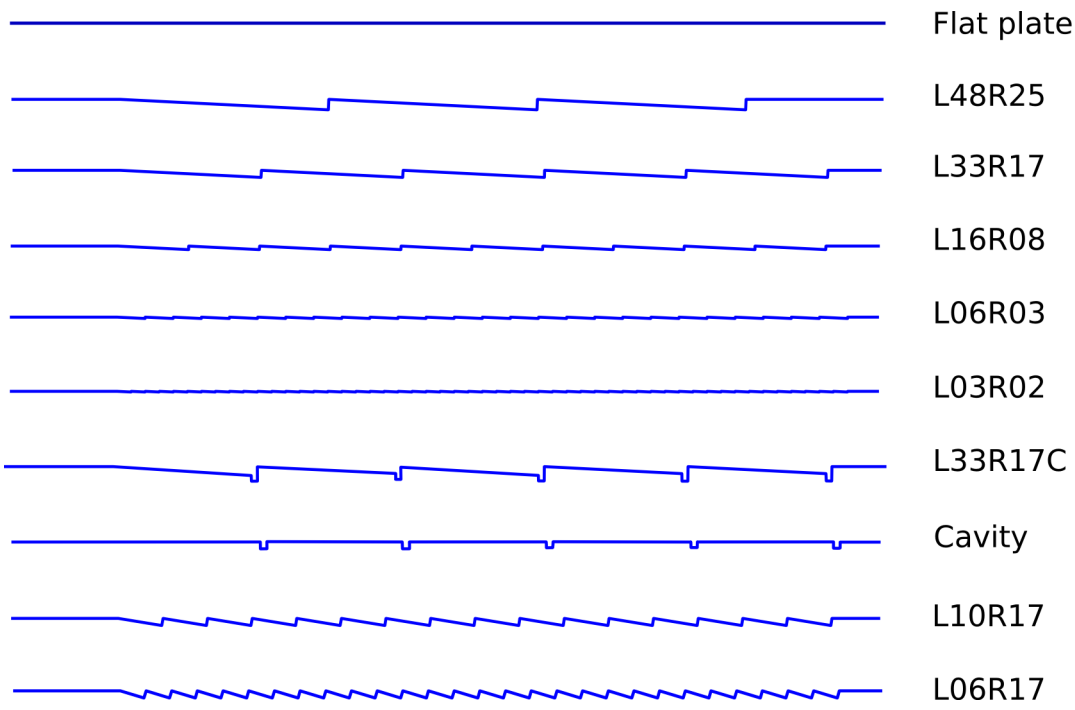

Figure A.1: Fabricated geometries

Figure A.1 shows all the fabricated geometries which have been tested with PIV. From the L48R25 to the L03R02 geometry a decrease in roughness height can be seen. The Cavity and L33R17C geometries show a different geometry. The L10R17 and L06R17 geometries show an increase in spatial frequency.

Appendix B

Numerical Results

Table B.1 shows a summary of a number of important quantities calculated in this report. The top table shows the all the geometries simulated with CFD, and there drag coefficients. The drag coefficients have been subdivided in the pressure and viscous part. The middle table shows the heat flux and the heat transfer coefficient for the cooled and heated cases. The heat transfer coefficients have been calculated with the local adiabatic wall temperature, as presented in section 7.2. In the bottom table the adiabatic heat transfer coefficients have been calculated. Thereby the friction coefficients have been transformed to a heat transfer coefficients with a Reynolds analogy. The Prandtl number required for this calculation has been calculated for the wall temperature on the basis of Sutherland law, see White [12]. As discussed in sections 7.6 and 7.7 the driving friction for the L06R03 and L06R17 geometries is half the total drag coefficient. For the L48R25 and flat plate geometries this driving friction is the viscous part of the drag coefficient.

Model	k (mm)	L/k	k/δ	Roughness class	C_f 10^{-3} total	C_f 10^{-3} viscous	C_f 10^{-3} pressure
Flat plate	0	-	-	-	0.9	1.60	-0.70
L48R25	2.45	19.8	0.46	Large	9.05	0.85	8.19
L33R17	1.65	19.9	0.31	Large	7.82	0.83	6.99
L16R08	0.83	19.8	0.16	Large	6.32	0.72	5.60
L06R03	0.33	19.8	0.06	Small	4.28	0.50	3.78
Cavity	1.65	19.9	0.31	Cavity	1.72	1.49	0.23
L33R17C	3.21	19.9	0.60	Large	8.02	0.83	7.19
L10R17	1.65	6.05	0.31	Cavity	6.53	-0.09	6.54
L06R17	1.64	3.2	0.30	Cavity	5.27	-0.10	5.38

Model	$\dot{Q}_{heated}$ (w) 10^4	$\dot{Q}_{Cooled}$ (w) 10^4	h_{heated}	h_{cooled}	$\frac{h_{heated}}{h_{heated_{flat}}}$	$\frac{h_{cooled}}{h_{cooled_{flat}}}$
Flat plate	1.28	-1.84	470.22	657.67	1	1
L48R25	1.35	-1.90	469.04	616.46	1	0.93
L06R03	1.33	1.82	476.27	609.95	1.01	0.93
L06R17	1.59	-2.07	489.30	569.74	1.04	0.86

Model	h_{heated} Adiabatic	h_{cooled} Adiabatic
Flat plate	437.30	410.11
L48R25	516.38	484.28
L06R03	518.61	545.45
L06R17	716.14	671.62

Table B.1: Numerical results, friction (top) and heating (middle and bottom)

Appendix C

Linearized flow equation with Fourier wall modeling

This report on roughness highlights the main problem of modeling flow over a rough surface. For this report experiments (CFD, PIV) had to be done to describe the behavior of the flow in relation to the roughness. Presently no method exists that is able to analytically describe the properties of the flow over an arbitrary-rough surface. This author aimed at searching for such a method by starting with a paper by Inger [14]. In this paper a set of linearized perturbation equations of the flow with harmonic wall modeling are derived. With a harmonic function both the wall amplitude and shape can be varied, but no complicated shapes can be used. To improve this, this author proposes to model the wall not with a single harmonic function, but with a Fourier series. In theory this would yield the possibility to solve the flow over more complicated surfaces, of any arbitrary rough walled shape. The goal of the section is to derive a set of perturbation equations in the same manner as Inger, but with improved wall modeling. All the terms in the naiver-stokes equation will be treated, and resulting equations will be tested.

Starting at the same point as Inger the mean flow is idealized in a first approximation as a plane parallel shear flow in the x direction. The wall is modeled as

$$y(x) = \sum_{k=1}^{N-1} \left[a_k cos\left(k\omega_0 x\right) + b_k sin\left(k\omega_0 x\right) \right] \tag{C.1}$$

With equation (C.1) and constants a_k, b_k and ω_0 set differently per desired wall shape.

The flow properties will be expanded by a mean value and a small perturbation, resulting

in

$$u = u_0(y) + E\widetilde{u}(y) \quad v = E\widetilde{v}(y) \quad p = p_\infty + E\widetilde{p}(y) \quad \rho = \rho_0 + E\widetilde{\rho}(y) \quad T = T_0 + E\widetilde{T}(y) \tag{C.2}$$

As can be seen in equation (C.2) the flow quantities are expanded as a mean quantity $(u_0\, p_\infty\, \rho_0\, T_0)$ and a perturbation term $\left(\widetilde{u}\,\widetilde{v}\,\widetilde{p}\,\widetilde{\rho}\,\widetilde{T}\right)$, E denotes the harmonic variation of the perturbation term, with

$$E = e^{i\omega_0 x} \tag{C.3}$$

The choice for this harmonic perturbation term was made because it was assumed that higher-order perturbation terms would die out, and only first-order perturbations would sustain. Taking a single harmonic for the flow perturbation, will still mean that there is no restriction on the amount of harmonics used for the description of the wall function.

Since the equations are linearized around a mean value only first order perturbation will be retained.
Since the goal is to derive perturbation equation, mean quantities will be subtracted from the final equation to remain with a set of perturbation equations.
Quasi laminar behavior will also be assumed in the perturbation field.

The first assumption is made since perturbations are small, therefore products of perturbations are so small they can be neglected. The second assumption is needed for deriving simplified perturbation equations.With these assumptions given the governing flow equations can be derived:

C.1 Continuity equation

The steady compressible continuity equation is given as (C.4), which can be found in White [12].

$$\nabla \cdot (\rho \mathbf{V}) = 0 \tag{C.4}$$

After expanding the formulation the following arises:

$$\begin{pmatrix} \frac{\partial}{\partial x} \\ \frac{\partial}{\partial y} \end{pmatrix} \cdot \begin{pmatrix} (\rho_0 + E\widetilde{\rho})(u_0 + E\widetilde{u}) \\ (\rho_0 + E\widetilde{\rho})E\widetilde{v} \end{pmatrix} = 0$$

Expanding this formulation into it's individual terms and retaining only first order perturbations yields

$$(u_0\widetilde{\rho} + \rho_0\widetilde{u})\frac{dE}{dx} + \left(\widetilde{v}\frac{d\rho_0}{dy} + \rho_0\frac{d\widetilde{v}}{dy}\right)E = 0$$

Taking the last terms of this equation together the final form of the continuity equation,

$$(u_0\widetilde{\rho} + \rho_0\widetilde{u})\frac{\frac{dE}{dx}}{E} + \frac{d}{dy}(\widetilde{v}\rho_0) = 0 \tag{C.5}$$

C.2 Momentum equation, x

According to White [12] the x momentum equation in a 2D flow field can be written as (C.6).

$$\nabla \cdot (\rho u\mathbf{V}) + \frac{\partial p}{\partial x} = \frac{\partial}{\partial x}\left(\lambda\nabla \cdot \mathbf{V} + 2\mu\frac{\partial u}{\partial x}\right) + \frac{\partial}{\partial y}\left(\mu\left(\frac{\partial v}{\partial x} + \frac{\partial u}{\partial y}\right)\right) \tag{C.6}$$

Since there are a number of terms each term will be expanded independently. Expanding the first term yields:

$$\rho u\frac{\partial u}{\partial x} + \rho v\frac{\partial u}{\partial y} = (\rho_0 + E\widetilde{\rho})(u_0 + E\widetilde{u})\frac{\partial(u_0 + E\widetilde{u})}{\partial x} + (\rho_0 + E\widetilde{\rho})(E\widetilde{v})\frac{\partial(u_0 + E\widetilde{u})}{\partial y}$$

Working this term out and neglecting all higher order perturbations yields

$$\rho_0 u_0\widetilde{u}\frac{dE}{dx} + \rho_0\widetilde{v}E\frac{du_0}{dy} \tag{C.7}$$

The pressure term can be expanded as

$$\frac{\partial p}{\partial x} = \frac{\partial}{\partial x}(p_\infty + E\widetilde{p}) = \widetilde{p}\frac{dE}{dx} \tag{C.8}$$

In the first term on the right hand side of equation (C.6) λ the bulk viscosity will be modeled by a stokes hypothesis: $\lambda = -\frac{2}{3}\mu$, see white [12] for details.

With this assumption the first term on the right hand side becomes:

$$2\frac{\partial}{\partial x}\left(\mu\left(-\frac{1}{3}\left(\frac{\partial u}{\partial x}+\frac{\partial v}{\partial y}\right)+\frac{\partial u}{\partial x}\right)\right) = 2\frac{\partial}{\partial x}\left(\mu\left(\frac{2}{3}\frac{\partial u}{\partial x}-\frac{1}{3}\frac{\partial v}{\partial y}\right)\right)$$

Expanding this term in its mean and perturbation the following is achieved

$$\begin{gathered} 2\tfrac{\partial \mu}{\partial x}\left(\tfrac{2}{3}\tfrac{\partial u}{\partial x}-\tfrac{1}{3}\tfrac{\partial v}{\partial y}\right)+2\mu\left(\tfrac{2}{3}\tfrac{\partial^2 u}{\partial x^2}-\tfrac{1}{3}\tfrac{\partial^2 v}{\partial x \partial y}\right)=.. \\ 2E\widetilde{\mu}\left(\tfrac{2}{3}E\tfrac{d\widetilde{u}}{dy}-\tfrac{1}{3}E\tfrac{d\widetilde{v}}{dy}\right)+2\left(\mu_0+E\widetilde{\mu}\right)\left(\tfrac{2}{3}\widetilde{u}\tfrac{d^2E}{dx^2}-\tfrac{1}{3}\tfrac{dE}{dx}\tfrac{d\widetilde{v}}{dy}\right) \end{gathered}$$

Neglecting all terms with higher order perturbations yields the following

$$\frac{4}{3}\mu_0\widetilde{u}\frac{d^2E}{dx^2}-\frac{2}{3}\mu_0\frac{dE}{dx}\frac{d\widetilde{v}}{dy} \tag{C.9}$$

The second term on the right hand side can be expanded in the same manner:

$$\frac{\partial}{\partial y}\left(\mu\left(\frac{\partial v}{\partial x}+\frac{\partial u}{\partial y}\right)\right) = \frac{\partial}{\partial y}\left(\left(\mu_0+E\widetilde{\mu}\right)\left(\widetilde{v}\frac{\partial E}{\partial x}+\frac{\partial u_0}{\partial y}+E\frac{\partial \widetilde{u}}{\partial y}\right)\right)$$

Expanding to individual terms and neglecting again the higher order perturbations yields the following term

$$\frac{\partial}{\partial y}\left(\mu_0\widetilde{v}\frac{\partial E}{\partial x}+\mu_0\frac{\partial u_0}{\partial y}+\mu_0E\frac{\partial \widetilde{u}}{\partial y}+E\widetilde{\mu}\frac{\partial u_0}{\partial y}\right)$$

This term can be rewritten into it's final form as

$$\frac{\partial}{\partial y}\left[\mu_0\left(E\frac{\partial \widetilde{u}}{\partial y}+\widetilde{v}\frac{\partial E}{\partial x}\right)\right]+E\frac{\partial}{\partial y}\left(\widetilde{\mu}\frac{\partial u_0}{\partial y}\right)+\frac{\partial}{\partial y}\left(\mu_0\frac{\partial u_0}{\partial y}\right) \tag{C.10}$$

Combining all the terms of the x momentum equation and dividing by E yields:

$$\begin{gathered}\rho_0 u_0 \widetilde{u}\frac{\frac{dE}{dx}}{E} + \rho_0 \widetilde{v}\frac{du_0}{dy} + \widetilde{p}\frac{\frac{dE}{dx}}{E} = \ldots \\ \frac{\partial}{\partial y}\left[\mu_0\left(\frac{\partial \widetilde{u}}{\partial y} + \widetilde{v}\frac{\frac{\partial E}{\partial x}}{E}\right)\right] + \frac{\partial}{\partial y}\left(\widetilde{\mu}\frac{\partial u_0}{\partial y}\right) - \frac{2}{3}\mu_0\left(\frac{\frac{dE}{dx}}{E}\frac{d\widetilde{v}}{dy} - 2\widetilde{u}\frac{\frac{d^2E}{dx^2}}{E}\right) + \frac{1}{E}\frac{\partial}{\partial y}\left(\mu_0\frac{\partial u_0}{\partial y}\right)\end{gathered} \tag{C.11}$$

C.3 Momentum equation, y

The y momentum equation in a 2D flow field as given by White [12] can be seen in equation

$$\nabla \cdot (\rho u \mathbf{V}) + \frac{\partial p}{\partial x} = \frac{\partial}{\partial x}\left(\mu\left(\frac{\partial v}{\partial x} + \frac{\partial u}{\partial y}\right)\right) + \frac{\partial}{\partial y}\left(\lambda \nabla \cdot \mathbf{V} + 2\mu\frac{\partial v}{\partial y}\right) \tag{C.12}$$

Each term will now be treated individually.

The first term on the left hand side of equation (C.12) can be expanded in the following manner:

$$\nabla \cdot (\rho u \mathbf{V}) = \rho u\frac{\partial v}{\partial x} + \rho v\frac{\partial v}{\partial y} = (\rho_0 + E\widetilde{\rho})(u_0 + E\widetilde{u})\widetilde{v}\frac{\partial E}{\partial x} + (\rho_0 + E\widetilde{\rho})E\widetilde{v}E\frac{\partial \widetilde{v}}{\partial y}$$

Expanding and neglecting all second order perturbations yields the final form of this term, see

$$\rho_0 u_0 \widetilde{v}\frac{\partial E}{\partial x} \tag{C.13}$$

The pressure term can be expanded as shown in equation (C.14)

$$\frac{\partial p}{\partial y} = \frac{\partial (p_\infty + E\widetilde{p})}{\partial y} = E\frac{\partial \widetilde{p}}{\partial y} \tag{C.14}$$

The first term on the right hand side of equation (C.12) can be expanded in the following manner:

$$\frac{\partial}{\partial x}\left(\mu\left(\frac{\partial v}{\partial x}+\frac{\partial u}{\partial y}\right)\right)=\frac{\partial}{\partial x}\left((\mu_0+E\widetilde{\mu})\left(\widetilde{v}\frac{\partial E}{\partial x}+\frac{\partial u_0}{\partial y}+E\frac{\partial \widetilde{u}}{\partial y}\right)\right)$$

Expanding to individual terms and neglecting higher order perturbations yields

$$\frac{\partial}{\partial x}\left(\widetilde{v}\mu_0\frac{\partial E}{\partial x}+\mu_0\frac{\partial u_0}{\partial y}+E\mu_0\frac{\partial \widetilde{u}}{\partial y}+E\widetilde{\mu}\frac{\partial u_0}{\partial y}\right)$$

Taking the x derivative of all the terms yields the final expression for this term, see equation (C.15).

$$\widetilde{v}\mu_0\frac{\partial^2 E}{\partial x^2}++\mu_0\frac{dE}{dx}\frac{\partial \widetilde{u}}{\partial y}+\widetilde{\mu}\frac{dE}{dx}\frac{\partial u_0}{\partial y} \tag{C.15}$$

With the stokes hypothesis the second term on the right hand side in equation (C.12) can be expanded in the same manner as is done in the x momentum equation.

$$\frac{\partial}{\partial y}\left(\lambda\nabla\cdot\mathbf{V}+2\mu\frac{\partial v}{\partial y}\right)=\frac{\partial}{\partial y}\left(-\frac{2}{3}\mu\left(\frac{\partial u}{\partial x}+\frac{\partial v}{\partial y}\right)+2\mu\frac{\partial v}{\partial y}\right)=2\frac{\partial}{\partial y}\left(\mu\left(\frac{2}{3}\frac{\partial v}{\partial y}-\frac{1}{3}\frac{\partial u}{\partial x}\right)\right)$$

Expanding this term into a mean and perturbation term yields

$$\begin{array}{l}2\frac{\partial}{\partial y}\left(\mu_0\left(\frac{2}{3}\frac{\partial v}{\partial y}-\frac{1}{3}\frac{\partial u}{\partial x}\right)\right)+2E\frac{\partial}{\partial y}\left(\widetilde{\mu}\left(\frac{2}{3}\frac{\partial v}{\partial y}-\frac{1}{3}\frac{\partial u}{\partial x}\right)\right)=\ldots\\ \frac{4}{3}\frac{\partial}{\partial y}\left(\mu_0\left(E\frac{\partial \widetilde{v}}{\partial y}-\frac{1}{2}\widetilde{u}\frac{\partial E}{\partial x}\right)\right)+\frac{4}{3}E\frac{\partial}{\partial y}\left(\widetilde{\mu}\left(E\frac{\partial \widetilde{v}}{\partial y}-\frac{1}{2}\widetilde{u}\frac{\partial E}{\partial x}\right)\right)\end{array}$$

Neglecting the second term due to second order perturbations yields the final form of this term, see equation (C.16).

$$\frac{4}{3}\frac{\partial}{\partial y}\left[\mu_0\left(E\frac{\partial \widetilde{v}}{\partial y}-\frac{1}{2}\widetilde{u}\frac{\partial E}{\partial x}\right)\right] \tag{C.16}$$

Combining all terms and dividing by E gives the final form of the y momentum equation,

see equation (C.17).

$$\rho_0 u_0 \widetilde{v} \frac{\frac{\partial E}{\partial x}}{E} + E\frac{\partial \widetilde{p}}{\partial y} = \frac{4}{3}\frac{\partial}{\partial y}\left[\mu_0\left(\frac{\partial \widetilde{v}}{\partial y} - \frac{1}{2}\widetilde{u}\frac{\frac{\partial E}{\partial x}}{E}\right)\right] + \widetilde{\mu}\frac{\frac{\partial E}{\partial x}}{E}\frac{\partial u_0}{\partial y} + \mu_0\left(\mu_0\frac{\frac{\partial E}{\partial x}}{E}\frac{\partial \widetilde{u}}{\partial y} + \widetilde{v}\frac{\frac{\partial^2 E}{\partial x^2}}{E}\right) \quad \text{(C.17)}$$

C.4 Energy equation

The energy equation with viscous terms as given by White [12] can be seen in equation (C.18).

$$\rho\frac{D\left(C_pT + \frac{V^2}{2}\right)}{Dt} = \frac{\partial}{\partial x}\left(k\frac{\partial T}{\partial x}\right) + \frac{\partial}{\partial y}\left(k\frac{\partial T}{\partial y}\right) + \frac{\partial\left(u\tau_{xx}\right)}{\partial x} + \frac{\partial\left(u\tau_{yx}\right)}{\partial y} + \frac{\partial\left(v\tau_{xy}\right)}{\partial x} + \frac{\partial\left(v\tau_{yy}\right)}{\partial y} \quad \text{(C.18)}$$

In equation (C.18) the shear terms are given by: $\tau_{xx} = \lambda\left(\nabla\cdot\mathbf{V}\right) + 2\mu\frac{\partial u}{\partial x}$, $\tau_{yx} = \tau_{xy} = \mu\left(\frac{\partial v}{\partial x} + \frac{\partial u}{\partial y}\right)$ and $\tau_{yy} = \lambda\left(\nabla\cdot\mathbf{V}\right) + 2\mu\frac{\partial v}{\partial y}$

Each term will now be expanded individually.

The first term on the left hand side, in this case of steady flow can be expanded as seen in equation (C.19).

$$\rho\frac{D\left(C_pT + \frac{V^2}{2}\right)}{Dt} = \rho u\frac{\partial\left(C_pT + \frac{V^2}{2}\right)}{\partial x} + \rho v\frac{\partial\left(C_pT + \frac{V^2}{2}\right)}{\partial y} \quad \text{(C.19)}$$

The term $\left(C_pT + \frac{V^2}{2}\right)$ can be expanded as:

$$C_pT + \frac{V^2}{2} = C_p\left(T_0 + E\widetilde{T}\right) + \frac{u_0^2 + 2Eu_o\widetilde{u}}{2} = C_pT_0 + \frac{u_0^2}{2} + C_p\widetilde{T}E + Eu_o\widetilde{u}$$

With $C_pT_0 + \frac{u_0^2}{2}$ denoting the mean enthalpy H_0 and $C_p\widetilde{T} + u_o\widetilde{u}$ denoting the perturbation enthalpy $\widetilde{H}$.

Expanding the first term on the right hand side of equation (C.19) now gives :

$$\rho u \frac{\partial\left(C_p T + \frac{V^2}{2}\right)}{\partial x} = \left(\rho_0 + E\rho_0\right)\left(u_0 + E\widetilde{u}\right) \frac{\partial\left(C_p T_0 + \frac{u_0^2}{2} + C_p \widetilde{T} E + E u_0 \widetilde{u}\right)}{\partial x}$$

Working this the out and neglecting higher order perturbations yields the first term of the energy equation

$$\rho_0 u_0 \widetilde{H} \frac{dE}{dx} \tag{C.20}$$

Expanding the second term on the right hand side of equation (C.19) yields:

$$\rho v \frac{\partial\left(C_p T + \frac{V^2}{2}\right)}{\partial y} = \left(\rho_0 + E\rho_0\right)\left(E\widetilde{v}\right) \frac{\partial\left(C_p T_0 + \frac{u_0^2}{2} + C_p \widetilde{T} E + E u_0 \widetilde{u}\right)}{\partial y}$$

Neglecting again the second order terms and putting all terms together yields the second term of the energy equation,

$$\rho_0 \widetilde{v} E \frac{dH_0}{dy} \tag{C.21}$$

For the right hand side of equation ((C.18)) the thermal conductivity will be approximated by $k = \mu C_p$. The proper correlation taken from White [12] is $k = 1.45\mu C_p$, but the constant will be omitted for simplicity, and any constant that is missing can be reintroduced as constants of integration. Now the first term on the right hand side can be expanded as:

$$\frac{\partial}{\partial x}\left(k \frac{\partial T}{\partial x}\right) = \left(\mu_0 + E\widetilde{\mu}\right) C_p \widetilde{T} \frac{d^2 E}{dx^2} \approx \mu_0 C_p \widetilde{T} \frac{d^2 E}{dx^2}$$

The second term on the right hand side of equation (C.18) can be expanded in the following manner:

$$\frac{\partial}{\partial y}\left(k \frac{\partial T}{\partial y}\right) = \frac{\partial}{\partial y}\left(C_p\left(\mu_0 + E\widetilde{\mu}\right) \frac{d\left(T_0 + E\widetilde{T}\right)}{dy}\right) = \frac{\partial}{\partial y}\left(C_p \mu_0 \frac{dT_0}{dy} + C_p \mu_0 E \frac{d\widetilde{T}}{dy} + C_p E \widetilde{\mu} \frac{dT_0}{dy}\right)$$

The next step is to expand all the shear terms that are present in the the energy equation:

$$\frac{\partial\left(u\tau_{xx}\right)}{\partial x}=\frac{\partial\left(u\left(-\frac{2}{3}\mu\left(\frac{\partial u}{\partial x}+\frac{\partial v}{\partial y}\right)+2\mu\frac{\partial u}{\partial x}\right)\right)}{\partial x}=2\frac{\partial}{\partial x}\left(u\mu\left(\frac{2}{3}\frac{\partial u}{\partial x}-\frac{1}{3}\frac{\partial v}{\partial y}\right)\right)$$

Expanding this term and neglecting higher order perturbations yields the final form of this term

$$\frac{4}{3}u_0\mu_0\widetilde{u}\frac{d^2E}{dx^2}-\frac{2}{3}u_0\mu_0\frac{dE}{dx}\frac{d\widetilde{v}}{dy} \tag{C.22}$$

The second shear term can be expanded as:

$$\frac{\partial\left(u\tau_{yx}\right)}{\partial y}=\frac{\partial}{\partial y}\left(u\mu\left(\frac{\partial v}{\partial x}+\frac{\partial u}{\partial y}\right)\right)$$

Expanding and neglecting higher order perturbations yields the final form of this shear term, see equation (C.23).

$$\frac{d}{dy}\left(\mu_0u_0\widetilde{v}\frac{dE}{dx}+\mu_0u_0\frac{du_0}{dy}+\mu_0u_0E\frac{d\widetilde{u}}{dy}+u_0\widetilde{\mu}E\frac{du_0}{dy}+\widetilde{u}\mu_0E\frac{du_0}{dy}\right) \tag{C.23}$$

Expanding the 3th shear term yields:

$$\frac{\partial\left(v\tau_{xy}\right)}{\partial x}=\frac{\partial}{\partial x}\left(v\mu\left(\frac{\partial v}{\partial x}+\frac{\partial u}{\partial y}\right)\right)$$

Expanding this term and neglecting second order perturbations yield the final form of the 3th shear term:

$$\widetilde{v}\mu_0\frac{dE}{dx}\frac{du_0}{dy} \tag{C.24}$$

Taking the 4th and final shear term and expanding this term yields:

$$\frac{\partial\left(v\tau_{yy}\right)}{\partial y}=\frac{\partial}{\partial y}\left(v\left(-\frac{2}{3}\mu\left(\frac{\partial u}{\partial x}+\frac{\partial v}{\partial y}\right)+2\mu\frac{\partial v}{\partial y}\right)\right)=2\frac{\partial}{\partial y}\left(v\mu\left(-\frac{1}{3}\frac{\partial u}{\partial x}+\frac{2}{3}\frac{\partial v}{\partial y}\right)\right)$$

Expanding this term and neglecting higher order terms yield the final form of this 4th shear term, see equation (C.25).

$$-\frac{2}{3}E\frac{d}{dy}\left(\widetilde{v}\mu_0\frac{du_0}{dy}\right) \tag{C.25}$$

Collecting terms and dividing by E will yield the final version of the energy equation, see (C.26).

$$\begin{aligned}\rho_0 u_0\widetilde{H}\tfrac{\frac{dE}{dx}}{E}+\rho_0\widetilde{v}\tfrac{dH_0}{dy}=\tfrac{d}{dy}\left[\mu_0\left(\tfrac{d\widetilde{H}}{dy}+\tfrac{\frac{dE}{dx}}{E}u_0\widetilde{v}\right)+\widetilde{\mu}\tfrac{dH_0}{dy}\right]+\tfrac{1}{E}\tfrac{d}{dy}\left(\mu_0\tfrac{dH_0}{dy}\right)+\tfrac{\frac{dE}{dx}}{E}\mu_0\widetilde{v}\tfrac{du_0}{dy}\\ -\tfrac{2}{3}\tfrac{d}{dy}\left(\widetilde{v}\mu_0\tfrac{du_0}{dy}\right)+\mu_0\tfrac{\frac{dE}{dx}}{E}\left(\widetilde{H}+\tfrac{1}{3}u_0\widetilde{u}-\tfrac{2}{3}\tfrac{\frac{dE}{dx}}{\frac{d^2E}{dx^2}}u_0\tfrac{d\widetilde{v}}{dy}\right)\end{aligned} \tag{C.26}$$

C.5 Perfect gas law

To complete the equations, and to get a solvable system, the energy equation is needed. In this section the perfect gas law will be expanded as in the foregoing manner.

The perfect gas law as can be found in any normal text book, for example Anderson [26] can be seen in equation (C.27).

$$p=\rho RT \tag{C.27}$$

In equation C.27 p the is pressure, ρ the density R the specific gas constant and T the temperature. Expanding equation (C.27) in the same manner as was done in the forgoing sections, and dividing by the static pressure yields:

$$1+E\frac{\widetilde{p}}{p_\infty}=R\frac{\rho_0T_0}{p_\infty}+ER\widetilde{\rho}\frac{T_0}{p_\infty}+ER\widetilde{T}\frac{\rho_0}{p_\infty}$$

Assuming that equation (C.27) is also valid for only the mean parameters we can say : $\frac{\rho_0T_0}{p_\infty}=\frac{1}{R}$, $\frac{T_0}{p_\infty}=\frac{1}{R\rho_0}$ and $\frac{\rho_0}{p_\infty}=\frac{1}{RT_0}$.

Combining the foregoing formulations the final form of the perfect gas law can be described as:

$$\frac{\widetilde{p}}{p_\infty} = \frac{\widetilde{\rho}}{\rho_0} + \frac{\widetilde{T}}{T_0} \tag{C.28}$$

The combination of equations (C.4),(C.6),(C.17), (C.26) and (C.28) yields a set of equations that can be solved.

C.6 Boundary conditions

With the derivation of the differential equations, the boundary conditions need to be complemented, to have a solvable set of equations. At the edge of the boundary layer the same treatment as Inger will be used, 2 boundary conditions will be applied: Perturbations become adiabatic and the pressure field involves simple Mach waves for exponential-decaying signals. See equation (C.29) for the formulations.

$$\begin{gathered} \widetilde{H}(\delta) = 0 \\ \frac{d\widetilde{P}}{dy}(\delta) = -i\left(Me^2 - 1\right)^{1/2} \widetilde{P}(\delta) \end{gathered} \tag{C.29}$$

For the wall three boundary conditions will be applied: $v = 0$, no flow through the surface, no slip condition $u(y_w) = 0$ and a fixed wall temperature for fixed heat flux condition, $T(y_w) = C$ or $\mu\frac{dT}{dy}(y_w) = C$. Making the assumption that the wall profiles are small small enough so that one can expand the no-slip condition as a first order Taylor series:

$$u(y_w) = u_0(0) + E\widetilde{u}(0) + y_w\frac{du_0}{dy}(0) + Ey_w\frac{d\widetilde{u}}{dy}(0)$$

Making the assumption that $u(y_w) \approx u_0(0)$ and presuming that the perturbation derivative vanishes on the wall, or $(\frac{d\widetilde{u}}{dy}(0) = 0)$. The final boundary condition can be derived as,

$$\widetilde{u}(0) = -\frac{y_w}{E}\frac{du_0}{dy}(0) = -\frac{y_w}{E}\frac{\tau_{n_0}}{\mu_{w_0}} \tag{C.30}$$

In equation (C.30) y_w is the wall shape, τ_{n_0}, is the wall shear, and $\mu_{w_0}$is the viscosity based on wall temperature.

For the condition of constant wall temperature the assumption of a small wall shape is made again. Now the wall temperature can be expanded as a first order Taylor series:

$$T\left(y_w\right) = T_0\left(0\right) + E\widetilde{T}\left(0\right) + y_w\frac{dT_0}{dy}\left(0\right) + Ey_w\frac{d\widetilde{T}}{dy}\left(0\right)$$

With the assumption that the derivative of the perturbation vanishes against the wall, $T\left(y_w\right) \approx T_0\left(0\right)$. The boundary condition of a constant temperature wall can be set-up as

$$\widetilde{T}\left(0\right) = -\frac{y_w}{E}\frac{dT_0}{dy}\left(0\right)$$

$$\widetilde{H}\left(0\right) = -\frac{y_w}{E}\frac{dH_0}{dy}\left(0\right) \tag{C.31}$$

For the condition where the heat flux is fixed we have the following:

$$\mu\frac{dT}{dy} = c$$

Expanding this and subtracting main values yields.

$$\mu_0\frac{d\widetilde{H}}{dy} + \widetilde{\mu}\frac{dH_0}{dy} \simeq 0 \tag{C.32}$$

With the present formulation the equations can be solved by means of numerical analysis. However for a better understanding of the physics behind the equations a number of simplifications will be made to the differential equations, which will make them solvable with analytical techniques.

C.7 Viscous solution

To simplify the equations a number of assumptions are necessary. The same assumptions as Inger [14] has made.

- Viscous dissipation heating effects on both the mean and perturbation terms in the flows are neglected.
- Viscosity and heat conduction effects on the perturbation field are restricted to a thin “frictional sublayer" whose thickness δ_f is small compared to the boundary layer thickness
- In the case of turbulent flow, this frictional sublayer lies within the so-called laminar sublayer such that the mean velocity and temperature profiles are approximately linear.
- The frictional sublayer is small compared to the disturbance wavelength such that $(\alpha\delta_f)^2 \ll 1$.
- The density and viscosity perturbations are neglected
- $\rho_0\mu_0 \simeq$ constant

With the following compressibility transforms the governing equations can be greatly simplified as,

$$\begin{aligned} Y &= \int_0^y \left(\frac{\rho_0}{\rho_{0_w}}\right) dy \\ \widetilde{V}^* &= \frac{\rho_0 \tilde{V}}{\rho_{0_w}} \end{aligned} \tag{C.33}$$

With these compressibility transforms the governing equations can be reduces to the following,

$$\frac{\frac{dE}{dx}}{E}\widetilde{u} + \frac{d\widetilde{V}^*}{dY} \simeq 0 \tag{C.34}$$

$$\frac{\frac{dE}{dx}}{E}u_0\widetilde{u} + \left(\frac{dq_0}{dY}\right)\widetilde{V}^* + \frac{\frac{dE}{dx}}{E}\left(\frac{H_0}{h_{0_w}}\right)\frac{\widetilde{P}}{\rho_{0_w}} \simeq \nu_{0_w}\frac{d^2\widetilde{u}}{dY^2} \tag{C.35}$$

$$\frac{\frac{dE}{dx}}{E} u_0 \widetilde{H} + \left(\frac{d\widetilde{H}_0}{dY} \right) \widetilde{V}^* \simeq \nu_{0_w} \frac{d^2 \widetilde{H}}{dY^2} \tag{C.36}$$

Combining equations (C.34) and (C.35), yields a single equation in $\widetilde{V}^*$,

$$\left\{ \nu_{0_w} \frac{d^2}{dY^2} - \frac{\frac{dE}{dx}}{E} \frac{\tau_{N_0}}{\mu_{w_0}} Y \right\} \frac{d^2 \widetilde{V}^*}{dY^2} \simeq - \left(\frac{\frac{dE}{dx}}{E} \right)^2 \frac{\widetilde{P}\,(0)}{\rho_{0_w}} \left[\frac{dH_0/dY\,(0)}{h_{0_w}} \right] \tag{C.37}$$

Equation (C.37) is a non-homogeneous Orr-Sommerfield equation. With equation (C.37) in combination with the boundary conditions ((C.30) and (C.31) or (C.32)) the basic systems of equations to solve is determined. The perturbation terms that have to be taken into account are: $\frac{\frac{dE}{dx}}{E}$ and $-\frac{y_w}{E}$. In the next section equivalences will be made to Ingers results so that Ingers final results are usable.

C.8 Equivalent frequency and amplitude

In Ingers original paper the terms $\frac{\frac{dE}{dx}}{E}$ and $-\frac{y_w}{E}$ are expanded in the following matter

$$\frac{\frac{dE}{dx}}{E} = i\alpha \qquad -\frac{y_w}{E} = i\epsilon \tag{C.38}$$

With E defined by equation (C.3) $\frac{\frac{dE}{dx}}{E}$ becomes:

$$\frac{\frac{dE}{dx}}{E} = ik\omega_0 \frac{e^{i\omega_0 x}}{e^{i\omega_0 x}} = i\omega_0$$

Now we define an equivalent amplitude such that this derivation is compatible with Inger's, with

$$\alpha_e = \omega_0 \tag{C.39}$$

For $-\frac{y_w}{E}$ we obtain

$$-\frac{y_w}{E} = -\frac{\sum_{k=1}^{N-1} a_k cos(ik\omega_o x) + b_k sin\left(ik\omega_o x\right)}{e^{i\omega_o x}}$$

which after a number of steps can be simplified to :

$$-\frac{y_w}{E} = -\sum_{k=1}^{N-1} e^{i\omega_o x}\left(a_k cosh\left(k\omega_o x\right) + ib_b sinh\left(k\omega_o x\right)\right)$$

Comparing this relation with C.38 we can define the equivalent amplitude as:

$$\epsilon_e = -\frac{1}{i}\sum_{k=1}^{N-1} e^{i\omega_o x}\left(a_k cosh\left(k\omega_o x\right) + ib_k sinh\left(k\omega_o x\right)\right) \tag{C.40}$$

From this point onwards the derivation of Inger can be followed, such that in the end the change in wall shear and heat transfer can be modeled as

$$\triangle\widetilde{\tau} \simeq 1.37\tau_{N_0}\frac{\epsilon_e\Omega_p}{\delta_f}e^{\frac{4}{3}\pi i}\left[1 + 1.62e^{\pi i/3}\left(\frac{\delta_f}{h_{w_0}}\right)x\frac{dH_0}{dY}\left(0\right)\right] \tag{C.41}$$

$$\triangle\tilde{\dot{q}}_w \simeq 0.443\mu_{w_0}\frac{dH_0}{dY}\left(0\right)\frac{\epsilon_e}{\delta_f}\Omega_p e^{\frac{4}{3}\pi i}\left[1 + 5.4\left(\frac{\delta_f}{h_{w_0}}\right)\frac{dH_0}{dY}e^{13\pi//30}\right] \tag{C.42}$$

Table C.1 gives a description of the variables included in equation C.41 and C.42.

Table C.1: Variables equations C.41 and C.42

Variables	Meaning	Parameter group	Reference
$\triangle\widetilde{\tau}$	Change in wall shear		
$\triangle\tilde{\dot{q}}_w$	Change in heat transfer		
τ_{N_0}	Reference wall shear		
ϵ_e	Equivalent amplitude		
α_e	Equivalent frequency		
Ω_p	Stokes number	$\Omega_p = \frac{\alpha_e \delta_f^2 \widetilde{P}(0)}{\epsilon_e \tau_{N_0}}$	
δ_f	Size frictional sublayer	$\delta_f = \left(\frac{\mu_0^2}{\rho_0 \tau_{N_0} \alpha_e}\right)$	
h_{w_o}	wall enthalpy		
$\frac{dH_0}{dY}(0)$	change in total wall enthalpy		
μ_{w_0}	Wall viscosity		
$\widetilde{P}(0)$	Pressure fluctuations	$\frac{p'}{\gamma p_\infty M^2} = \frac{\epsilon\alpha cos(x-\beta y)}{\beta}$	[13]
β	compressibility correction	$\beta = \sqrt{M^2 - 1}$	

C.9 Testing and Conclusions

For testing of the current equations, a forward facing step geometry was chosen. Observing equation C.41 and C.42 2 groups of variables are responsible for the geometrical variations, $\frac{\epsilon_e \Omega_p}{\delta_f}$ and δ_f. Both equations C.41 and C.42 show these groups, and therefore either one can be used to display the behavior. This author has chosen for the wall shear (equation C.41). Three runs where made, one with constant step height, and varying length, one with constant length and varying height, and one with varying height, at a constant L/R ratio, where R is the height of the step.

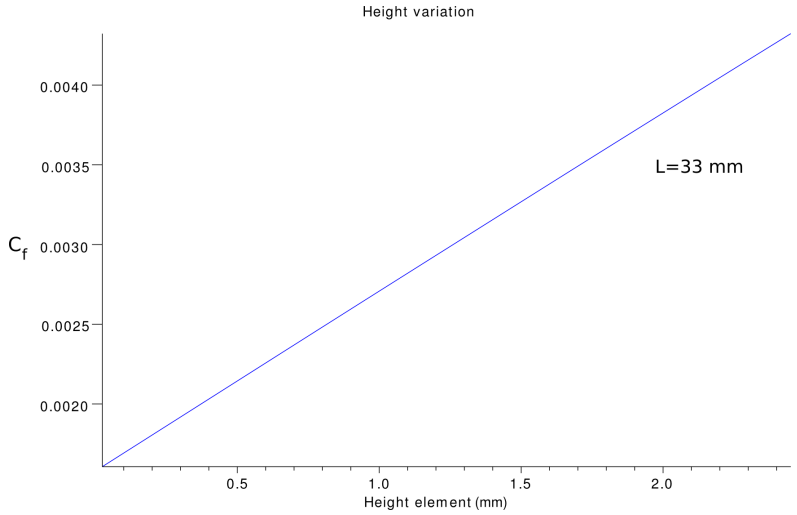

Figure C.1: Height variation at constant length

Fig. C.1 shows the variation in friction coefficient at a constant element length. Noteworthy is the linear behavior, that was also observed with the CFD results, Figure 7.2. The friction coefficients presented here are approximately half of the friction coefficients obtained from CFD.

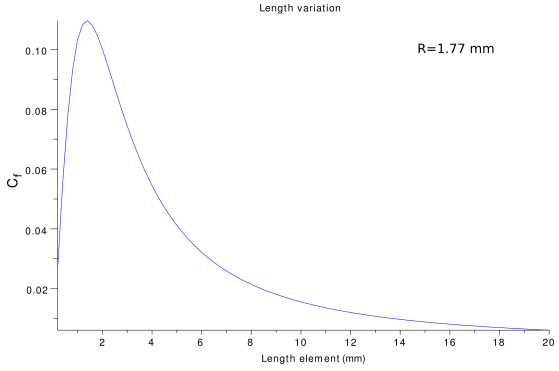

Figure C.2: Length variation at constant height

Fig. C.2 shows the friction coefficients at constant height. Interestingly for small lengths there is an increase of friction coefficient, but for larger heights a decrease can again be noted. This decrease is due to the large influence of the spatial frequency on the results.

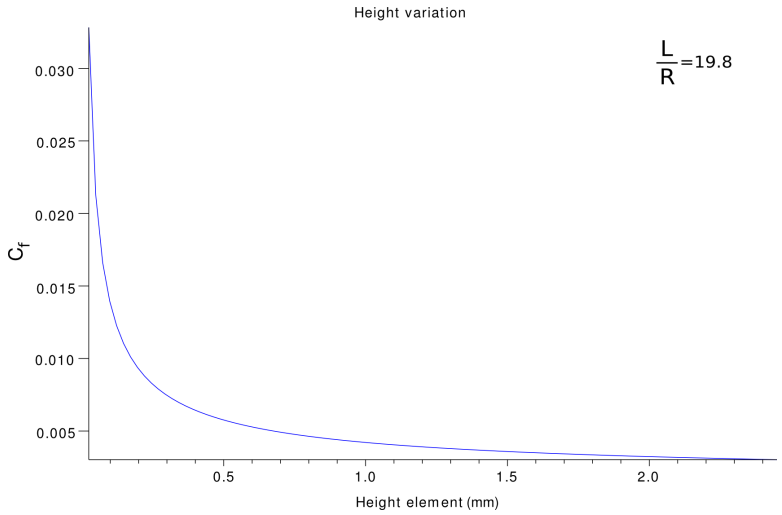

Figure C.3: Height variation at constant $\frac{L}{R}$

Fig. C.3 shows the friction coefficient at constant $\frac{L}{R}$. An asymptote for zero roughness height can be seen. Furthermore again the unphysical behavior of decrease friction for increasing roughness height.

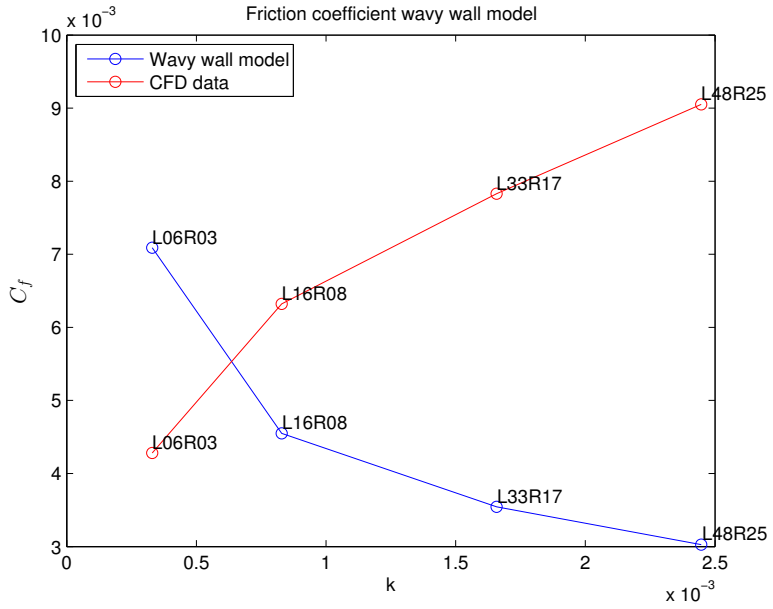

Figure C.4: Comparison wavy wall model with analytical results

Figure C.4 shows a comparison of the CFD data with the 4 height variation geometries. As can be seen the model shows the inverse behavior of the data. Noteworthy is that the inverse of the model shows good comparison with the data. The high frequency geometries have not been shown in the last figure. In figure C.2 the same roughness height as these geometries has been used. It can be noted that the model gives a friction coefficient in the neighborhood of 0.02 to 0.04 while the actual friction coefficients are in the order of 0.005.

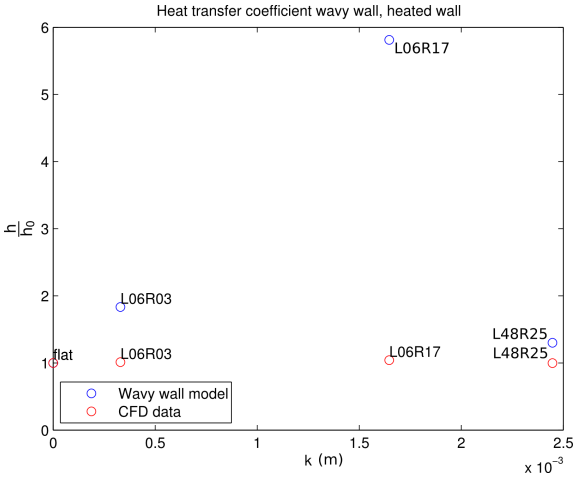

Figure C.5: Heat transfer, heated wall

Figure C.5 shows the heat transfer for the heated wall of 412.5 Kelvin. The heat transfer coefficients have been normalized with the flat plate heat transfer. As can be seen the model heat transfers overestimate the data from the CFD. The L06R03 and L48R25 geometry have the smallest difference compared to the L06R17 geometry. As with the friction coefficient a large overestimation could be seen.

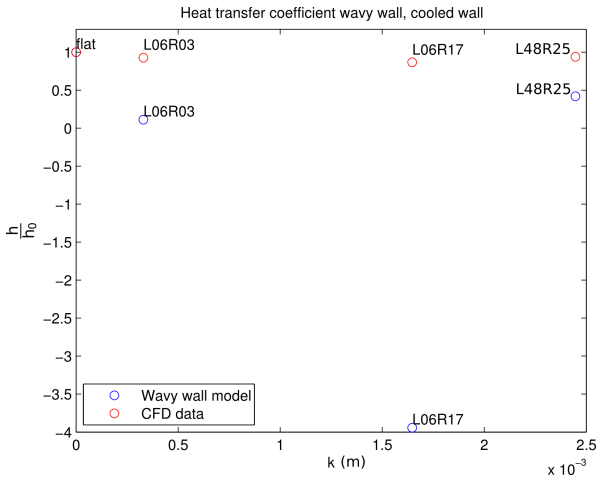

Figure C.6: Heat transfer, cooled wall

Figure C.6 shows the heat transfer of the cooled case. Again large differences are visible between the data and the model predictions. The L06R17 geometry shows the biggest difference between the model predictions and the data. Noteworthy is that in the data the L06R17 has the smallest heat transfer followed by the L06R03 and the L48R25 geometry. The model does produce the order, from smallest to largest heat transfer.

From figures C.2 and C.3, it can be noted that unphysical behavior appears when the length of the elements is varied. Both show a decrease in friction coefficient with increase in roughness height. Both are due to the large influence of the spatial frequency on the solutions.
For the variation in height at constant length, good results where obtained. The physical behavior of increasing friction with roughness height was obtained. Also linear behavior was obtained, the same as was shown by the CFD.

Therefore we can conclude that using Fourier series does yield an increase in modeling capabilities. The model presented here though does still have a number of shortcomings that need to be addressed, the influence of the spatial frequency, and the results need to be calibrated with experimental results to yield proper results.

Appendix D

CFX Run setting

The current settings have been used for all adiabatic runs with the SST Reynolds stress model.

For the runs done with the BSL model the Option parameter under Turbulence model was changes to BSL Reynolds stress.

For the runs done with heated and cooled wall the option heat transfer under the location 'platte' has been changed from adiabatic to : Fixed Temperature = 412.5 [K] Option = Fixed Temperature, or a temperature of 137.5 K for the cooled simulations.

This run of the CFX-13.0 Solver started at 10:30:00 on 05 Jul 2013 by

user hvanpelt on TUD103665 (intel_xeon64.sse2_winnt) using the command:

"C:\Program Files\ANSYS Inc\v130\CFX\bin\perllib\cfx5solve.pl"

-stdout-comms -batch -ccl -

Setting up CFX Solver run ...

+————————————————————————————+

| |

| CFX Command Language for Run |

| |

+——————————————————————————+

LIBRARY:

MATERIAL: Air Ideal Gas

Material Description = Air Ideal Gas (constant Cp)

Material Group = Air Data,Calorically Perfect Ideal Gases

Option = Pure Substance

Thermodynamic State = Gas

PROPERTIES:

Option = General Material

EQUATION OF STATE:

Molar Mass = 28.96 [kg kmol^-1]

Option = Ideal Gas

END

SPECIFIC HEAT CAPACITY:

Option = Value

Specific Heat Capacity = 1.0044E+03 [J kg^-1 K^-1]

Specific Heat Type = Constant Pressure

END

REFERENCE STATE:

Option = Specified Point

Reference Pressure = 1 [atm]

Reference Specific Enthalpy = 0. [J/kg]

Reference Specific Entropy = 0. [J/kg/K]

Reference Temperature = 25 [C]

END

DYNAMIC VISCOSITY:

Option = Sutherlands Formula

Reference Temperature = 0 [C]

Reference Viscosity = 1.716e-5 [Pa s]

Sutherlands Constant = 111 [K]

Temperature Exponent = 0.666

END

THERMAL CONDUCTIVITY:

Option = Sutherlands Formula

Reference Temperature = 0 [C]

Reference Thermal Conductivity = 0.0241 [W m^-1 K^-1]

Sutherlands Constant = 194 [K]

Temperature Exponent = 0.81

END

ABSORPTION COEFFICIENT:

Absorption Coefficient = 0.01 [m^-1]

Option = Value

END

SCATTERING COEFFICIENT:

Option = Value

Scattering Coefficient = 0.0 [m^-1]

END

REFRACTIVE INDEX:

Option = Value

Refractive Index = 1.0 [m m^-1]

END

END

END

END

END

FLOW: Flow Analysis 1

SOLUTION UNITS:

Angle Units = [rad]

Length Units = [m]

Mass Units = [kg]

Solid Angle Units = [sr]

Temperature Units = [K]

Time Units = [s]

END

ANALYSIS TYPE:

Option = Steady State

EXTERNAL SOLVER COUPLING:

Option = None

END

END

DOMAIN: Default Domain

Coord Frame = Coord 0

Domain Type = Fluid

Location = FLUID

BOUNDARY: einlaufstrecke

Boundary Type = WALL

Location = EINLAUFSTRECKS

BOUNDARY CONDITIONS:

HEAT TRANSFER:

Option = Adiabatic

END

MASS AND MOMENTUM:

Option = Free Slip Wall

END

END

END

BOUNDARY: inlet

Boundary Type = INLET

Location = INLET

BOUNDARY CONDITIONS:

FLOW DIRECTION:

Option = Normal to Boundary Condition

END

FLOW REGIME:

Option = Subsonic

END

HEAT TRANSFER:

Option = Total Temperature

Total Temperature = 290 [K]

END

MASS AND MOMENTUM:

Option = Total Pressure

Relative Pressure = 3.2e5 [Pa]

END

TURBULENCE:

Option = Medium Intensity and Eddy Viscosity Ratio

END

END

END

BOUNDARY: lowerwall

Boundary Type = WALL

Location = LOWERWALL

BOUNDARY CONDITIONS:

HEAT TRANSFER:

Option = Adiabatic

END

MASS AND MOMENTUM:

Option = No Slip Wall

END

WALL ROUGHNESS:

Option = Smooth Wall

END

END

END

BOUNDARY: outlet

Boundary Type = OUTLET

Location = OUTLET

BOUNDARY CONDITIONS:

FLOW REGIME:

Option = Supersonic

END

END

END

BOUNDARY: rauwheit

Boundary Type = WALL

Location = PLATTE

BOUNDARY CONDITIONS:

HEAT TRANSFER:

Option = Adiabatic

END

MASS AND MOMENTUM:

Option = No Slip Wall

END

WALL ROUGHNESS:

Option = Smooth Wall

END

END

END

END

BOUNDARY: upperline

Boundary Type = SYMMETRY

Location = UPPERLINE

END

BOUNDARY: wandhinten

Boundary Type = SYMMETRY

Location = WANDHINTEN

END

BOUNDARY: wandvorne

Boundary Type = SYMMETRY

Location = WANDVORNE

END

DOMAIN MODELS:

BUOYANCY MODEL:

Option = Non Buoyant

END

DOMAIN MOTION:

Option = Stationary

END

MESH DEFORMATION:

Option = None

END

REFERENCE PRESSURE:

Reference Pressure = 0 [atm]

END

END

FLUID DEFINITION: Fluid 1

Material = Air Ideal Gas

Option = Material Library

MORPHOLOGY:

Option = Continuous Fluid

ENDCFX Run setting

END

FLUID MODELS:

COMBUSTION MODEL:

Option = None

END

HEAT TRANSFER MODEL:

Include Viscous Work Term = On

Option = Total Energy

END

THERMAL RADIATION MODEL:

Option = None

END

TURBULENCE MODEL:

Option = SST

END

TURBULENT HEAT TRANSFER:

TURBULENT FLUX CLOSURE:

Option = Eddy Diffusivity

Turbulent Prandtl Number = 0.9

END

END

TURBULENT WALL FUNCTIONS:

High Speed Model = On

Option = Automatic

END

END

END

END

OUTPUT CONTROL:

RESULTS:

File Compression Level = Default

Option = Standard

END

END

SOLVER CONTROL:

Turbulence Numerics = High Resolution

ADVECTION SCHEME:

Option = High Resolution

END

CONVERGENCE CONTROL:

Maximum Number of Iterations = 10000

Minimum Number of Iterations = 1

Physical Timescale = 1e-005 [s]

Timescale Control = Physical Timescale

END

CONVERGENCE CRITERIA:

Residual Target = 1e-10

Residual Type = RMS

END

DYNAMIC MODEL CONTROL:

Global Dynamic Model Control = On

END

END

END

END

COMMAND FILE:

Version = 13.0

Results Version = 13.0

END

SIMULATION CONTROL:

EXECUTION CONTROL:

EXECUTABLE SELECTION:

Double Precision = On

END

INTERPOLATOR STEP CONTROL:

Runtime Priority = Standard

MEMORY CONTROL:

Memory Allocation Factor = 1.0

END

END

PARALLEL HOST LIBRARY:

HOST DEFINITION: tud103665

Host Architecture String = winnt-amd64

Installation Root = C:\Program Files\ANSYS Inc\v%v\CFX

END

END

PARTITIONER STEP CONTROL:

Multidomain Option = Independent Partitioning

Runtime Priority = Standard

EXECUTABLE SELECTION:

Use Large Problem Partitioner = Off

END

MEMORY CONTROL:

Memory Allocation Factor = 1.0

END

PARTITIONING TYPE:

MeTiS Type = k-way

Option = MeTiS

Partition Size Rule = Automatic

Partition Weight Factors = 0.50000, 0.50000

END

END

RUN DEFINITION:

Run Mode = Full

Solver Input File = D:\hvanpelt\flat\flatrefsst.def

INITIAL VALUES SPECIFICATION:

INITIAL VALUES CONTROL:

Continue History From = Initial Values 1

Use Mesh From = Solver Input File

END

INITIAL VALUES: Initial Values 1

File Name = D:\hvanpelt\flat\flatrefsst_001.res

Option = Results File

END

END

END

SOLVER STEP CONTROL:

Runtime Priority = Standard

MEMORY CONTROL:

Memory Allocation Factor = 1.0

END

PARALLEL ENVIRONMENT:

Number of Processes = 2

Start Method = HP MPI Local Parallel

Parallel Host List = tud103665*2

END

END

END

END


ASTRIUM
AN EADS COMPANY